INVESTIGATING MICROSTRUCTURAL AND ENVIRONMENTAL EFFECTS ON THE VERY HIGH CYCLE FATIGUE BEHAVIOR OF TI-6242S

by

Jason Geathers

A dissertation submitted in partial fulfillment
of the requirements for the degree of
Doctor of Philosophy
(Mechanical Engineering)
in the University of Michigan
2016

Doctoral Committee:

Associate Professor Samantha H. Daly, Co-Chair
Professor J. Wayne Jones, Co-Chair
Professor John E. Allison
Associate Professor Vikram Gavini
Adam L. Pilchak, Air Force Research Laboratory

To my family

ACKNOWLEDGEMENTS

First and foremost, I would like to thank my academic advisors and committee co-chairs, Professor Samantha Daly and Professor J. Wayne Jones, for their support and guidance, without which this thesis would not have been possible. I truly appreciate the tremendous amount of time, advice, and patience that they devoted to my professional and personal development during my time at the University of Michigan. I would also like to thank the rest of my committee members, Professor John Allison, Professor Vikram Gavini, and Dr. Adam Pilchak, for their invaluable insights and careful consideration and critique of my dissertation.

The fatigue experiments presented in this dissertation would have been difficult to conduct without Chris Torbet of the University of California Santa Barbara, who assisted in the designing and building of the *in situ* ultrasonic fatigue and scanning electron microscopy system. I would also like to thank him for his help in the designing of experiments and continuous technical support. I am also grateful to Dr. John Mansfield, Dr. Emmanuelle Marquis, and Bobby Kerns of the University of Michigan Center for Materials Characterization for their assistance with facilities use and troubleshooting the experimental setup.

I must also thank my numerous colleagues, who provided thoughtful discussions regarding research and other topics, as well as encouragement, assistance, and camaraderie: Dr. Ben Reedlunn, Dr. Kyubum Kim, Dr. Adam Kammers, Dr. Alfred Okello, Dr. Michael Kimiecik, Dr. Jared Tracy, Dr. Jiashi Miao, Dr. Zhe Chen, Dr. Qianying Shi, Dr. Xianfeng Ma, Dr. Luke Rettberg, Dr. Tracy Berman, Sinsar Hsie, Alan Githens, Joyce Gong, Will LePage, Michelle

Harr, Marissa Linne, Aeriel Murphy, Erin Deda, Anna Trump, Vir Nirankari, Jacob Adams, Paul Schrems, Allison Ryan, Emmanuel Nyangweso, and Steve Orloff.

I would also like thank my family, my girlfriend, and friends for their love, support, encouragement, and prayers. All of this would have been impossible without you.

Finally, I gratefully acknowledge the Air Force Office of Scientific Research, Structural Mechanics Program, monitored by Dr. David Stargel (Project No. F031559), for funding the majority of this work. I would also like to acknowledge the Rackham Merit Fellowship Program at the University of Michigan for providing the initial startup funding. A special thank you is extended to my Air Force Research Laboratory collaborators, especially Dr. James M. Larsen, Dr. Sushant Jha, and Dr. Christopher Szczepanski (currently at Special Metals Corp.) for providing the titanium alloy that was used in this dissertation and for their insightful discussions and support.

TABLE OF CONTENTS

LIST OF TABLES

LIST OF FIGURES

LIST OF APPENDICES

ABSTRACT

INVESTIGATING MICROSTRUCTURAL AND ENVIRONMENTAL EFFECTS ON THE VERY HIGH CYCLE FATIGUE BEHAVIOR OF TI-6242S

by

Jason Geathers

Chairs: Samantha Daly, J. Wayne Jones

Extending the service lifetimes of existing components, and designing new mechanical systems capable of withstanding longer lifetimes, is critically important for applications in the aerospace, energy generation, and transportation sectors. These applications require an understanding of the coupled interactions between local microstructure and environmental effects. Towards this end, the effects of microstructure and environment on fatigue damage accumulation behavior in the VHCF regime were investigated in the near alpha titanium alloy Ti-6Al-2Sn-4Zr-2Mo-0.1Si (Ti-6242S). The influence of microstructure and environment on fatigue crack initiation from micro-notches, and on early crack growth behavior, was characterized using ultrasonic fatigue. Fatigue crack growth was studied in laboratory air, high vacuum (1.7×10^{-4} Pa), and in various pressures of water vapor, high purity oxygen, and hydrogen gas.

A new experimental methodology was developed that combines ultrasonic fatigue at 20 kHz and environmental scanning electron microscopy to examine small crack growth behavior as a function of the local microstructure, *in situ*. Ultrasonic fatigue techniques enabled the acquisition

of large numbers of cycles in significantly shorter timeframes than conventional testing techniques. Incorporating fatigue testing directly into an environmental scanning electron microscope (ESEM) enabled very high spatial resolution imaging (≈ 5 nm) of localized damage accumulation at the micro-scale and early crack initiation and growth observations.

A number of findings have resulted from these experiments and analyses, which have provided new insights in fatigue mechanisms in the VHCF regime. Natural fatigue crack initiation occurred at or very near grain boundaries between two similarly oriented primary alpha grains that were not favorably oriented for slip. Small fatigue cracks took longer to initiate from micronotches in vacuum than in laboratory air or low pressure water vapor environments (65 Pa – 665 Pa). Water vapor was also found to be significantly more deleterious to fatigue life than either pure hydrogen or pure oxygen at equivalent pressures. Similar fatigue crack growth rates were obtained for cracks grown in ambient air and 1330 Pa water vapor environments (corresponding to a relative humidity of 40%-60%), suggesting a dominance of water vapor effects in ambient air as well. Fatigue crack growth rates were found to significantly increase with increasing water vapor pressure in both the primary α phase and the lamellar $\alpha + \beta$ microstructure. Increased fatigue crack growth rates in water vapor and oxygen were determined to be due to adsorption-assisted crack propagation, which stems from atoms or molecules being adsorbed onto fresh surfaces at the crack-tip causing increased irreversibility. A striking change in the fatigue crack growth rate of an arrested crack with a change in environment indicated an associated loss of effectiveness of grain boundaries as barriers to short crack propagation.

CHAPTER 1

INTRODUCTION

The annual cost of high cycle fatigue to the military has been estimated to be over $400 million [1]. Additionally, there has been increased interest in the design of components to handle increasingly longer lifetimes (>10^7 cycles), and it is critically important to be able to accurately predict when these components will fail. Increasing the service lifetimes of components into the very high cycle fatigue (VHCF) regime, in which components are loaded to >10^7 cycles, requires an understanding of the interactions between the intrinsic material properties and the operating environment.

There is a growing need to extend the service life of systems and components well beyond the traditional fatigue design limits of 10^7 cycles, into the VHCF regime. Researchers have conventionally assumed the existence of a fatigue limit, or threshold stress amplitude below which fatigue life is infinite [2]. This assumption is historically linked to fatigue studies of ferrous metals in the high cycle fatigue (HCF) regime, a fatigue life range of 10^4 to 10^7 cycles [3]. However, recent studies conducted at 30-100 Hz [4, 5] and at ultrasonic frequencies [6, 7] reveal that this assumption may not be a valid design approach for materials operating in the VHCF regime. Even at applied stresses well below the conventional fatigue threshold and at nominally elastic strains characteristic of VHCF, damage accumulation at the microstructural length scale can lead to crack initiation and fatigue failure [8-11]. Furthermore, fatigue life in

this regime is dominated by crack initiation and the growth of microstructurally small cracks. Thus, a significant portion of the fatigue life involves micro-scale mechanistic responses to cyclic stresses [12]. The sensitivity of cyclic deformation mechanisms to microstructural influences adds complexity and uncertainty to lifetime predictions.

Fatigue in the VHCF regime poses additional challenges in component design when considering the significant influence of microstructural variability and environmental effects. One practice is to extrapolate test data from the high cycle fatigue regime to higher numbers of cycles. This can lead to non-conservative fatigue life estimates in some materials, such as titanium alloys with a duplex microstructure, due to the occurrence of fatigue life failures well below the mean life behavior. Another method is to interrogate the VHCF regime directly. This is typically done using ultrasonic fatigue techniques that operate most commonly at 20 kHz that enable investigating VHCF behavior in a time-efficient manner. The use of ultrasonic fatigue testing systems is typically carried out in laboratory air, with little discussion of environmental effects. A substantial knowledge gap remains in high frequency, long life testing and the environmental processes that may be operative in this regime. In evaluating the environmental mechanisms responsible for diminished fatigue lifetimes and increased fatigue crack growth rates at ultrasonic fatigue frequencies, the following questions remain:

1. Are the mechanisms for enhanced fatigue crack growth with increased environmental activity that are proposed for short lifetime, low frequency testing relevant in the VHCF regime at ultrasonic frequencies?
2. What factors or dependencies govern the mechanisms for environmentally assisted fatigue crack growth during ultrasonic fatigue, and how do they compare to lower frequency testing?

3. What insights can be gathered from environmental testing using ultrasonic fatigue to help develop a better understanding of the surface vs. sub-surface fatigue crack initiation competition observed in many materials at longer lifetimes at ultrasonic frequencies?

The present work focused on addressing these questions regarding environmental effects on the fatigue behavior of near-alpha titanium alloys using a direct, experimental approach. This new experimental methodology combines ultrasonic fatigue testing capabilities at 20 kHz with an environmental scanning electron microscope (ESEM).

Ultrasonic fatigue testing has been used since the early 1950s [13, 14] to provide a powerful and time-effective means for interrogating VHCF of a wide range of materials including cast aluminum alloys [15, 16], nickel-base superalloys [8, 17], titanium alloys [11], and high strength steels [18, 19]. Over the past forty years the technique has been extended to enable VHCF studies under various environmental conditions [8, 20], in crack growth studies [21-23], and in conjunction with other techniques such as synchrotron x-ray imaging [17]. However, the data acquired from ultrasonic fatigue testing largely remains limited to determination of total fatigue life, crack growth rates, and deformation processes that are inferred from fractography and surface microscopy. Observations regarding crack initiation and ultimate failure are linked to microstructure in a before-and-after methodology through grain mapping techniques, mainly by electron backscatter diffraction, with limited *in situ* observations. Efforts have been made to track the evolution of deformation and formation of early fatigue damage, such as slip bands, by using methods that probe the damage micro-mechanisms taking place as a function of the number of cycles. For example, replication is a common technique used to obtain surface fatigue damage history as a function of applied cycles [22]. In another approach, Stanzl-Tschegg et al. [24] used a combination of high resolution SEM and atomic force microscopy (AFM) to

investigate fatigue damage in copper polycrystals in the VHCF regime. This technique was *ex situ* and required a significant amount of time, but provided useful information regarding the progression of fatigue damage at even 50% below the persistent slip band (PSB) threshold. In order to advance the understanding of fatigue crack initiation and early crack growth in VHCF, new experimental techniques are needed that enable the *in situ* study of damage accumulation mechanisms as a function of microstructure and environment.

The overall aim of this dissertation research was to develop a fundamental understanding of environmental and microstructural influences on fatigue damage mechanisms in titanium alloys in the VHCF regime, thereby advancing accurate life prediction models and increasing the efficiency and reliability of aerospace components.

The specific objectives of this thesis work were to:

1. Develop and validate a new experimental methodology that combines ultrasonic fatigue testing techniques at 20 kHz with (environmental) scanning electron microscopy;
2. Determine the effects of laboratory air, water vapor, oxygen, hydrogen, and vacuum environments on small fatigue crack growth rates in Ti-6242S;
3. Characterize the processes responsible for environmental effects on small fatigue crack growth in Ti-6242S in ultrasonic fatigue;
4. Identify the microstructural features responsible for fatigue damage accumulation and add to our understanding of the mechanisms of fatigue crack initiation in the VHCF of Ti-6242S, which represents an important class of near-α titanium alloys used in aerospace applications.

Chapter 2 provides a review of the literature that is relevant to the present work, including previous studies of microstructural and environmental effects on fatigue behavior of titanium alloys. A review of investigations of environmental influences of fatigue of various materials at an ultrasonic frequency of 20 kHz will also be discussed. In Chapter 3, the experimental methods for VHCF studies in air and other environments is described, along with details of instrumentation developed for *in situ* SEM studies. A detailed description of the influence of microstructure and environment on small fatigue crack growth behavior in Ti-6242S at 20 kHz with respect to the processes responsible for this behavior is presented in Chapter 4. The results of very high cycle fatigue crack initiation experiments of Ti-6242S in both laboratory air and vacuum is presented in Chapter 5. Finally, conclusions and recommendations for future work are detailed in Chapter 6.

CHAPTER 2

LITERATURE REVIEW

In this chapter, a review of the literature relevant to understanding the objectives, the approach, and the results of this dissertation is presented. Section 2.1 describes the physical and mechanical metallurgy of alpha and near-alpha titanium alloys, and includes discussion of the relevant processing routes and deformation processes of titanium alloys. A review of work aimed at understanding fatigue behavior in titanium alloys in relation to microstructural effects is described in Section 2.2. Section 2.3 summarizes the findings of studies regarding frequency and environmental effects in fatigue of titanium alloys. Section 2.4 focuses on the oxidation behavior of titanium and titanium alloys in the presence of various gaseous environments, which is critical as it relates to processes that govern environmental effects in fatigue of titanium alloys. Finally, Section 2.5 provides a summary of this literature review, including an identification of open questions, and states the objectives and the approach taken to meet them.

2.1 Microstructure of Titanium Alloys

The physical and mechanical properties of pure titanium and titanium alloys have been studied extensively and many published review papers and books are available which summarize these investigations. This literature review was completed using information from the books *Titanium 2nd Edition* by Lutjering and Williams [25] and *Titanium and Titanium Alloys* by Leyens and Peters [26]. A recent review paper on scientific studies regarding titanium by Banerjee and Williams [27] provided a detailed examination of the current state of titanium research and was a useful resource in the completion of this chapter as well.

2.1.1 Physical Metallurgy

As shown in the Ti-Al binary phase diagram in Figure 2.1, pure titanium undergoes an allotropic phase transformation at 882 °C from a hexagonal close-packed phase (α) to a body centered cubic phase (β). The equilibrium phase at room temperature is the α phase and at temperatures above 882 °C the β phase is stable. The temperature of the transformation is called the beta transus (T_β) and is determined by the alloy composition. By varying the alloy composition and the processing route, it is possible to control the morphology of the microstructure and the volume fractions of the α and β phases. In addition to composition, the mechanical properties of titanium alloys are largely determined by thermomechanical processing and heat treatment. The wide range of microstructures that can be obtained through alloying and thermomechanical processing are generally classified as α, $\alpha + \beta$, or β titanium alloys. Figure 2.2 shows examples of different types of titanium alloy microstructures.

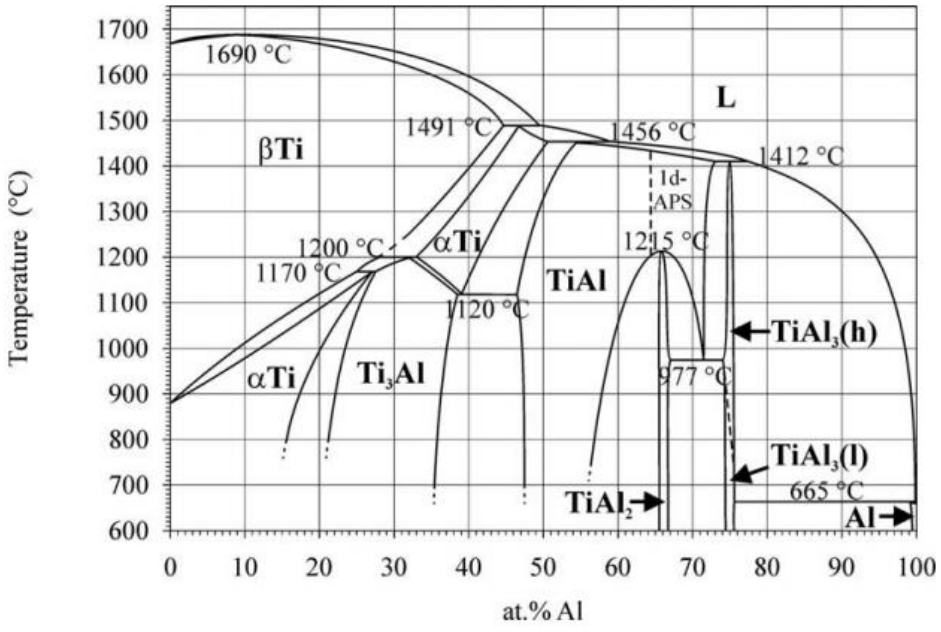

Figure 2.1: Ti-Al binary phase diagram illustrating the α stabilizing effect of aluminum alloying [28]

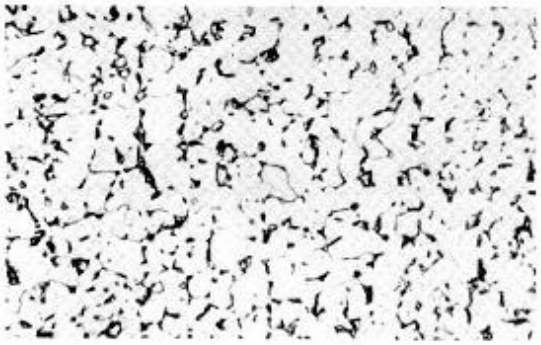

(a) Equiaxed α and a small amount of intergranular β.

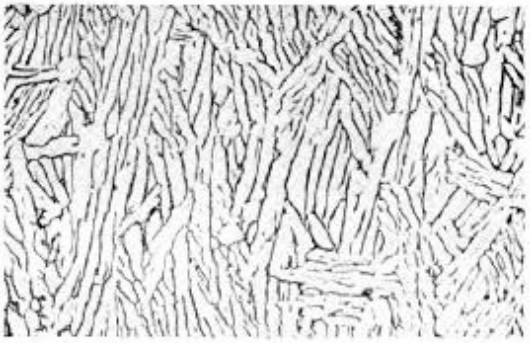

(d) Small amount of equiaxed α in an acicular α (transformed β) matrix.

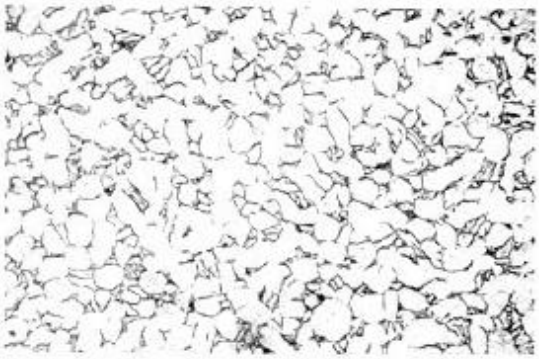

(b) Equiaxed and acicular α and a small amount of intergranular β.

(e) Plate-like acicular α (transformed β); α at prior β grain boundaries.

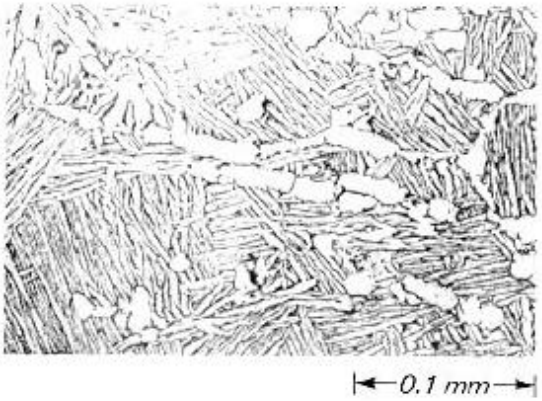

(c) Equiaxed α in an acicular α (transformed β) matrix.

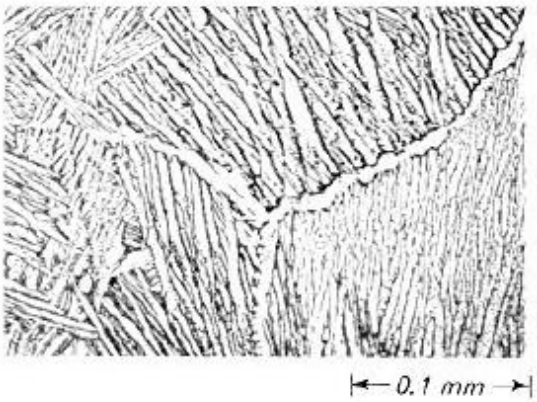

(f) Blocky and plate-like acicular α (transformed β); α at prior β grain boundaries.

Figure 2.2: Micrographs showing the morphologies and length scales of microstructures attainable by control of material composition and thermomechanical processing route [29]

The material used in the present study is the near-alpha titanium alloy Ti-6242S with a nominal composition of wt.%. 6Al, 2Sn, 4Zr, 2Mo, 0.1Si, and Ti (balance). Aluminum is a well-known α-stabilizer that raises the T_β temperature as its concentration is increased. High aluminum content also increases slip planarity. Precipitation of the brittle Ti_3Al phase occurs at concentrations just above 6% aluminum equivalent. Thus, in applications where damage tolerance is a design criterion, titanium alloys having less than 6% aluminum are used. Tin and zirconium are thermodynamically neutral, but preferentially segregate to the α phase and increase the strength of the α phase by solid solution strengthening. Molybdenum is a β-stabilizer that preferentially segregates to the β phase and increases the strength of the β phase by solid solution strengthening. Silicon is also a β stabilizer that forms intermetallic compounds through a eutectoid reaction. Silicon also increases the creep resistance of titanium alloys used in high temperature applications. Interstitial additions of oxygen, nitrogen, and carbon are also possible and strengthen the α phase. However, they are susceptible to forming hard alpha and their concentrations are carefully controlled. Titanium has extensive solubility for oxygen and nitrogen. Because of this titanium alloys do not contain oxide or nitride inclusions that commonly initiate fatigue failure in other structural materials. Hydrogen stabilizes the β phase and forms eutectoids. A review of the effects of different elements on α and β phase stability is shown in Figure 2.3.

The microstructural morphologies that form mainly due to thermomechanical processing are commonly classified as equiaxed α, lamellar α, equiaxed α + transformed β, and Widmanstätten. There are numerous thermomechanical steps needed to form each of these microstructures, but the remainder of this section will focus only on the material properties and mechanical behavior of the equiaxed α + transformed β microstructure, which is the type of microstructure used in the

material in this dissertation work. This class of microstructure is also the most widely used in titanium alloys that possess a good balance of strength and toughness.

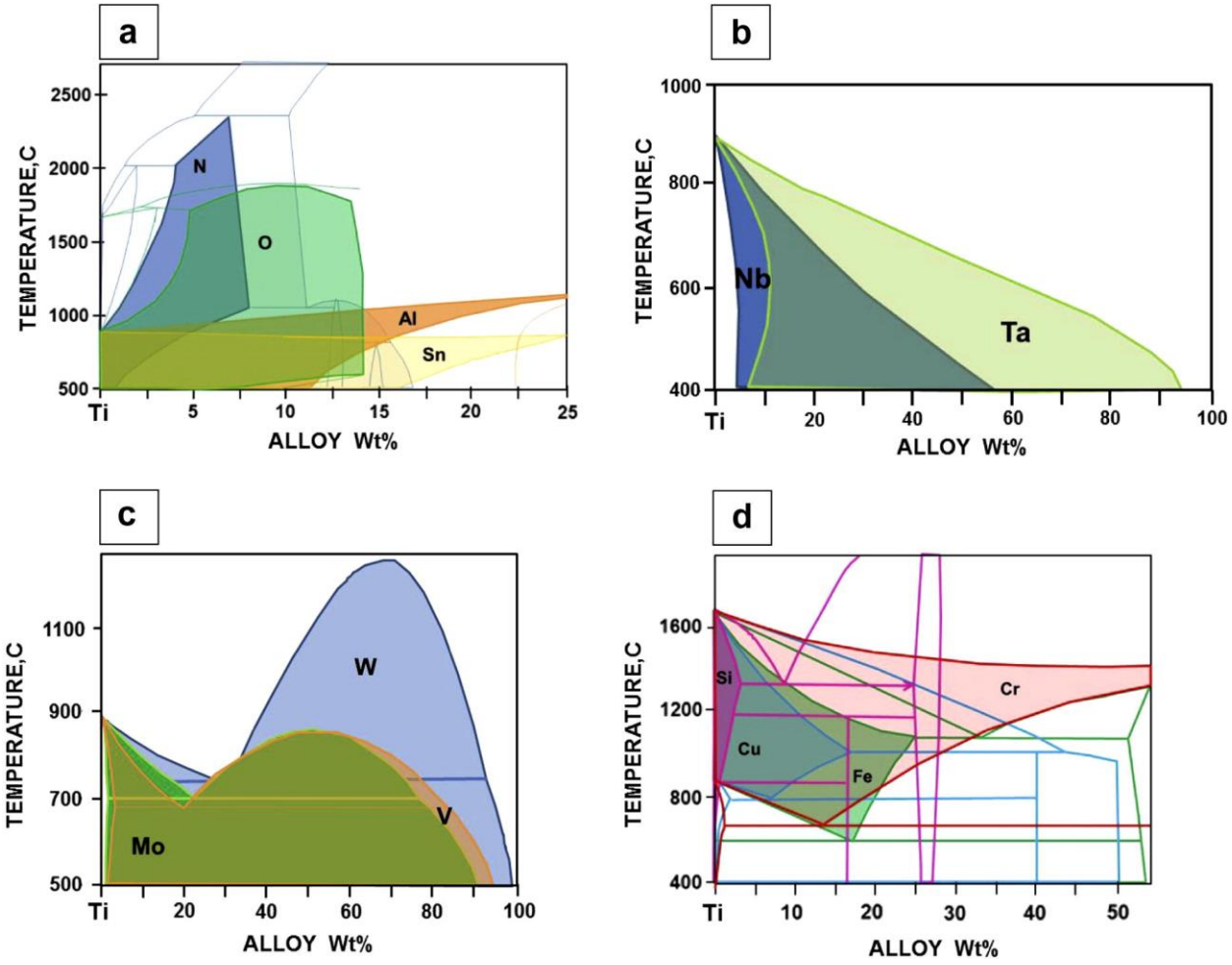

Figure 2.3: Diagrams showing the effects of various elements on the beta transus in Ti alloys. (a) α stabilizers, (b) β stabilizers with continuous solubility, (c) β stabilizers with an immiscibility gap in the β phase, and (d) eutectoid systems with intermetallic compound formations [27]

2.1.2 Description of Microstructure

Figure 2.4 shows a high magnification backscattered electron micrograph of the Ti-6242S material used in this work and serves as an example of the bi-modal, or duplex microstructure commonly observed in titanium alloys composed of an equiaxed primary alpha (α_p) phase and a transformed β matrix phase. As shown in Figure 2.4, the microstructure consists of several different features ranging in size and shape. Each of these features form in response to the thermomechanical processing steps. The lath α forms in the β phase through an allotropic phase transformation. The orientation of this phase is determined by the Burgers orientation relationship (BOR) between the two phases: $\{110\}\beta//(0001)\alpha$; $<1\bar{1}1>\beta//<11\bar{2}0>\alpha$. This requires that the close packed planes of the hcp α phase are aligned with the close packed planes of the bcc β phase. Because of this, slip is often continuous across the lath α regions. The globular, equiaxed α_p grains evolve from the α laths by a spherodization process. The α_p phase does not necessarily maintain the Burgers orientation relationship, and as a result slip transfer is not necessarily continuous between α_p grains and the β matrix. The main source of strength, strain incompatibility, and stress inhomogeneity in titanium alloys comes from the barrier to dislocation motion represented by α/β interfaces. Because of this, controlling the size, morphology, and volume fraction of the alpha phase in structural titanium alloys is critical to enhancement of mechanical properties [26]. Much of this control is achieved by the thermomechanical processing route, which is discussed in the next section.

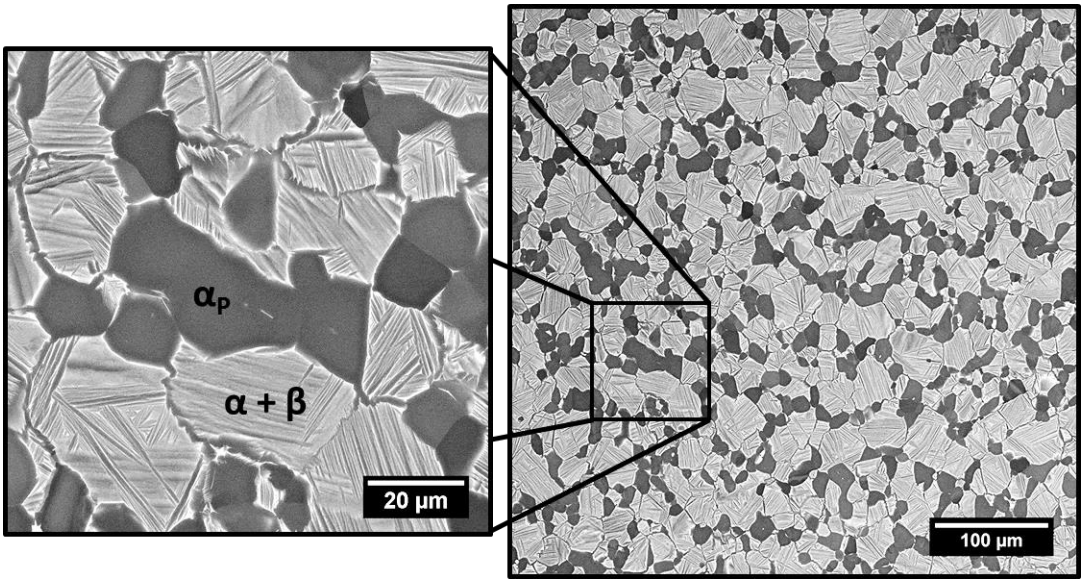

Figure 2.4: Backscattered electron micrograph of Ti-6242S material as an example of the bimodal, or duplex microstructure which consists of globular primary α grains in a transformed β matrix

2.1.3 Thermomechanical Processing

The exact processing route used to form the material studied in this dissertation is proprietary. However, the general processing route for the production of titanium alloys having a duplex, or bi-modal microstructure is discussed in this section. The titanium alloy used in this dissertation work was processed to minimize microtexture, but it should be mentioned that the relationship between microstructure evolution and microtexture has gained significant interest in recent years. The presence of large microtextured regions, or macrozones of similarly oriented grains, can cause early fatigue failures and more work is needed in understanding the origin of these regions and their influences on cyclic and dwell fatigue behavior. The schematic of various processing paths and the texture developed at key steps is shown in Figure 2.5.

The initial process used in the production of the titanium alloy used in this dissertation is a vacuum arc remelting (VAR) process applied to an ingot several times to homogenize the material and remove impurities. Rotor grade VAR ingots are typically triple melted and often

given a homogenization anneal in the β phase field prior to hot working. The times and temperatures vary with alloy, but are typically 200-450 °C above the β- transus (T_β) for 20-30 hours. Regardless of whether or not a homogenization process is done, the ingot is conditioned by grinding or lathe turning before forging. Once conditioned, the material would have been forged in the β phase field at approximately 150° C above T_β and then cooled, with the cooling rate determining the width of the α lamellae. A schematic of the processing route for bi-modal microstructures beginning with this step is shown in Figure 2.6. Reheating to a temperature below T_β and further hot working refines the microstructure. The deformation from this step can lead to crystallographic textures that can strongly influence mechanical properties. A low, or weak texture, such as observed in the material of this study, is obtained by performing this deformation step at a moderate temperature in the $\alpha + \beta$ phase field. A recrystallization step in the $\alpha + \beta$ phase field follows this step and has little effect on the crystallographic texture formed in the previous step. Finally, annealing at a moderate temperature in the $\alpha + \beta$ phase field completes the process.

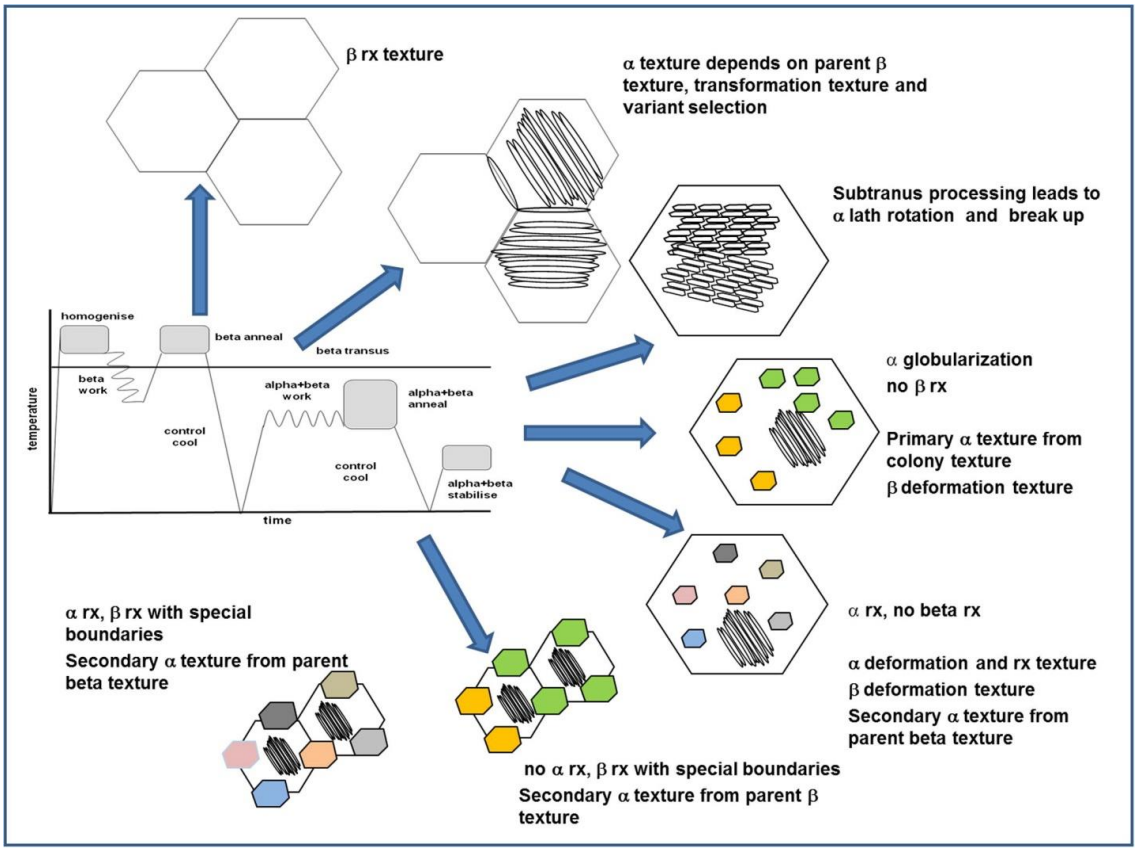

Figure 2.5: Schematic of various processing paths in titanium alloys and the texture developed at key steps [30]

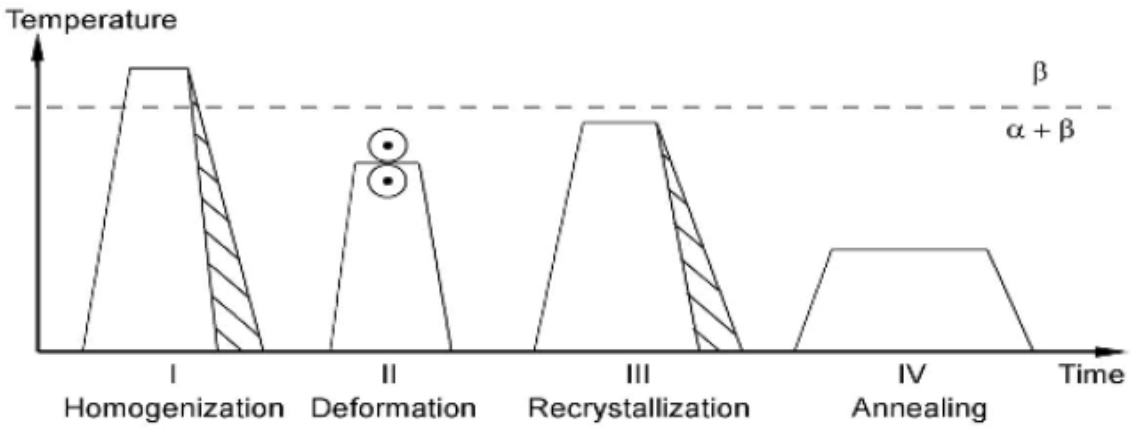

Figure 2.6: Schematic of the processing route for bi-modal microstructures of Ti alloys [25]

2.1.4 Mechanical Behavior of Titanium

There have been numerous studies on the monotonic deformation behavior of pure titanium and titanium alloys to determine the effects of composition, temperature, and microstructure on the inherent strength of the material and the critical resolved shear stress (CRSS) for the various slip planes. Ogi et al. have investigated the elastic moduli of alpha titanium with temperature and the findings are reported in Figure 2.7 [31]. The Young's modulus of the "c" direction was higher than the "a" direction and all of the elastic constants decreased with increasing temperature.

In α and near-α titanium alloys plastic deformation is extremely anisotropic [32-34]. Plastic deformation behavior is controlled by slip on the basal (0002), prismatic $(10\bar{1}0)$, and pyramidal $(10\bar{1}1)$ crystal planes as shown in Figure 2.8. Slip generally occurs on these planes in the <a> type directions $<11\bar{2}0>$. These represent four independent slip systems. Satisfaction of the Von Mises criterion for plastic deformation requires five independent slip systems and is obtained by activation of slip that may occur along the c-axis in the $<11\bar{2}3>$ direction by <c + a> slip or by deformation twinning. Numerous studies have reported that CRSS for both basal and pyramidal slip are higher than the CRSS for prismatic slip in pure titanium and Ti-Al alloys [25, 35]. Figure 2.9 shows a plot of CRSS of the slip systems versus temperature in single crystals of Ti-6.6Al. It should be noted that slip in α grains still tends to occur by basal or prismatic slip even when well oriented for pyramidal slip.

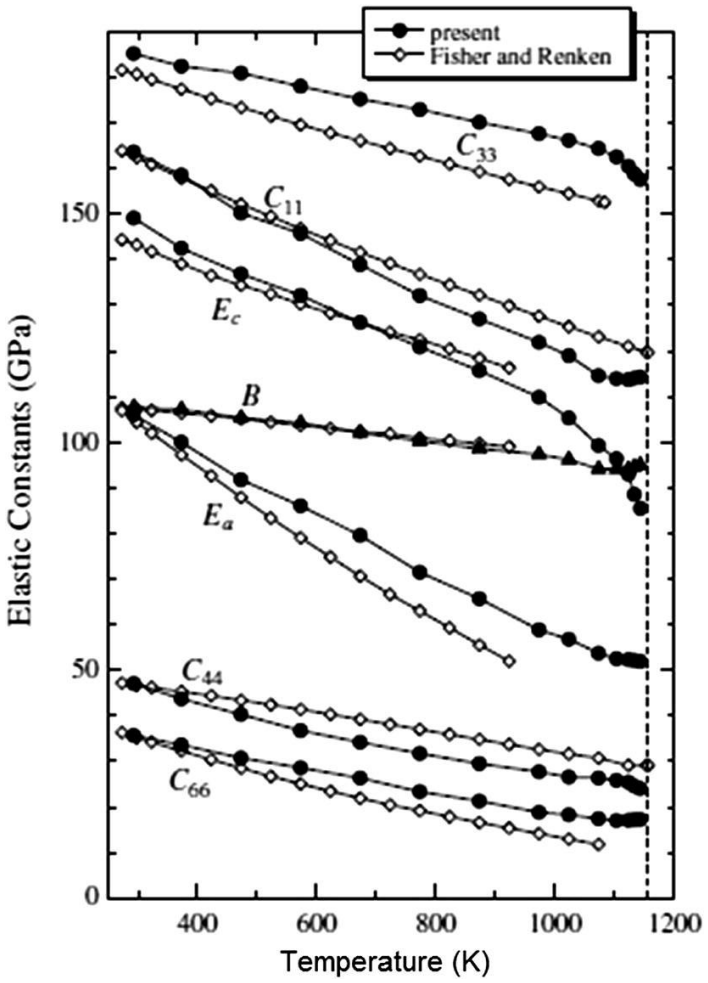

Figure 2.7: Elastic constants of the α phase in titanium as a function of temperature are shown. The Young's modulus in the "c" direction was higher than the "a" direction. [31]

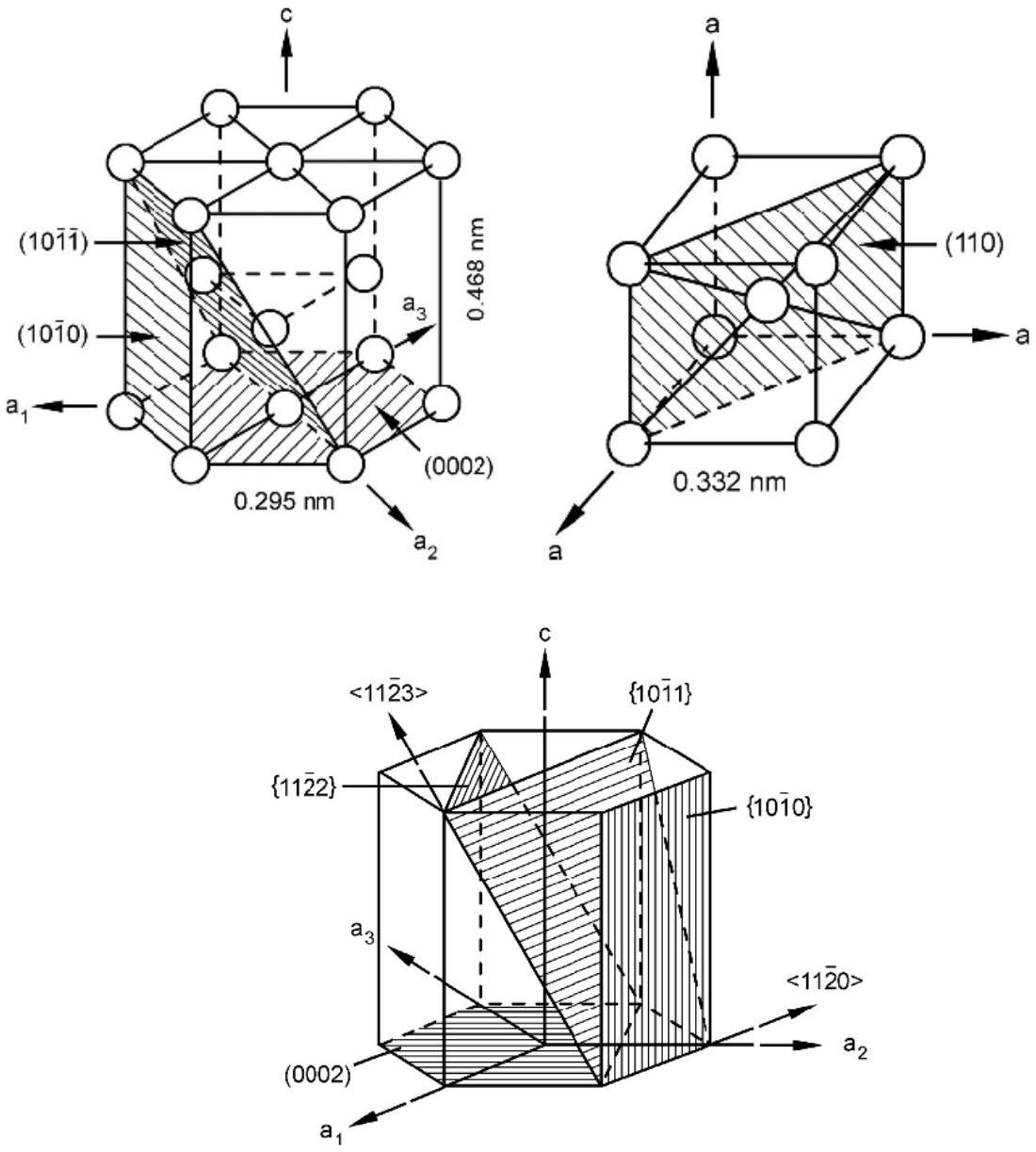

Figure 2.8: Slip systems of α phase titanium, hcp and β phase titanium, bcc are shown. Plastic deformation behavior is controlled by slip on the basal, (0002), prismatic (10$\bar{1}$0), and pyramidal (10$\bar{1}$1) crystal planes of the α phase. [25]

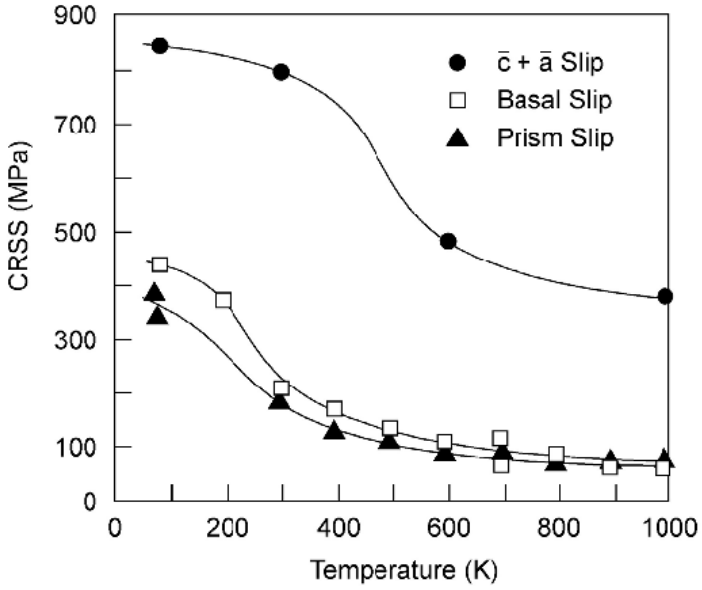

Figure 2.9: CRSS for basal, prism, and <c + a> slip in single crystals of Ti-6.6Al as a function of temperature [36]

2.1.4.1 Slip in Ti-Al systems

The CRSS for prismatic slip in Ti-Al alloys has been observed to increase with increasing aluminum composition [37], while the CRSS for basal slip remained constant. The CRSS for basal and prismatic slip was also reported to be equal at 6.6wt% aluminum. This is attributed to the fact that α-stabilizing substitutional elements, such as aluminum and oxygen, increase the atomic packing fraction on basal planes relative to prism planes. Williams et al. [25] also investigated the effect of aluminum on deformation in Ti-Al single crystals with compositions ranging from 1.4 to 6.6% Al in the temperature range 300-1000 K. Similarly, they concluded that the CRSS for basal and prism slip become the same at higher Al concentrations and temperatures. The CRSS for <c + a> slip on the (1122) plane was also reported to be much higher than that for basal or prism slip. Work by Tanaka and Conrad [38] on titanium single crystals also showed that the ratio of CRSS on the basal and pyramidal planes to the prismatic plane decreases with increasing interstitial and aluminum content.

Twinning is suppressed and planar slip occurs in titanium alloys that have moderate to high aluminum and oxygen compositions [39, 40]. The decrease in the frequency of the occurrence of twinning is compensated for by the activation of non-basal <c + a> slip. Since <c + a> slip has a significantly higher CRSS than both basal and prism slip (Figure 2.9), crystals loaded parallel or near parallel to their c-axis will have increased strength. The cause of slip planarity in response to Al content is believed to be slip plane softening as a result of a destruction of *short range order* (SRO). Ordering of oxygen at interstitial sites may also affect slip on basal and prismatic planes [41]. Similar to precipitation hardened systems, regions with SRO provide increased tensile strength at the expense of ductility. Regions with SRO are also theorized to promote slip localization during cyclic loading. A study performed on Ti-7Al indicated that homogenous slip generally led to longer lives under dwell fatigue conditions. In general, fracture surfaces in SRO materials support the existence of greater slip planarity due to particle shearing. Planar slip intensifies in the presence of both Al and O, but the exact processes for how these elements affect slip behavior is not well understood. Planar slip on basal planes has been associated with faceted fatigue crack initiation in many titanium alloys and is discussed in Section 2.2.

2.1.4.2 Summary of Deformation Mechanisms

Titanium alloys plastically deform by slip on basal, prismatic, and pyramidal planes in <a> type directions. In grains that are poorly oriented for <a> slip, plastic deformation can occur by twinning or <c + a> slip. However, twinning is suppressed in titanium alloys that have high concentrations of the interstitial and substitutional elements oxygen and aluminum, respectively. The CRSS for <c + a> slip is also higher than both basal and prism slip, with prism slip often having the lowest CRSS.

Slip transfer in the bi-modal microstructure consisting of equiaxed α in a transformed β matrix is a complex process that is not well understood. It has been shown that slip initiates in the equiaxed α phase consistent with Schmid's law at the surface. In fact, the transformed β regions are believed to contribute only slightly to the yield strength of the material for this reason. Because the deformation is controlled by the α_p phase, the focus of most investigations, as well as this dissertation, has been on understanding the mechanisms that govern strain localization, crack initiation, and crack growth as it relates to this phase.

2.2 Fatigue of Titanium Alloys – Microstructural Effects

Several investigations have been conducted in order to develop a better understanding of the fatigue behavior of titanium and titanium alloys [26]. This work has spanned the low cycle to the very high cycle fatigue regimes. However, this section will focus on a review of findings regarding high cycle and very high cycle fatigue behavior of titanium alloys. A discussion of observed mechanisms and processes for strain accumulation, fatigue crack initiation, and early crack propagation as a function of microstructure is detailed. The effects of frequency and environment will be described in the next section.

2.2.1 Fatigue Crack Initiation

Determination of when a fatigue crack has initiated remains a debated topic and is often characterized by the detection limits of the experimental technique. For example, in the case of scanning electron microscopy this equates to the resolution of the SEM system being used. Another methodology is to define the number of cycles for crack initiation based on when the crack begins to behave as a propagating crack. By this definition, crack initiation will be determined by the scale of the microstructure, which can range from individual α laths to large α colonies. Hall defines these fatigue critical microstructures as *crack-like discontinuities* (CLD),

or the minimum feature size at which the accumulated fatigue damage starts to behave as a fatigue crack [42]. Examples of these features in titanium alloys includes α_p grains, α colonies, prior β grains, and macrozones as illustrated in Figure 2.10. In general, the type of microstructure responsible for fatigue crack initiation is determined by both the microstructure and the nature of the fatigue loading.

In materials absent of inclusions and porosity, fatigue cracks will initiate in locations where the local microstructure promotes the accumulation of irreversible slip. A review of the literature on fatigue crack initiation in α and near-α titanium alloys establishes that fatigue damage typically accumulates in the α_p phase [43-47]. This is reasonable given that the α phase accounts for the largest phase by volume and has a higher propensity for strain localization than the β phase, which is usually harder due to precipitation strengthening.

The mechanisms responsible for fatigue crack initiation in titanium alloys have been classified as slip band formation in α grains, α/β strain incompatibility, strain incompatibility between adjacent α grains, and damage accumulation across microtextured regions. In the case of the duplex microstructure, the fatigue cracks predominantly nucleated on or near the basal plane of α_p grains [44, 48]. However, fatigue crack initiation has been observed to occur on prism planes as well [48]. Additionally, investigators have shown that both basal and prism slip can be activated in the crack initiation region.

The fatigue crack initiation mechanism also varies with stress. At higher stresses, slip bands leading to cracks are formed within the α_p grains or across α colonies, while at lower stresses the α/β interface is often reported as the initiation site. This is reasonable given that at low stresses it is expected that the required amount of damage needed to initiate a crack may not be attainable within a single microstructural element. Because of this, it is expected that barriers to slip

activity such as grain or colony boundaries may play a critical role in the crack nucleation process by causing strain localization, or dislocation pile-ups at these boundaries. Regardless, the damage accumulation within the α phase leads to the eventual fatigue crack initiation.

The presence of facets at the fatigue crack initiation site has been reported by many researchers [43, 49-52]. The plane normals of these fatigue facets are nearly parallel to the loading direction. For example, Slavik et al. examined the orientation of fatigue fracture facets in Ti-6246 using a combination of tilt fractography and EBSD [53]. They showed that facets near the fatigue crack initiation site tended to have facet normals nearly parallel to the loading axis under both cycle and dwell fatigue conditions. The facets occurred on near-basal planes with their c-axis within 15° of the loading direction, especially in the case of fully reversed loading conditions. However, specimens failed under monotonic tension mostly had facets with facet normals oriented 40°- 50° from the loading axis. This behavior was explained using a modified Stroh model first proposed by Neal and Blenkinsop [54] to account for fatigue cracks that were observed to initiate from facets that formed in α grains or colonies with their basal plane normals oriented to the loading axis. Stroh originally proposed this model as a fracture mechanism in the case of monotonic loading of metals [55]. In the modified model for fatigue, hard-soft grain pairs are theorized to be preferential sites of fatigue crack nucleation. Grains that are favorably oriented for prismatic slip, termed “soft”, develop shear stresses in an adjacent grain that has no easy slip systems, or a “hard” grain. Primary α grains with basal plane normals oriented parallel to the loading axis are prime candidates to serve as hard grains for load shedding from the soft neighbor grain by dislocation pileup. Eventually, the stresses become high enough in the hard grain to cause slip or cracking by operation of a pseudo cleavage mechanism. This modified form of the Stroh mechanism to account for cyclic loading is shown in Figure 2.11. Work by

Bantounas et al. on fatigue crack initiation behavior in Ti-6Al-4V supported this model [52]. Faceted fatigue crack initiation failure was associated with grains having their c-axis orientations near (15° - 40°) the loading axis direction. Recently, work by Brandes et al. [56] which investigated fatigue behavior in Ti-7Al reported that facet formation on basal planes did not require the presence of a hard-soft grain pair. Soft-soft grain pairs were also shown to result in faceted fracture. A summary of the pairings for which facet formation was observed is shown in Figure 2.12. These “defects” represent examples of how fatigue cracks initiate from a neighborhood effect rather than from an individual grain. However, it is important to recognize that much of our understanding of fatigue crack initiation mechanisms is linked to surface observations. Tools and methodologies that enable subsurface examination of the critical microstructural features for fatigue crack initiation are becoming more widely utilized.

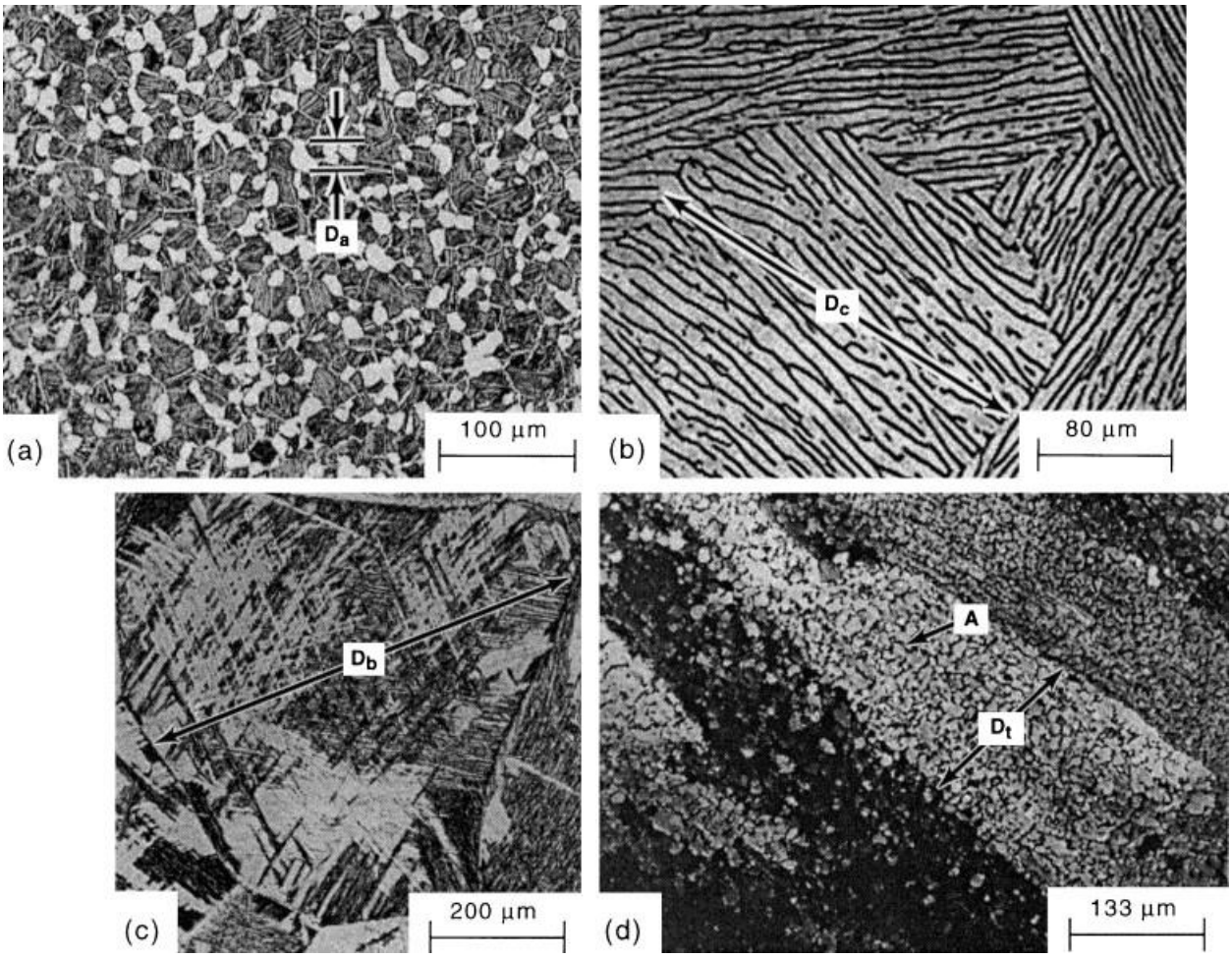

Figure 2.10: Examples of microstructural features that can cause fatigue crack initiation in $\alpha + \beta$ titanium alloys are shown. (a) α_p grains, (b) α colonies, (c) prior β grains, (d) microtextured regions. [42]

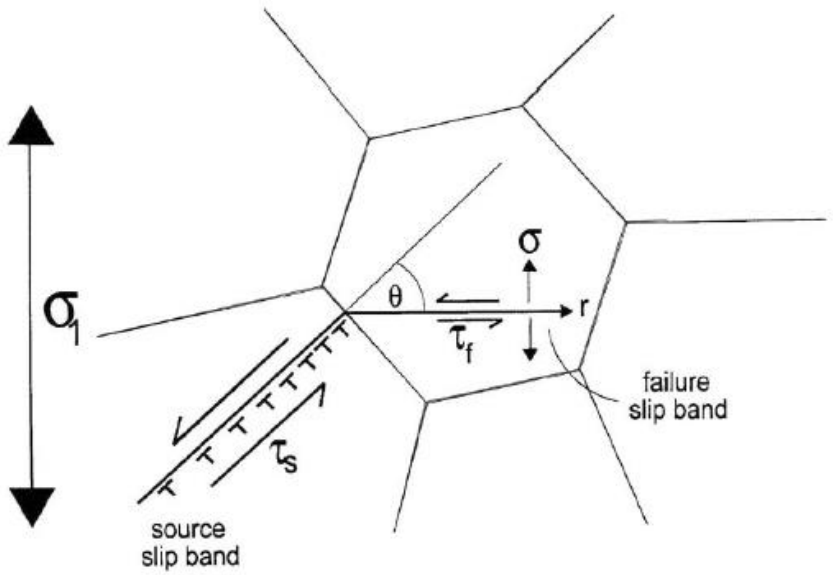

Figure 2.11: Schematic of Stroh model for planar slip leading to fatigue crack initiation [57]

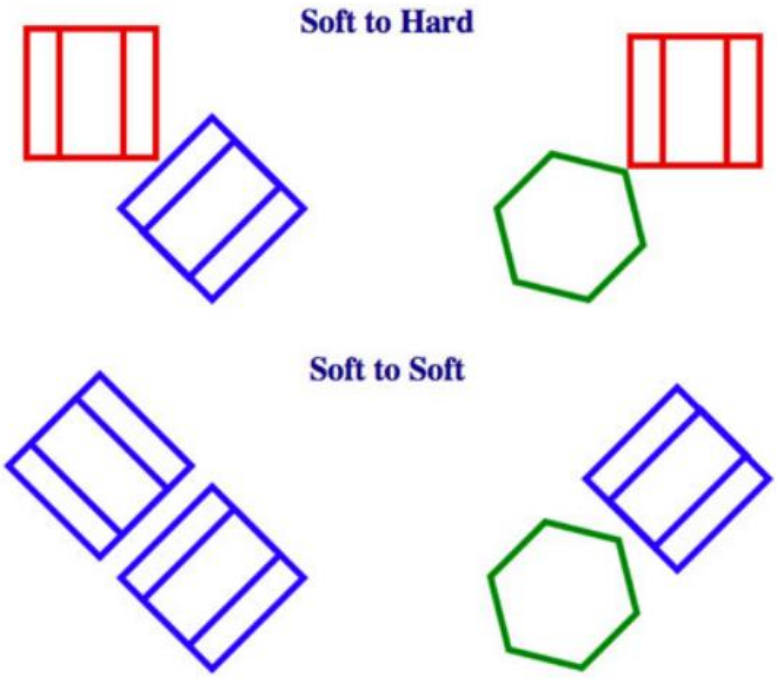

Figure 2.12: Schematics of examples of neighbor grain configurations for which basal plane facet formation was observed. Hard-soft grain pairs are thought to be the most detrimental to fatigue life. [56]

2.2.2 Small Crack Growth Behavior

The phenomenon of small or short fatigue cracks was first studied by Pearson [58]. It was observed that short crack growth rates and long crack growth rates did not correlate using linear elastic fracture mechanics. Since then, many researchers have studied small crack growth behavior and fatigue life prediction based on fracture mechanics [59-64]. It is commonly accepted that small cracks grow at higher crack growth rates than long cracks under the same nominal driving force, and can grow at stress intensity factors below the long crack threshold ("the small crack effect"). In general small cracks are defined in one of the following ways [62].

(1) Microstructurally small cracks: Cracks small compared to microstructural dimensions

(2) Mechanically small cracks: Cracks small compared to the scale of local plasticity

(3) Physically small cracks: Cracks are simply physically small (< 1mm)

(4) Chemically small cracks: Cracks can be up to 10 mm long, depending on the crack-tip environment

In this dissertation work, as in much of the literature, the terms "small" and "short" are used synonymously. A schematic fatigue crack growth rate dc/dN vs. ΔK plot that highlights the problem of small cracks is shown in Figure 2.13.

The cause of the small crack effect is not well understood. Suggested causes for the observed faster crack growth rates compared to longer cracks are the absence of crack closure effects and a breakdown of microstructure similitude. The significant variability of crack growth rates for small cracks growing in the near threshold regime is generally attributed to microstructure dissimilitude, characterized by a situation in which the crack front does not sample enough grains to be indicative of the average material properties. In such cases, the properties of the individual grain in which the crack is growing become critical to crack growth behavior.

Conversely, long cracks have very little scatter in their fatigue crack growth rates. Lankford observed that small cracks decelerate as they approach grain boundaries [60]. He proposed that the deceleration was not due to the grain boundaries, but rather the crystallographic orientation of the adjacent grain. This happened in response to the crack needing to propagate on a different plane in the adjacent grain. Cracks were also observed to arrest at certain grain boundaries. Initiation sites at these locations indicated the crack re-initiated in order to propagate into the adjacent grain.

While there have been many investigations on fatigue crack growth in titanium alloys, much of this work was completed on the study of long cracks [65-69]. Furthermore, attempts to link microstructure to fatigue crack growth behavior were done at the macroscopic scale (i.e. the crack growth resistance of one particular microstructure to another). The role of microstructure on small crack growth rate variability in titanium alloys at the micro-scale needs further exploration. Some findings in this area are discussed in the following section.

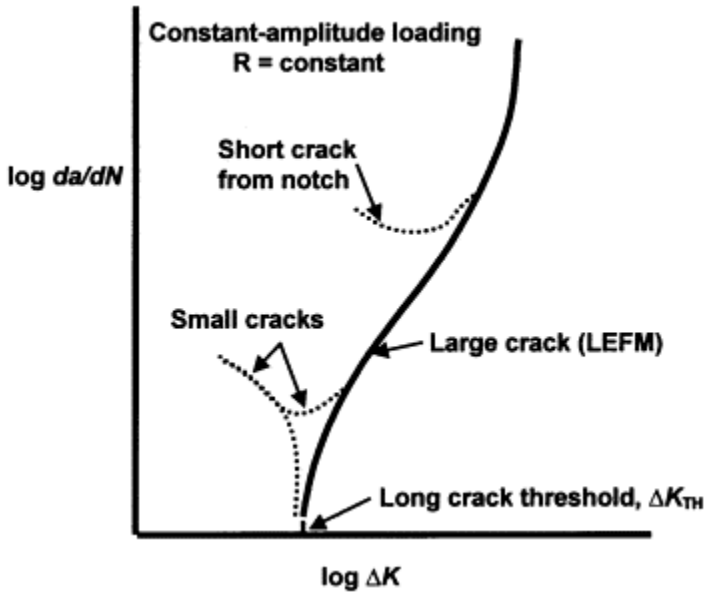

Figure 2.13: This schematic shows the small crack effect where the growth rates of small cracks can sometimes be higher than expected based on long fatigue crack growth rates. [70]

2.2.2.1 Microstructural Effects on Small Fatigue Crack Growth in Titanium Alloys

Published studies regarding the link between local microstructure and small fatigue crack growth behavior remain limited. One finding is that small fatigue crack growth rates are determined by the relative twist between active slip planes in adjacent grains [71]. As a fatigue crack propagates from one grain to another, if a large deflection of the crack is required, the crack can decelerate or arrest. However, at grain boundaries that were well aligned where little deflection of the crack was needed, no decreases in crack growth rate were observed [71]. The work of Marx et al. [72] that investigated small crack growth behavior from FIB notches in a nickel based superalloy is in agreement with this finding. They also observed that cracks decelerate at grain boundaries with high misorientations between the active slip planes. In regards to α/β titanium alloys in particular, an investigation by Saleh and Margolin [73] highlighted the significance of the Burgers orientation relationship and showed that α/β phase boundaries do not allow easy slip transfer across these boundaries and can retard crack growth also. More recent work by Szczepanski et al. [74] investigated the role of microtextured regions and local microstructure on small fatigue crack growth rates in a textured and an un-textured $\alpha + \beta$ Ti-6Al-2Sn-4Zr-6Mo alloy. In this study, no correlation between crack growth rates and the local texture was observed in either microstructure. They concluded that the local textures studied were not severe enough to influence fatigue crack growth rates and the two-dimensional characterization method used may not effectively describe the local microstructure.

Jin and Mall also reported on the breakdown of microstructure similitude leading to a small crack effect in a coarse, lamellar Ti-6242S alloy [75]. No crack closure measurements were made, so it is not possible to rule out roughness induced closure as a cause for the observed small crack effect. Sinha investigated closure effects in a mill-annealed Ti-6Al-4V material and found

that coarser lamellar structures had a higher degree of closure and slower propagation rates (R = 0.1) [76]. They also noted that the increased tortuosity of the fracture surface correlated with the observed increase in fatigue crack growth resistance due to crack deflection.

Researchers have investigated the nature of slip at the crack-tip as another process that might enhance understanding of the small crack effect. Bowen investigated the effects of crystallographic orientation on crack growth rates in a strongly textured Ti-6Al-4V [77]. Deformation was observed to be symmetric about the crack, leading to nominally flat fracture surfaces and lower fatigue crack growth rates. It was reasoned that symmetric deformation at the crack-tip acts as a toughening mechanism, thereby increasing the ability of the microstructure to accumulate more cycles before crack advance. Cracks grew faster in specimens where asymmetric deformation was observed at the crack-tip since slip damage was concentrated on one specific slip system. The work of Krupp et al. on a β titanium alloy is in agreement with these findings [78]. They also observed that if a single slip system was activated the crack growth would be fast, but if multiple slip systems were activated this would decelerate the propagating crack.

2.2.3 Very High Cycle Fatigue Behavior

Very high cycle fatigue (VHCF) is characterized by loading at low stresses, where nominally elastic deformation occurs and localized damage accumulation at the microstructural level characterizes fatigue behavior. The regime of VHCF is commonly considered to be 10^7 to 10^9 cycles. The study of VHCF is of growing importance because of the recent development of components used in applications that will require increasingly long lifetimes.

Conventional methods of designing a component to a fatigue limit are not valid in the VHCF regime, since fatigue failures have been observed to occur below this limit as shown in Figure

2.14 [79]. This has led some researchers to propose a modified S-N curve highlighting the surface failures that tend to occur at high stresses and the subsurface failures that can occur at low stresses and very long lives beyond the fatigue limit. The dominating stage of fatigue lifetime in the VHCF regime is crack initiation. Mughrabi explained failures in the VHCF regime as a result of a fatigue damage accumulation mechanism [80]. He suggested that even though the macroscopic strain is nominally elastic, and below the persistent slip band (PSB) threshold, slip irreversibility can still occur and lead to fatigue failure. This is in agreement with work by Lukas et al. that argued that the applied strain is nominally elastic, but localized plastic deformation will accumulate at specific microstructural sites [81]. This makes VHCF failure mechanisms fundamentally different from low cycle fatigue, in which a majority of the microstructure undergoes some degree of plastic deformation. In VHCF, fatigue damage mechanisms are much more sensitive to microstructural variability and localized damage accumulation at key sites control fatigue life. Studies have shown these microstructural sites can be hard phases, such as inclusions, large phases, specific grain-grain boundary relationships, or microtextured regions. Additionally, the microstructural neighborhood responsible for failure is sensitive to other properties, such as distance from the specimen surface, spatial orientation, and grain size effects.

Natural crack initiation of micro-cracks at microstructural features does not guarantee the continued propagation of the crack. Many factors, such as grain size, grain orientation, and grain boundary orientation determine the favorability of crack propagation. It has been shown that a single fatigue specimen can possess multiple sites of crack initiation, where cracks did not propagate past a critical microstructural barrier [8].

An increased likelihood of subsurface crack initiation in the VHCF regime has been reported for high strength steels [82] and titanium alloys [83, 84]. The reasons for this behavior have been attributed to the presence of compressive residual stresses at the surface, the probability of finding the critical microstructural neighborhood for fatigue failure being higher in the volume than the surface, and environmental effects.

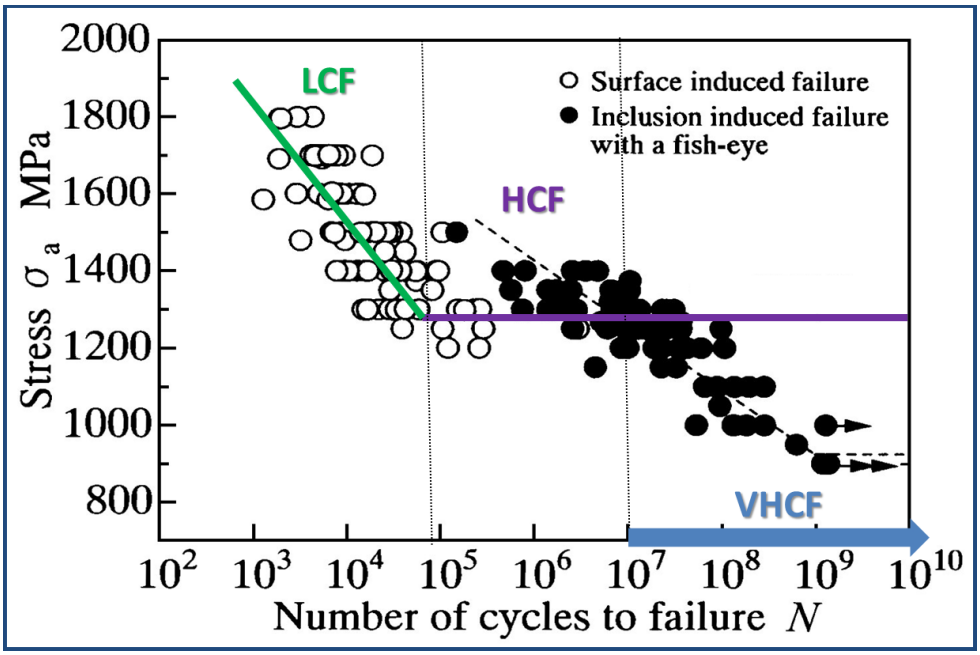

Figure 2.14: S-N data on a high strength steel gathered by Sakai et al. that shows fatigue failures occurred below the fatigue limit at very long lives. The failure also switched from surface to subsurface. [3]

2.2.3.1 Surface vs. Subsurface Fatigue Crack Initiation

Surface and subsurface fatigue crack initiation behavior depends on test conditions and environment. At high stresses, fatigue crack initiation typically occurs at slip bands at the surface. At lower stresses, cracks can initiate from surface slip bands or from interior regions. Work by Gilbert and Piehler shed light on this competition by removing the effect of testing conditions [85]. Under cyclic bending, where stresses are higher at the surface, cracks were found to initiate at both the surface and subsurface, with both being attributed to local grain

orientations. Interestingly, none of the fatal cracks initiated from subsurface locations, even though an arrangement favorable for slip transfer was found. This could point to an environmental effect in which surface crack growth in air is favored over subsurface cracking in a vacuum-like environment. Sinha and Larsen investigated the vacuum levels needed to simulate the vacuum environment that a subsurface crack would experience using thermodynamic calculations [86]. It was reported that the vacuum level needed to avoid oxidation of fresh Ti surfaces is orders of magnitude below the capability of state of the art vacuum systems. Thus, a change in fatigue behavior may still occur at lower vacuum pressures, closer to subsurface behavior where no oxidation is expected. Further development of the mechanisms of surface and subsurface crack initiation and growth processes in relation to environmental effects is necessary. The role of environment in the fatigue behavior of titanium alloys is discussed in Section 2.3.1.

2.3 Fatigue of Titanium Alloys – Frequency Effects

The effects of frequency on fatigue behavior can be manifested in the form of a strain rate effect and an environmental effect. Some materials exhibit longer fatigue lifetimes at ultrasonic testing frequencies than at lower, conventional test frequencies. The difference in lifetime is usually attributed to strain rate effects or time-dependent environmental effects, stemming from humidity, temperature, or atmospheric composition.

The reports regarding frequency effects in titanium alloys are inconclusive. Ritchie et al. did not observe a frequency effect in Ti-6Al-4V when tested at frequencies between 50 Hz and 1 kHz [70]. This was in agreement with work carried out by Davidson on the same material at 1.5 kHz where no frequency effect was observed on fatigue crack growth rates in air [87]. Additionally, no intrinsic frequency effects on threshold and near threshold fatigue crack growth

rates were observed in Ti-6Al-4V when tested at 20 Hz and 20 kHz in air by Stanzl-Tschegg [88]. Roth et al. proposed that strain rate effects are more significant in materials with few available slip systems [89], and therefore, hcp materials are more susceptible to strain rate effects than fcc or bcc materials. Some researchers have also speculated that two phase materials, such as duplex titanium alloys may be more susceptible to strain rate effects due to the frequency dependence of incompatibility stresses at the α/β boundaries [90].

2.3.1 Environmental Effects

Table 2.1 summarizes the test conditions and relevant findings from investigations of environmental effects on fatigue in titanium alloys. The majority of these experiments focus on the effects of water vapor, oxygen, and hydrogen gases. It should be noted that most of these studies examined low cycle ($< 10^4$ cycles) and high cycle ($10^4 – 10^7$ cycles) fatigue behavior at lower frequencies. Studies that compared fatigue crack propagation in air versus vacuum [91-97] consistently showed that fatigue cracks propagated up to three orders of magnitude slower in vacuum, below ~ 1 Pa, than in air. Work by Demulsant and Mendez [93], also showed that fatigue crack initiation was delayed in vacuum compared to air in a Ti-6Al-4V and Ti-6246 alloy in the low cycle fatigue regime. Increased fatigue crack growth rates (FCGRs) in air versus vacuum in titanium alloys are mostly attributed to the deleterious effects of water vapor and oxygen.

2.3.1.1 Effects of Water Vapor and Oxygen

The processes responsible for increased fatigue crack growth rates in titanium alloys due to water vapor and oxygen are not completely understood. Internal oxygen has been shown to significantly increase crack growth rates, whereas the role of gaseous oxygen remains debated. Bache et al. [97] studied the role of internal oxygen content on ambient temperature fatigue

crack propagation in a Ti–6Al–4V alloy at 13.3 Pa and concluded that oxygen was responsible for the increase in growth rate, partially through enhanced facet formation. They suggested that oxygen reduces the stacking fault energy in titanium, promoting single slip and increasing fatigue crack growth rates. Sarrazin-Baudoux et al. [95] investigated the effects of water vapor and oxygen on fatigue crack growth in Ti-6242 at 550 °C and showed that humidified argon substantially increased fatigue crack propagation rates compared to that of humidified argon with added oxygen. They argued that oxygen limits the effects of water vapor on the oxide layer formation that results primarily from water vapor dissociation. Work by Gao et al. [98] studied the effects of water vapor and oxygen on fatigue crack growth in Ti-5Al-2.5Sn and Ti-6Al-4V at room temperature. The results showed that reactions with water vapor and oxygen were both rapid with only a monolayer of TiO being produced in water vapor compared to an oxide layer in oxygen that was two to three layers. They concluded that the process for increased FCGRs in water vapor was adsorption of water vapor molecules on fresh Ti surfaces, oxide layer formation from a dissociation reaction of Ti and water vapor, and embrittlement by hydrogen produced by this reaction. The enhanced fatigue crack growth response was shown to adhere to a transport controlled crack growth model. These results indicate that formation of an oxide layer may be a critical process contributing to increased crack growth in the presence of water vapor and gaseous oxygen.

2.3.1.2 Effects of Hydrogen

Titanium and titanium alloys have a well-documented incompatibility with gaseous hydrogen. However, the role of hydrogen in the fatigue behavior of titanium alloys is not yet resolved. Studies have shown that gaseous hydrogen can decrease fatigue resistance at room temperature [99-102]. A review of the literature indicates that the effects of hydrogen on fatigue behavior of titanium alloys can be summarized by two mechanisms:

1. Fracture by localized plastic deformation enhanced by the presence of hydrogen, or HELP, where hydrogen reduces the stress needed for dislocation motion; and
2. Brittle fracture of the stress induced titanium hydride phase that precipitates near the crack-tip.

Determining which, if either, of these two mechanisms is active depends on numerous factors including microstructure, stress intensity, strain rate, gas pressure, and temperature. Hydrogen has been shown to readily adsorb and penetrate titanium and its alloys at room temperature. Hydrogen diffusion has also been shown to induce lattice strain and enhance dislocation motion even at low concentrations. Nelson et al. [103], observed a difference in hydrogen embrittlement mechanisms at room temperature in a Ti-6Al-4V alloy with changes in stress intensity. Hydrogen transport was found to be the rate determining mechanism, becoming more significant at low strain rates. They postulated that if the strain rate were too high essentially no hydrogen is transported to the reaction site and no embrittlement occurs. Their results also suggest a strong microstructural influence on diffusion rates, in line with previous observations that hydrogen diffusion in the beta phase is several orders of magnitude more rapid than the alpha phase [104]. Work by Moody et. al. [105] exploring the effects of internal hydrogen on a Ti-6Al-6V-2Sn alloy is in agreement with the work of Nelson et al. Slow crack growth was observed to proceed

by a process in which hydrogen accumulates at the crack-tip, saturation is reached, strain-induced hydrides form, and the local stress intensity is altered by the local microstructure. Hydrogen diffusion through the beta matrix was suggested to control the crack growth process and a significant temperature and microstructure dependence was observed. A study by Shih et al. [106] provided a deeper understanding of hydrogen embrittlement in an α titanium alloy using *in-situ* TEM experiments. The nucleation and growth of hydrides near crack-tips was observed *in-situ* at low stress intensities and the accommodation of the stress field around the hydride was observed to be partially elastic and partially plastic. A hydride nucleation-growth-cleavage mechanism for crack advance is described in which a crack propagates once the local stress exceeds the critical stress for hydride fracture. These studies, while important, were carried out on TEM specimens and results obtained from experiments with more conventional bulk specimens may differ. For example, an internal hydrogen study done by Evans et. al. [107] on a near alpha titanium alloy (Ti-6Al-5Zr-0.5Mo-0.25Si) concluded that hydrogen atoms modify dislocation behavior, particularly at lower concentrations. An increase in strength and a reduction in ductility were observed for increasing hydrogen ppm at low concentrations, but at high concentrations they induce additional failure events. This appears to differ from the observation of Shih et. al. regarding an increase in dislocation mobility with gaseous hydrogen. However, strain-induced hydride formation is proposed to account for the early failure mechanism observed for the higher hydrogen concentrations.

2.3.1.3 Environmental Effects of Other Gaseous Species

During low cycle fatigue at low frequencies it is also likely that atoms and molecules of other gases, not just water vapor, play an important role in fatigue crack propagation behavior. Sarrazin Baudoux et al. [92] studied the effects of other gaseous environmental species,

including water vapor, on fatigue crack propagation in a Ti-6Al-4V alloy at frequencies from 0.5 to 35 Hz. They observed similar fatigue crack growth rates in ambient air (P_{H2O} = 1.3 kPa) and humidified nitrogen (P_{H2O} = 1.3 kPa) as shown in Figure 2.15. Interestingly, dry nitrogen at 1 x 10^5 Pa (P_{H2O} = 1.6 Pa) had only a slightly lower fatigue crack growth rate than ambient air and humidified nitrogen, suggesting an effect of nitrogen, as well as water vapor, on fatigue crack propagation in Ti-6Al-4V as shown in Figure 2.16. Work by Shimojo et al. [94] is in agreement with this finding. They also examined the effects of nitrogen on fatigue crack growth, but in pure titanium using Auger electron spectroscopy. They discovered an increase in the concentration of nitrogen in the plastic zone, especially the cyclic plastic zone, in samples fatigued in high purity nitrogen gas at 1 x 10^5 Pa. It was suggested that the increased nitrogen concentration in the cyclic plastic zone was the result of nitrogen atoms being transported into the material during reverse slip processes. A schematic of the proposed process is shown in Figure 2.17. In a related study [108], the same group studied the effects of inert gases on fatigue crack propagation rates in pure titanium. An increase in fatigue crack growth rates over vacuum was observed for all of the inert gases studied at a pressure of 1 x 10^5 Pa, with rates being similar to that of nitrogen gas. Auger electron spectroscopy also revealed an increase in the inert gas concentration in the cyclic plastic zone and crack wake. They postulated that inert gas atoms may not chemisorb on fresh crack faces, but may physisorb and be transported into the plastic zone during reverse slip, causing increased irreversibility and higher crack growth rates.

Smith and Piascik [91] conducted a study of the effects of O_2, H_2O, N_2, and He gases on fatigue crack growth behavior in an $\alpha + \beta$ Ti-6Al-2Zr-2Cr-2Sn-2Mo-0.2Si alloy. Interestingly, results of room temperature fatigue tests in nitrogen and helium at lower pressures than Shimojo et. al. and Sarrazin Baudoux et. al. from 10^{-1} Pa to 2 Pa exhibited similar FCGRs as those of

ultra-high vacuum (UHV) tests at $< 7 \times 10^{-7}$ Pa suggesting no influence of nitrogen or helium on fatigue behavior at these pressures. This is in contradiction to the work of Shimojo and Sarrazin Baudoux and may indicate a pressure dependent mechanism is at work even in the presence of inert gases. The differences in the material compositions studied may also account for the differences in the effects of nitrogen and helium gas.

All of these studies were on long cracks tested in the low cycle fatigue regime. One cannot overlook the increase in plasticity and the size of the plastic zone of these cracks grown in the low cycle fatigue regime when compared to small cracks grown under the low stresses characteristic of very high cycle fatigue (VHCF). Especially since studies have indicated environmental effects are usually more pronounced during plastic deformation [109]. The transport of molecules and/or atoms to the crack-tip and diffusion of atoms into the small plastic zones associated with small cracks grown under VHCF, as in the present work, are discussed in Chapter 4.

Table 2.1: Summary of prior investigations on environmental effects in titanium alloys

Reference	Material	Temperature	Environment	Crack Regime	Findings	Conclusions
Smith and Piascik [91]	Ti-6Al-2Zr-2Cr-2Sn-2Mo	24 °C and 177 °C	Vacuum (7 x 10^{-7} Pa); Ambient air; O_2, N_2, He, H_2O	Long; LCF; R = 0.5, 0.75; f = 5 Hz or 0.5 Hz	• No change in FCGR from UHV to P_{H2O} of 10^{-2} Pa • Factor of 2 increase in FCGRs in P_{H2O} from 10^{-2} to 10^{-1} Pa • No change in FCGR from UHV to P_{O2} of 10^{-2} Pa • Factor of 2 increase in FCGRs in P_{O2} of 10^{-1} Pa • For P_{O2} >10^{-1} Pa FCGRs decrease with increasing P_{O2} until P_{O2} = 2 Pa, followed by constant FCGR to 600 Pa • P_{N2} and P_{He} from 10^{-1} Pa to 2 Pa had same FCGR as UHV • XPS analysis of crack surfaces from P_{H2O} = 67 Pa indicate dominance of hydroxide vs. oxide film	• Oxygen and water vapor both contribute to increased FCGRs in air • Nitrogen does not directly affect the fatigue crack growth in air • Three distinct regions of environmentally assisted crack growth: (1) inert at low pressures, (2) adsorption dominated, (3) oxide and hydrogen embrittlement region
Gaddam et. al [99]	Ti-6Al-4V	24 °C	Ambient air, P_{H2} = 15 MPa (high pressure)	Long; LCF; R = 0; f = 0.5 Hz	• Similar FCGR in air and high pressure H_2 up to ΔK ≈ 20 MPa √m, followed by large increase in FCGR with increasing ΔK	• At low ΔK, crack growth in hydrogen is dominated by same mechanism as in air due to low interaction of hydrogen
Ding et. al [96]	Ti-6Al-4V, Ti-4.5Al-3V-2Mo-2Fe	24 °C	P_{H2} = 0.245 MPa, Vacuum (1.3 Pa)	Long; R = 0.1, 0.5; f = 5-20 Hz	• Lower FCGRs in both H_2 and vacuum than in air • Similar crack growth rates in hydrogen and air at higher stress ratios (more brittle fractures alleviated crack deflection effects)	• A deflected crack path in hydrogen, resulting from localized brittle fractures in the α phase caused lower FCGRs. Decrease in occurrence of facets was cause in vacuum
Bache et. al [97]	Ti-6Al-4V	24 °C	P_{H2} = 13 Pa P_{Ar} = 13 Pa Vacuum (1.3 Pa, 1.3 x 10^{-4} Pa)	Long; R = 0.01; f = 1 Hz or 5 Hz	• FCGRs at 1.3 Pa similar to those in atmospheric air • Significantly lower FCGRs at 1.3 x 10^{-4} Pa • Reduced FCGRs in H_2 and Argon	• H_2 and Argon act to shield the crack tip from more detrimental species • Oxygen reduces SFE, promoting single slip, and increasing FCGRs

Table 2.1: Continued

Reference	Material	Temperature	Environment	Crack Regime	Findings	Conclusion
Sarrazin-Baudoux [92]	Ti-6Al-4V	24 °C, 300 °C	Ambient air, Dry N_2,Humidified N_2 (P_{TOT} = 10^2 kPa, P_{H2O} = 1.3 kPa), Vacuum (3 x 10^{-4} Pa),	Long; R = 0.1; f = 0.5 - 35 Hz	• Lower FCGRs in vacuum than air • (Intrinsic) Facet orientation lies within the basal planes of the alpha phase • Nearly identical FCGR in humidified nitrogen and air	• Two controlling mechanisms: an adsorption-assisted propagation and an additional H assisted propagation
Demulsant and Mendez [93]	Ti-6Al-4V/Ti-6246	24 °C	Vacuum (10^{-4} Pa), Lab air	Initiation/Short cracks; LCF; R = -1; f = 0.25 Hz	• Delayed crack initiation in vacuum compared to air • Surface crack densities lower in vacuum than air • Crack initiation sites modified by air in Beta forged Ti • Retardation of cracks longer in vacuum than air	• Environment tends to decrease the effect of microstructural barriers hence favoring crack growth and less branching • Mechanical sliding near the basal plane leads to stage 1 like propagation and cleavage like initiation • Internal fatigue crack initiation associated with concentration of hydrogen due to local stress
Pilchak and Williams [110]	Ti-8Al-1Mo-1V	24 °C	Lab air, 3.5 % NaCl	LCF; R = 0.1; f = 30 Hz	• Fatigue crack initiation occurred at surface in a grain whose basal pole was inclined 25° to the loading • Propagation also occurred on basal planes inclined between 22° and 41° • Increase in dwell fatigue life with increasing internal hydrogen content • Fracture surface roughness and FCGR increase with increasing crack length consistent w/ plasticity controlled cracking	• The role of hydrogen during dwell fatigue needs further study • Effect on microtexture region size is greater than effect of bulk hydrogen concentration up to 230 ppm • Facet surface topography from static air tests was consistent with that formed by cracking in H_2 gas (tear ridges extending in direct of crack propagation)

Table 2.1: Continued

Reference	Material	Temperature	Environment	Crack Regime	Findings	Conclusion
Shimojo et. al. [94]	Pure Ti	24 °C	Vacuum (3 x 10^{-5} Pa), N_2, He, Ar, air 20% RH	Long cracks; R = 0.1; f = 10 Hz	• Concentration of nitrogen in plastic zone, esp. cyclic plastic zone, increased significantly in N_2 gas • FCGR in inert gas higher than vacuum • FCGR in all gaseous environments similar • Micro-crack occurrence increases with increasing environmental activity	• Gases adsorb on freshly formed crack faces, and diffuse into the CPZ during cyclic dislocation motion • Environmental gases including inert gases enter the plastic zone around the crack-tip • No obvious difference in fracture surface morphology at pretty high ΔK
Shimojo et. al. [108]	Pure Ti	24 °C	Vacuum (3 x 10^{-5} Pa), He, Ne, Ar, Kr, Xe	Long cracks; R = 0.1; f = 10 Hz	• Increased FCGR and change in fracture surface appearance for cracks grown in inert gases • Auger electron spectroscopy confirmed presence inert gases in subsurface regions of fracture surface	• Transport of inert gas atoms into the crack-tip plastic zone by reverse slip of slip planes at the crack on which atoms have physisorbed
Sarrazin-Baudoux et al. [95]	Ti-6242	550 °C	Ambient air, Vacuum, humidified Ar, humidified Ar plus O_2, humidified N_2 plus O_2	Long; R = 0.1; f = 0.05 - 35 Hz	• FCP in inert environment is a transgranular stage II crack • Humidified argon is worse than humidified synth air • At increasing ΔK the environmental assistance decreases then vanishes a high ΔK • At above 10 Hz behavior in humidified gas is similar to vacuum	• Moderating effect of oxygen – water vapor is the detrimental species • Controlling mechanism is adsorption assistance in the mid-rate range and hydrogen assistance in the near threshold

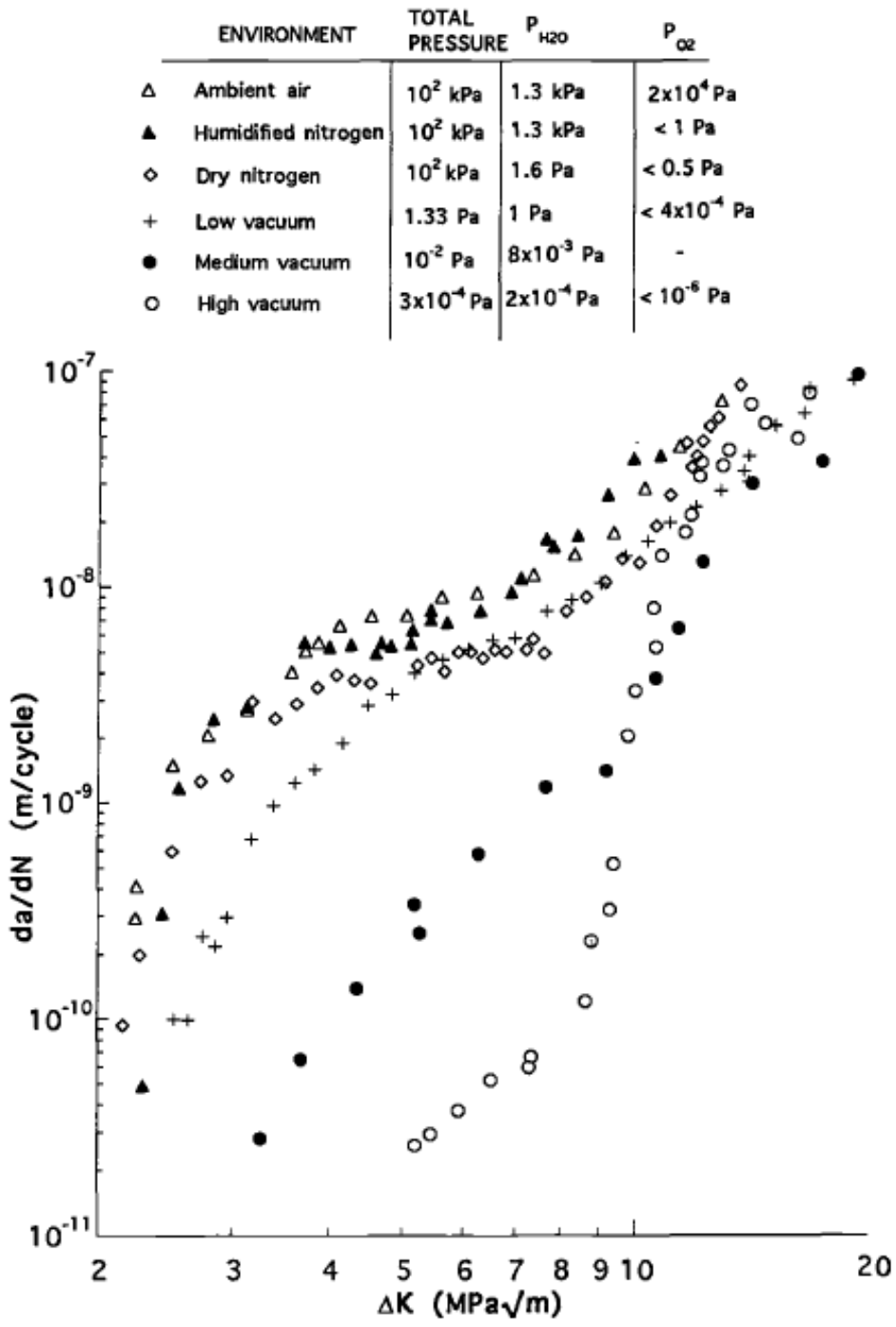

Figure 2.15: Crack growth rate data from fatigue of Ti-6Al-4V, at R = 0.1 and 35 Hz showing the effects of partial pressures of water vapor and oxygen are shown. [111]

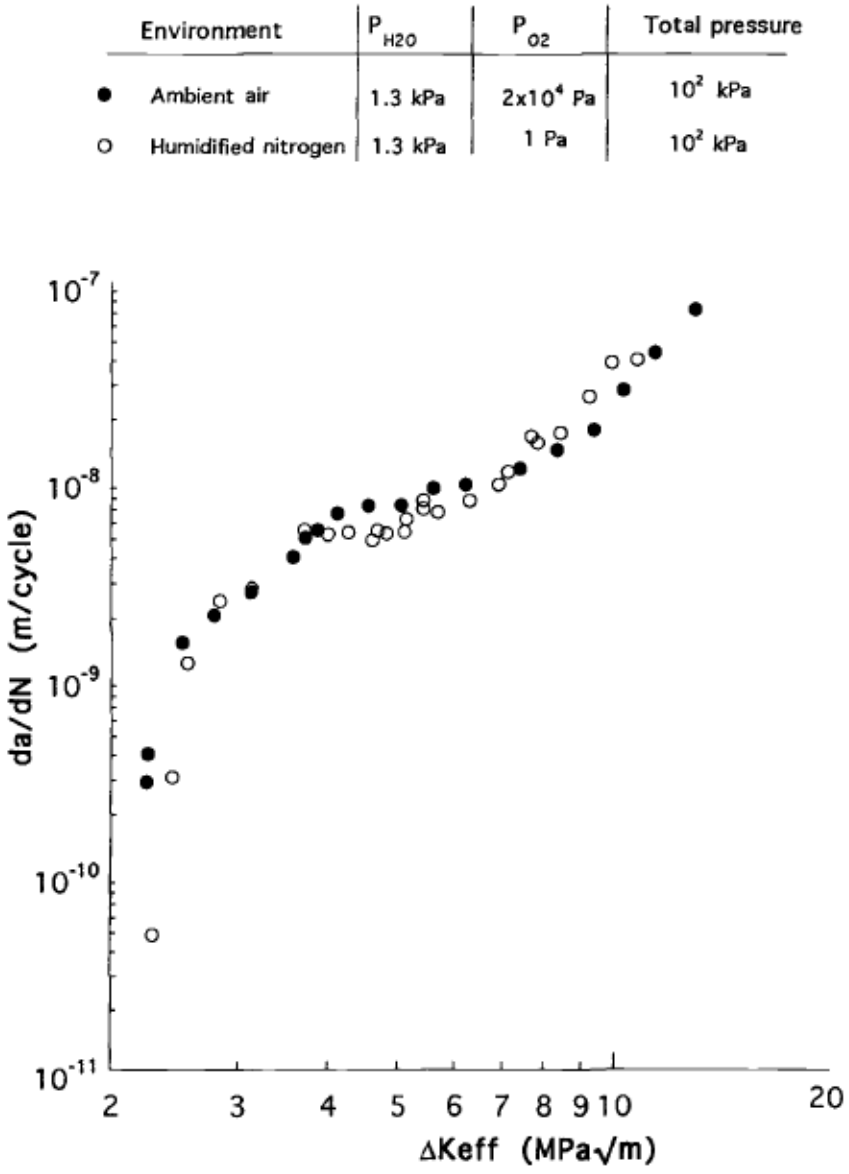

Figure 2.16: Crack growth rate data from fatigue of Ti-6Al-4V, at R = 0.1 and 35 Hz showing similar fatigue crack growth rates for ambient air and humidified nitrogen [111]

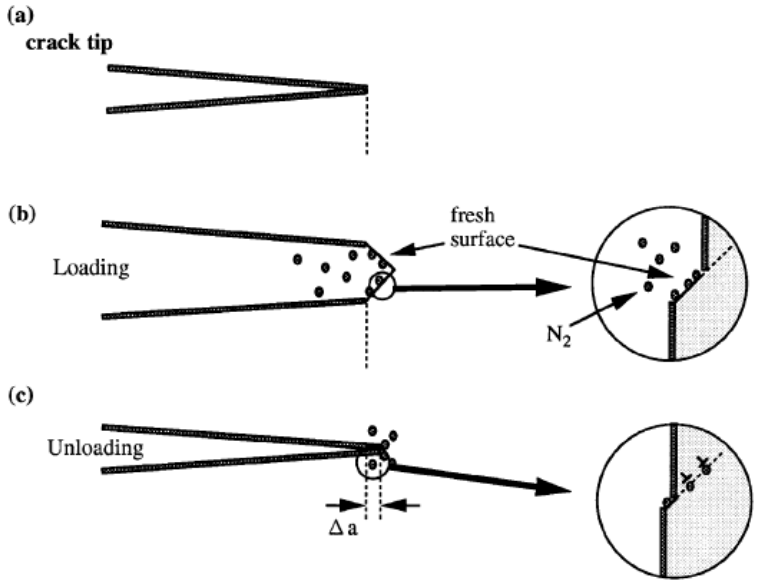

Figure 2.17: A schematic diagram of the model for nitrogen entry into the plastic zone during fatigue of pure titanium is shown. (a) a fatigue crack-tip, (b) Nitrogen adsorption onto fresh surfaces produced during the loading cycle of the crack-tip, (c) Nitrogen entry during the unloading portion of the cycle [94]

2.3.1.4 Environmental Effects in Ultrasonic Fatigue

Fatigue in the very high cycle fatigue regime (>10^7 cycles) poses additional challenges in component design when considering the significant influence of microstructural variability with environmental effects. A limited number of studies has been performed to investigate the role of environment in fatigue crack growth in materials under ultrasonic fatigue loading (at 20 kHz). These studies showed that environmental species, mainly water vapor, have a significant effect on fatigue behavior even at ultrasonic frequencies. In work done by Stanzl, Mayer, and Tschegg [112], the environmental effects associated with humid air, dried air, and vacuum on fatigue crack propagation in the aluminum alloy 2024-T3 was studied at a loading frequency of 20 kHz. An approximately one order of magnitude increase in fatigue crack growth rates in humid air (40% - 60% relative humidity) over vacuum (< 10^{-1} Pa) was observed below 10^{-9} m/cycle.

Stanzl-Tschegg et al. [88] found a pronounced influence of air humidity on near threshold fatigue crack growth rates in the aluminum alloy 7075-OA and Ti-6Al-4V at 20 kHz. Their calculations indicated that time-dependent environmental effects are fully effective at increasing crack growth rates over vacuum and expected, even at 20 kHz ultrasonic testing at fatigue crack growth rates below approximately 10^{-9} m/cycle. The rate controlling processes of water vapor and hydrogen diffusion, as well as the time needed to generate a monolayer of water vapor molecules at the crack-tip, were considered. Additionally, no intrinsic frequency effects on threshold and near threshold fatigue crack growth rates were observed in Ti-6Al-4V. Zhu et al. [113] studied the effect of environment on small crack growth in a cast aluminum alloy at 20 kHz, and also found that the fatigue crack growth rate increased with increasing water vapor pressures. A model was proposed that assumes a hydrogen-induced increase of fatigue crack growth rate, in which the hydrogen concentration is determined by the transport of water molecules to the crack tip, deemed the rate-determining step. A correlation between the estimated hydrogen concentration and fatigue crack growth rates was reported as shown in Figure 2.18.

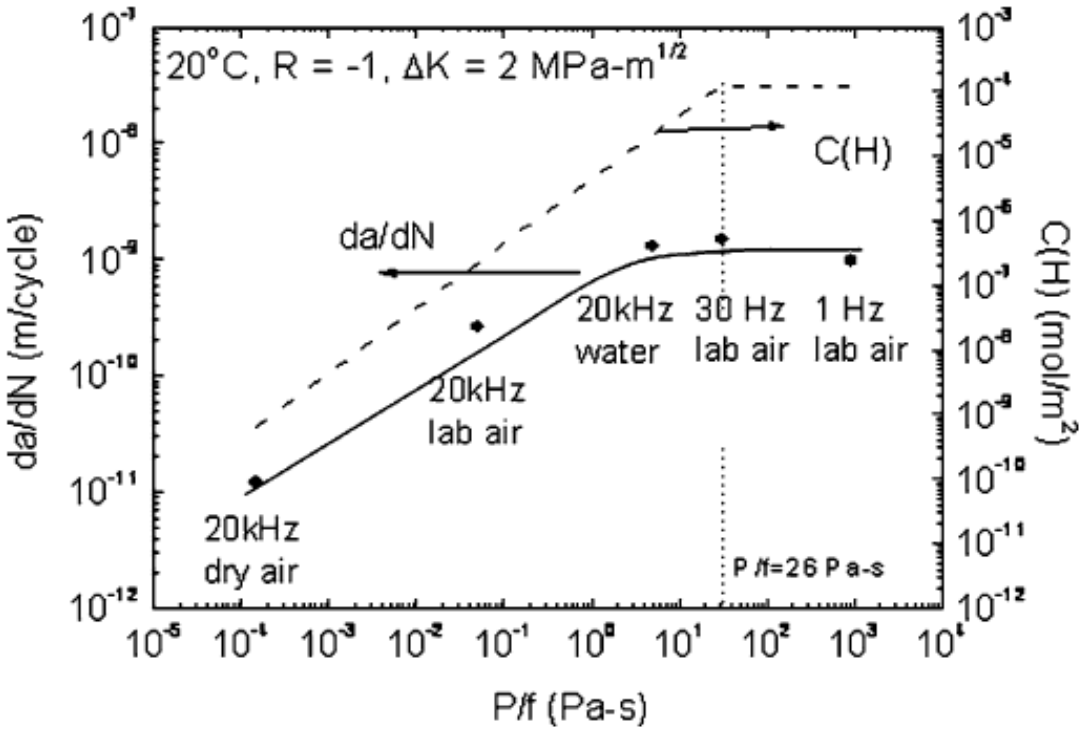

Figure 2.18: Dependence of crack growth and estimated hydrogen concentration of water exposure of a cast aluminum alloy at 20 °C. Data is also shown for ultrasonic fatigue at 20 kHz. [114]

2.4 Oxidation of Titanium and Titanium Alloys

Many investigations of the influence of ambient air, water vapor (humidity), and oxygen gas on fatigue crack growth rates in titanium alloys cite oxidation of newly created surfaces at the crack-tip as a critical step in the process leading to accelerated crack growth compared to vacuum. This is plausible given that bare titanium is highly reactive and forms an oxide layer instantaneously with exposure to these gases even at very low pressures ($<10^{-7}$ Pa). This section reviews relevant literature regarding the oxidation kinetics of titanium alloys exposed to these gases at various pressures and temperatures because oxidation may affect fatigue behavior even at ultrasonic frequencies at room temperature.

2.4.1 Oxidation in Air

Titanium forms a spontaneous passive, oxide layer when exposed to air. Titanium oxidation is characterized by fast oxygen adsorption and a slower oxygen uptake until saturation [115-118]. In atmosphere, an oxide layer is formed within microseconds. The native oxide is primarily TiO_2, which forms readily due to a high heat of reaction. The nearly impenetrable surface air formed oxide layer ranges from 2-7 nm in thickness. The titanium oxide layer can also be described as self-healing. For example, oxide that is formed on new crack faces is continuously broken and "healed" with the opening and closing of the crack. The adhesion properties of the oxide are controlled by the oxide thickness, oxidation temperature, and nitrogen influence. Adhesion in air was found to be greater than in pure O_2 [119]. The strength of oxide layer adhesion also decreases with thickness and as temperature increases.

Reports on the composition of the oxide layer formed on Ti-6Al-4V surfaces using XPS confirm TiO_2 is the top layer of the oxide with small amounts on suboxides below [120, 121]. These studies also showed that alloying elements can be found in their oxide forms. For

example, aluminum oxide was measured near the beginning of oxide formation in a Ti-6Al-4V alloy under ultra-high vacuum conditions [120]. The role of the alloying elements in oxide layer formation cannot be ignored.

2.4.2 Oxidation in Water Vapor

The effects of moisture levels in atmosphere and at low pressures on oxidation kinetics has been studied in many metallic materials including aluminum alloys, magnesium alloys, high strength steels, and titanium alloys. In titanium alloys, water vapor reacts with fresh titanium surfaces to produce a stable oxide layer, similarly to exposures with pure oxygen. However, no titanium oxides higher than TiO are observed with water vapor exposure to pure titanium surfaces at room temperature [122]. Furthermore, exposure to water vapor leads to the presence of hydroxides within the oxide layer. It is commonly accepted that most transition metals dissociate chemisorbed water at room temperature. This dissociation may be complete or partial or a combination of the two. Because oxidation by O_2 is more severe than by H_2O at room temperature, H and OH may play an important role in oxide layer formation.

2.4.3 Oxidation in Oxygen

Titanium and titanium alloys are highly reactive metals with high chemical affinities to oxygen [123]. Researchers have investigated the reaction of titanium with pure oxygen [115, 116, 119, 124, 125]. The kinetics of the oxidation reaction with titanium are highly dependent on the pressure as well as the exposure time. Vaquila et al. [116] observed that titanium oxidation proceeds immediately upon exposure to even low pressures of O_2 (3×10^{-9} Torr), with a negligible oxygen adsorption stage. This is consistent with the work of others, who observed a fast adsorption of oxygen at the top most surface layer, followed by a slower uptake of oxygen until saturation [115, 124]. General agreement is that the topmost oxide layer is composed

primarily of TiO_2. However, some researchers have observed lower oxidation states present near the oxide/metal interface. One reason for the differences in the nature of the observed oxidation states is that the ion beam used to sputter the oxide layer for depth profile analysis may also reduce part of the TiO_2 layer to lower oxidation states, such as Ti_2O_3 and in turn to TiO.

Oxidation efficiency also varies with temperature. For example, Gallerie et al. [126], observed oxidation is faster by water vapor than oxygen at 1123K. However, at 300K oxygen appears to be a more efficient oxidizer than water vapor [127].

2.5 Summary

This section summarizes the following key portions of the background and literature review for this dissertation work: processes governing environmental effects of fatigue crack growth behavior, microstructural small crack growth behavior, and fatigue crack initiation mechanisms in relation to microstructure and environment. Identification of the questions that remain unanswered is also discussed.

There have been several studies aimed at understanding the role of gaseous environmental species on fatigue behavior in titanium alloys as summarized in Table 2.1. The majority of these experiments focused on the effects of ambient air, vacuum, water vapor, oxygen, and hydrogen gases on the fatigue behavior of long cracks in the low cycle fatigue regime. Fatigue crack growth rates in air were reported to be orders of magnitude higher than vacuum at conventional frequencies. Limited studies on fatigue crack growth behavior in air versus vacuum at ultrasonic frequencies also showed a significant increase in FCGR with increasing air pressure. As reported in this chapter, the processes responsible for this behavior are mainly attributed to the amount of water vapor in the environment. It is proposed that water vapor molecules arrive at the crack-tip and react with fresh titanium surfaces created by the propagating crack [98]. This reaction may

result in oxygen, hydroxides, and/or atomic hydrogen. The hydrogen diffuses into the plastic zone ahead of the crack-tip where it causes an enhanced crack growth rate. The oxygen and hydroxides from the surface reaction also form an oxide layer that may also contribute to accelerated fatigue crack growth rates.

Fatigue experiments carried out in oxygen and hydrogen gas, separately, have attempted to determine the effects of the respective species. In terms of oxygen, oxidation of fresh crack faces at the crack-tip during the loading portion of a fatigue cycle is thought to impede reverse slip on these planes during the unloading cycle. This increase in irreversibility leads to higher damage accumulation rates at the crack-tip and thus, higher fatigue crack growth rates. There have also been studies that report an effect of internal or diffused oxygen on the titanium lattice, promoting planar slip and thereby, accelerating the FCGR [97]. The correlation of planar slip with higher crack growth rates has been observed by others. Krupp et al. [78] observed that if a single slip system was activated the crack growth would be fast, but if multiple slip systems were activated this would decelerate the propagating crack.

The effects of hydrogen on fatigue crack growth in titanium alloys remains unclear. Two mechanisms are proposed for increased fatigue crack growth rates in the presence of hydrogen: a mechanism of hydrogen enhanced local plasticity (HELP) or a hydrogen embrittlement process involving stress induced hydride formation at the crack-tip. Hydrogen has been shown to readily adsorb and penetrate titanium and its alloys at room temperature. Hydrogen diffusion has also been shown to induce lattice strain and enhance dislocation motion even at low concentrations. Once the hydrogen enters the titanium lattice, which can be aided by the presence of a local stress gradient, the mechanism by which it enhances fatigue crack growth rate depends

significantly on the testing conditions. Specifically, the operative mechanism can depend on many factors including microstructure, stress intensity, strain rate, gas pressure, and temperature.

Investigators have also indicated an increase in the amount of absorbed species such as nitrogen and inert gas atoms at the crack-tip and in the crack wake for long cracks in the LCF regime [94]. Measurements of the surface concentrations of these atoms were obtained using AES on the specimen surface. These investigations provided insight into to entering behavior of atoms at the crack-tip, but questions remain on the relative influence of such a mechanism for the much smaller plastic zones associated with small cracks growing under the nominally elastic stresses of VHCF testing.

Finally, in the study of small fatigue crack growth behavior, especially at low and negative stress ratios, the effects of crack closure may be significant. Indeed, Sinha observed a correlation between a high degree of closure in lamellar microstructures in Ti-6Al-4V and slower propagation rates at $R = 0.1$ [76]. The effects of crack closure are also likely to affect oxidation behavior and crack-tip loading behavior through adhesion and rewelding processes.

Prior to the this dissertation research, no investigation on the effects of laboratory air, vacuum, water vapor, oxygen, and hydrogen on small fatigue crack growth behavior during ultrasonic fatigue has been performed. The limited studies on environmental effects in ultrasonic fatigue testing focused predominantly on the influence of humidity in increasing fatigue crack growth rates and diminishing fatigue life. However, questions still remain regarding the influence of gaseous species, such as water vapor, oxygen, and hydrogen, and the processes governing environmental effects at kHz testing frequencies. Specifically, how do these species affect small crack growth behavior during ultrasonic fatigue? What is the process for increased

fatigue crack growth rates in hydrogen compared to vacuum? What role does oxidation and crack closure play in relation to environmental effects? These issues are addressed in this thesis.

In terms of fatigue crack initiation, the first step is to determine a suitable definition of crack initiation. Hall [42] provides a practical definition based on when a crack begins to behave as a propagating crack. By this definition, crack initiation is determined by the scale of the microstructure, which can range from individual α laths to large α colonies. Hall defines these fatigue critical microstructures as *crack-like discontinuities* (CLD), or the minimum feature size at which the accumulated fatigue damage starts to behave as a small fatigue crack. In general, two processes for fatigue crack initiation have been proposed: a mechanism that involves dislocation pile-up at grain boundaries causing fatigue crack initiation as a result of strain incompatibility, or intragranular fatigue crack initiation facilitated by crack initiating slip bands within the grain. The operative mechanism will certainly depend on the microstructure, but little attention has been given to whether it is environmentally dependent. Additionally, surface and subsurface fatigue crack initiation has been reported for fatigue failures of titanium alloys in the VHCF regime, and it has been postulated that the difference in the environment of these cracks has a significant influence on both the initiation and early propagation behavior. Questions still remain concerning how and whether fatigue crack initiation mechanisms change with respect to environment in the VHCF regime. For example, does the environment have a greater effect on the initiation or early propagation behavior of an initiated crack? These questions are discussed further in this thesis.

CHAPTER 3

MATERIAL AND EXPERIEMENTAL PROCEDURES

This chapter describes the material investigated and the experimental techniques used in this study. Section 3.1 describes the properties of the near alpha titanium alloy employed in this work. Section 3.2 describes the fatigue specimens used in small crack growth experiments and fatigue crack initiation studies, including the design and preparation of the specimens for testing. The techniques and procedures used for ultrasonic fatigue testing are described in Section 3.3, which also includes descriptions of the experimental setups employed for fatigue crack initiation studies, laboratory air fatigue crack growth testing, and the newly developed ultrasonic fatigue and environmental scanning electron microscopy system. Finally, Section 3.4 covers the microstructural characterization techniques that were used.

3.1 Material

Ti-6242S, a polycrystalline, near-alpha titanium alloy was provided in the form of oversized cylindrical blanks with approximate dimensions of 11.7 mm diameter by 46.0 mm long. The material was extracted from a larger disc shaped forging by electrical discharge machining (EDM). The alloy was processed to produce a bimodal microstructure and had a nominal composition of wt.%. 6Al, 2Sn, 4Zr, 2Mo, 0.1Si, and Ti (balance). Table 3.1 shows the material chemical composition measurements obtained from energy dispersive x-ray spectroscopy (EDS) and microprobe analysis conducted by personnel at the Air Force Research Laboratory. The bi-

modal microstructure consisted of primary α grains in a transformed β matrix, as shown in Figure 3.1. The exact thermomechanical processing steps are proprietary, but the processing route used to produce this microstructure can be estimated base on the observed microstructure and is described in Section 2.1.3 [25]. The average primary α grain size measured by the linear intercept method was 12.5 µm ± 5.5 µm. The area fraction of the primary α phase was approximately 30% ± 3%. The measured Young's modulus and yield stress were 121 GPa and 926 MPa, respectively. The Young's modulus was measured using a Jagdish Electronics Dynamic Elastic Properties Analyzer (DEPA) and the yield stress was determined by conventional tensile testing.

Table 3.1: Chemical composition of Ti-6242S alloy used in this study

	Al	**Sn**	**Zr**	**Mo**	**Ti**
EDS Analysis	6.7	2.3	4.9	2.8	Bal.
Electron Probe Analysis (Cameca SX100)	6.2	2.1	4.1	1.5	Bal.

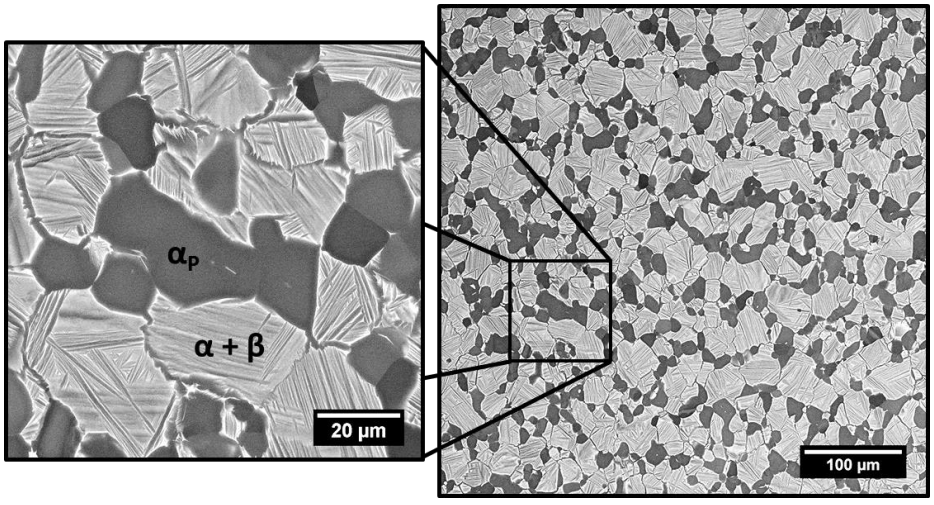

Figure 3.1: Backscattered electron micrograph of Ti-6242S material. The bimodal microstructure consisted of globular primary α grains in a transformed β matrix with an average primary α grain size of 12.5 ± 5.5 µm. The volume fraction of the primary α phase was approximately 30 ± 3%.

3.2 Fatigue Specimens

3.2.1 Specimen Design

Fatigue specimens were designed to resonate at approximately 20 kHz. The fatigue specimen drawing is shown in Appendix A. Specimens were designed using a Matlab program that computes the overall specimen length given the density, Young's modulus, and diameter of the specimen. The code uses numerical techniques to solve a wave equation of the form given by Equation 3.1, where $u = u(x,t)$ is the displacement along the specimen in the longitudinal (x) direction, A is the cross-sectional area, $\dot{A}$ is the derivative of A, ρ is the density, and E is the Young's modulus. Equation 3.1 is solved iteratively for the three regions of the fatigue specimens: the gage section, the curved end of the gage section, and the shoulder region leading to the grips.

$$\ddot{u} + \left(\frac{\dot{A}}{A}\right)\dot{u} + \omega^2\left(\frac{\rho}{E}\right)u = 0 \tag{3.1}$$

As shown in Equation 3.1, the resonant frequency depends on the ratio of the modulus and density of the material. Figure 3.2 shows a characteristic plot of the strain and the displacement along the fatigue specimen. The strain is nearly constant through the specimen gage (10 mm) and decreases through the shoulder and grip regions. The center of the specimen corresponds to a zero-displacement node and the specimen ends are displacement maxima.

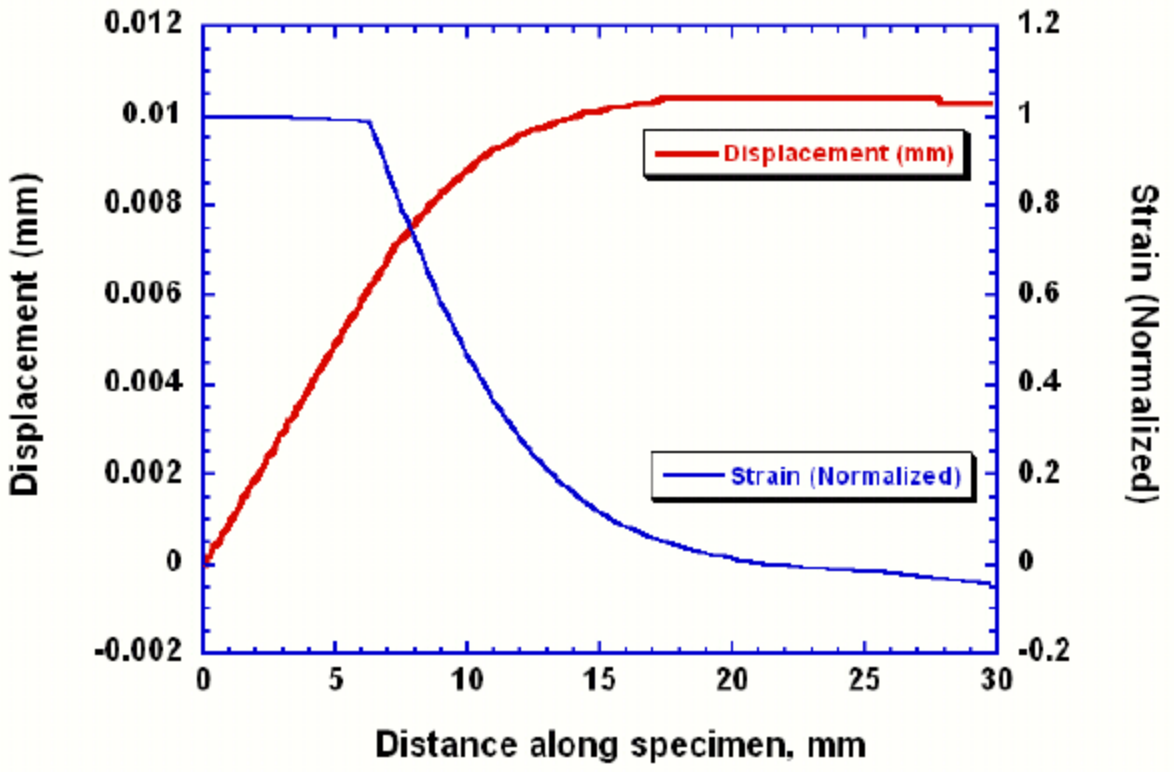

Figure 3.2: Representative plot of the displacement and strain as a function of position along the ultrasonic fatigue specimen axis for Ti-6246. [83]

3.2.2 Specimen Preparation

Smooth bar fatigue specimens were used for both fatigue crack initiation and fatigue crack growth tests. Fatigue test specimens were machined from slices extracted in the circumferential orientation from a disc-shaped forging. The longitudinal axis of the specimen blanks was aligned with the radial directions of the forging. Cylindrical specimen blanks were extracted by EDM and measured approximately 11.7 mm in diameter and 46.0 mm long. This material served as the gage section. Ti-6Al-4V rod was inertia welded to the specimen blanks for shoulder and grip regions. Diametrically opposed surface flats extending from the specimen shoulder regions were machined into the gauge section to facilitate fatigue crack growth observations and microstructural mapping using electron backscatter diffraction (EBSD) techniques. Final machining included low-stress grinding to minimize compressive residual stresses and was completed by Metcut Research Inc. A part drawing of the fatigue specimen is shown in Appendix A. The final specimen was designed to resonate at approximately 20 kHz and had a gage section of nominally 4 mm in diameter and 10 mm in length.

To further minimize surface compressive residual stresses, fatigue specimens were electropolished in a solution of 590 ml methanol, 350 ml butyl cellosolve, and 60 ml perchloric acid at -40 °C for 90 minutes. A schematic of the in-house electropolishing setup is shown in Figure 3.3. A one liter steel beaker was filled with the electrolyte solution and cooled to approximately -40 °C. The cooling bath of ethanol was contained in an Agitainer unit that uses a magnetic stirring pill and insulates the system. Additional insulation was obtained using a custom fiberglass cover. Cooling was accomplished using a Neslab Cryocool CC-100II Immersion Cooler. The steel beaker served as the cathode for the electrolytic cell. The specimens were attached to a motor using a thread copper rod and were rotated at 5-10 rpm. The electrolyte

was cycled using a Cole-Parmer MicroPump at a pumping rate of about 1.5 liters/minute to reduce thermal gradients in the bath and deposit fresh electrolyte at the specimen surface. The power supply was set to control the potential at 20 V, and the current was allowed to fluctuate as a function of electrolyte temperature and surface condition. Specimens were polished for 45 minutes in one vertical orientation before being flipped for an addition 45 minute polishing in the other vertical orientation to further reduce the effects of any thermal gradients. Approximately 100 μm was removed from the specimen surface by electropolishing.

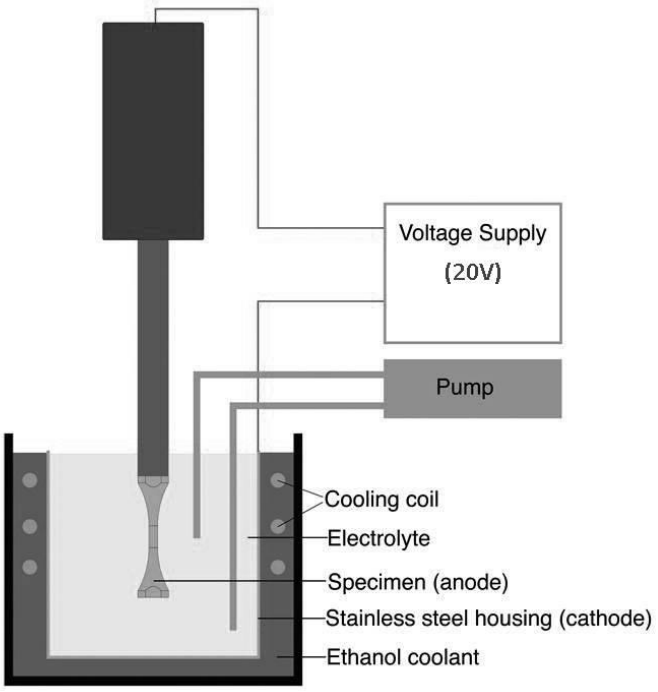

Figure 3.3: A schematic of the in-house electropolishing setup

3.2.3 Fatigue Crack Growth Specimens

In the case of fatigue crack growth testing, smooth bar fatigue specimens were notched at the surface to investigate small crack growth behavior. Micro-notches, which served as the initiation sites for fatigue cracks, were machined in the specimen flats using a FEI Nova Nanolab focused ion beam (FIB) SEM or FEI Quanta 3D E-SEM equipped with a gallium ion source operating at 30 kV and a probe current of 3.0 nA. FIB machining processes induce damage by gallium ion implantation that can alter the local mechanical properties. However, previous studies reported the penetration of 30 kV gallium ions to be much less than 1 μm [128]. Gallium ion implantation is expected to be less than 200 nm at a reduced probe current of 3.0 nA. As many as three 30 μm long (2*c*) and approximately 15 μm deep FIB micro-notches were machined in the center region of the gauge section of each specimen, with a spacing of 1 mm between notches, as shown schematically in Figure 3.4. FIB-deposited Pt markers were placed in a 200 μm by 100 μm rectangle centered about each FIB micro-notch to enable alignment of the EBSD and fatigue test field of view (FOV). Local microstructural information was determined in these neighborhoods by EBSD as shown in Figure 3.5. Fatigue crack growth tests in laboratory air, 133 Pa H_2O vapor, and 65 Pa H_2O vapor were carried out using specimens where FIB micro-notches were placed randomly with regard to the surrounding surface microstructure.

3.2.3.1 Site-Specific FIB Micro-notching

Fatigue crack growth experiments in 1330 Pa H_2O vapor, 665 Pa H_2O vapor, oxygen, hydrogen, and vacuum were conducted using specimens where FIB micro-notches were placed at specific microstructural sites. Placement of the micro-notches (see Fig. 3.5) was determined through a two-step process. First, three 500 μm by 500 μm EBSD maps were created with one at the gage center and the others centered one mm above and below the gage center. Next, a site

having two α_p grains with favorable orientations for crack initiation (see Section 4.4) and spaced approximately 30 μm apart was selected in each large EBSD scan area as the location for the micro-notch, with the notch tips located in these two favorably oriented grains. A second, higher resolution EBSD map centered about the micro-notch location was acquired in order to relate subsequent surface crack growth behavior to local microstructural features. An illustration of a representative FIB micro-notch of this type and accompanying EBSD map of the local microstructure is shown in Figure 3.5.

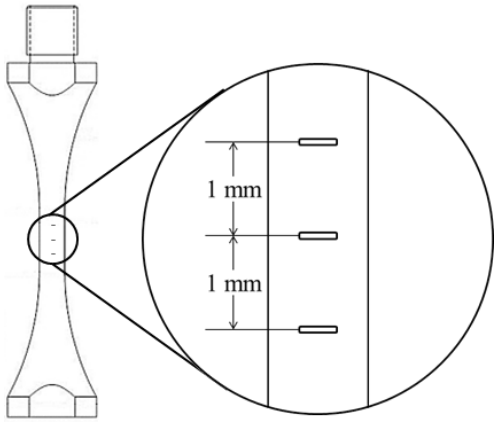

Figure 3.4: A schematic of FIB micro-notch placement on surface of fatigue specimens

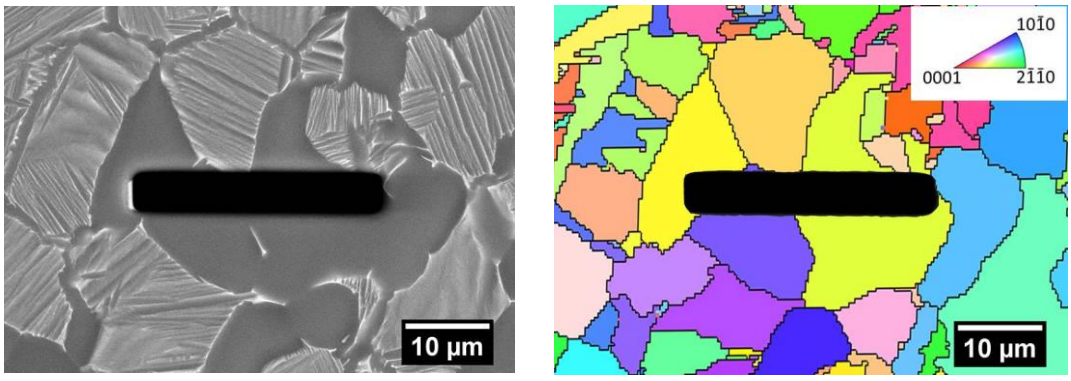

Figure 3.5: A BSE image of a FIB micro-notch is shown with the corresponding inverse pole figure (IPF) map of the surrounding microstructure.

3.3 Ultrasonic Fatigue Testing

Ultrasonic axial fatigue testing was performed in laboratory air, *in situ* in a Philips XL30 ESEM, and *in situ* in a Tescan Mira-3 FEG-SEM using the ultrasonic fatigue testing methods described in Appendix B. Specifically, fatigue tests in this study were conducted using ultrasonic instrumentation designed at BOKU Vienna. All tests were carried out at a stress ratio of R = -1 (fully reversed) and a testing frequency of approximately 20 kHz. For all fatigue crack growth tests a constant displacement amplitude was maintained to produce a stress amplitude of 400 MPa. A block loading cycle of 200 ms pulse and 3000 ms pause was used to minimize specimen heating.

3.3.1 Experimental Setup for Ultrasonic Fatigue Testing in Laboratory Air

Fatigue testing in laboratory air was accomplished using the experimental setup shown in Figure 3.6(a). The key components of this setup are the ultrasonic fatigue system, a Navitar optical imaging system and a Questar positioning stage. A Navitar 12X Ultrazoom lens system equipped with a 20X Mitutoyo infinity corrected objective and a 5-megapixel CCD (Point Grey GRAS-50S5C) was used in combination with the Questar positioning stage to monitor and record images of fatigue crack growth.

The ultrasonic fatigue testing system of this setup is described in detail in [17] and individual components are identified in Figure 3.6(b). A summary of this system follows. The acoustic pulse that drives the fatigue specimen in resonance is generated by the piezoelectric transducer at the top of the load frame. The acoustic signal from the ultrasonic transducer is amplified by the amplification horn before entering the fatigue specimen below. The components of the system are made of commercially available Ti-6Al-4V that are tuned to resonance using the equations described in Appendix B. Fatigue tests are operated in displacement control, within a closed-

feedback loop with a displacement transducer, or Hall Effect sensor. The control unit of the ultrasonic system, shown in Figure 3.7 sends a command voltage to the ultrasonic transducer and monitors the displacement measured by the Hall Effect sensor. The control unit sends power to the ultrasonic transducer until the measured displacement at the Hall Effect sensor matched the user specified amplitude at the control unit. The specimen is in resonance at the specified stress amplitude and the command voltage to the ultrasonic transducer is decreased to a point that is sufficient to maintain resonance to the specimen. The system is able to do this at a specified duty cycle consisting of pulsed loading blocks and pauses to reduce specimen heating. For testing in laboratory air, additional cooling was accomplished using forced air from the lab bench. The specimen temperature was maintained to within 2 °C of room temperature as determined by IR imaging using a FLIR SC5000 IR camera.

Due to small variations in specimen dimensions and the soundness of the connections between load train components, it is necessary to calibrate the system before each fatigue test. Kyowa strain gages with a gage length of 1 mm were applied to each fatigue specimen using strain gage cement. Next, specimens were cycled at low amplitudes, well within the elastic regime. Using the gages and the capability of the ultrasonic control unit to measure the dynamic portion of fatigue cycling at 20 kHz, it is possible to construct a calibration curve of command voltage vs. strain. Since the specimens are tested at approximately 0.4 of the yield stress, it is assumed that the cycling is nominally elastic.

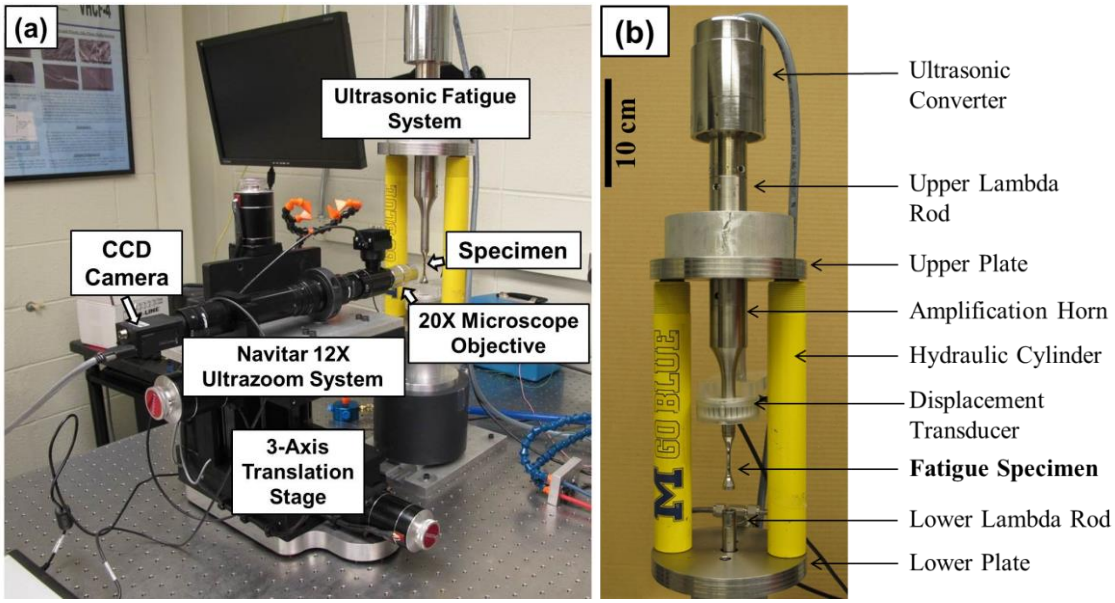

Figure 3.6: (a) Laboratory air setup including Navitar 12X Ultrazoom optical system and ultrasonic testing system and (b) a magnified view of the ultrasonic testing system.

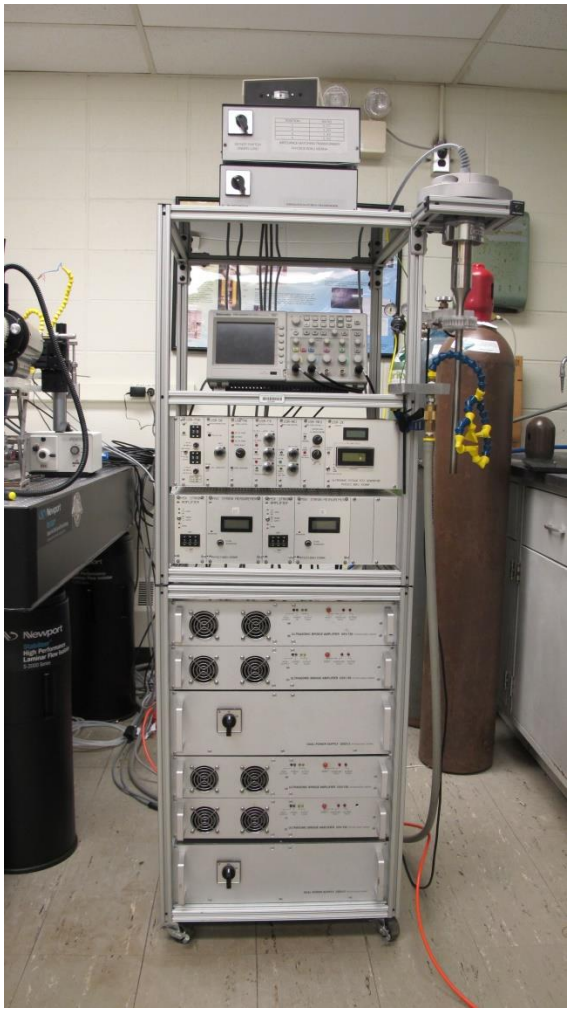

Figure 3.7: Control Unit for ultrasonic fatigue testing

3.3.2 Experimental Setup for Ultrasonic Fatigue Testing in Gaseous Environments

High spatial resolution (≈ 5 nm) imaging of fatigue damage at the microstructural length scale in vacuum and gaseous environments was accomplished using a custom combination of ultrasonic fatigue and scanning electron microscopy, termed UF-SEM and shown in Figure 3.8. The first build of this system combines ultrasonic fatigue testing instrumentation with a Philips XL30 ESEM. The ultrasonic fatigue instrumentation operates using the principles described in [13] and summarized here. The load line of the system is comprised of Ti-6Al-4V components tuned to a 20 kHz resonant frequency using the equations in Appendix B to determine the resonance length. The components include an ultrasonic converter that imparts a controlled sinusoidal displacement using a piezoelectric material stack, an amplification horn that magnifies the displacement from the ultrasonic converter, a lambda rod, and the fatigue test specimen. The system, which is mounted to a custom built SEM chamber door, is controlled by instrumentation that accurately maintains the resonant frequency within ± 1 Hz in displacement control by monitoring the input displacement to the specimen using a piezoelectric transducer in a closed-loop control system. Since putting a Hall Effect sensor inside the SEM complicated the design of the system a new means of measuring the displacement in the load train was devised that uses a piezoelectric film sensor (Measurement Specialties, Inc., Model DT1-028K). The UF-SEM system has been adapted to work on a FEI Quanta 3D E-SEM and a Tescan Mira-3 FEG/SEM. This was done by custom fabrication of SEM chamber doors for each SEM with the other components remaining unchanged. Figure 3.9 shows the UF-SEM system installed on these two SEMs.

Installing the ultrasonic fatigue instrumentation in an ESEM provides the capability to perform fatigue studies under environmental conditions ranging from vacuum (3.7×10^{-4} Pa) to low partial pressures (133 Pa to 2660 Pa) of selected gases. A gaseous secondary electron (GSE) detector was used for electron imaging in low vacuum and gaseous environments. The fatigue specimen is positioned in the desired imaging orientation using a McAllister Technical Services MB1500 manual manipulator stage with five translational adjustments (including insertion). The numerous degrees of freedom in the manual manipulator stage permitted the observation and tracking of multiple cracks or microstructural features such as large grains, grain clusters or regions of microtexture. Furthermore, rotation of the assembly about the longitudinal axis of the specimen enabled *in situ* EBSD mapping for crystallographic characterization.

3.3.2.1 Characterization of Specimen Heating

Specimen heating is a significant concern in the vacuum and low vacuum environments achieved by UF-SEM. No auxiliary cooling methods were used in the in-SEM fatigue experiments. The only procedure used to control specimen heating was a duty cycle. Heating/cooling behavior was determined from both thermal imaging (model FLIR SC5000) and K-type thermocouples. The setup for experiments used to measure the specimen temperature rise from cycling in vacuum using the FLIR camera is shown in Figure 3.10. A side port was created that uses a CaF_2 window, that is IR transparent and enables viewing of the specimen in the SEM once pumped down. In vacuum, specimen temperature was maintained to within approximately 10°C of room temperature for 10^6 cycles applied using a duty cycle of 200 ms / 3000 ms pulse/pause. Only measurements in vacuum were obtained since they are expected to represent the highest and lowest rates of temperature increase and decrease, respectively.

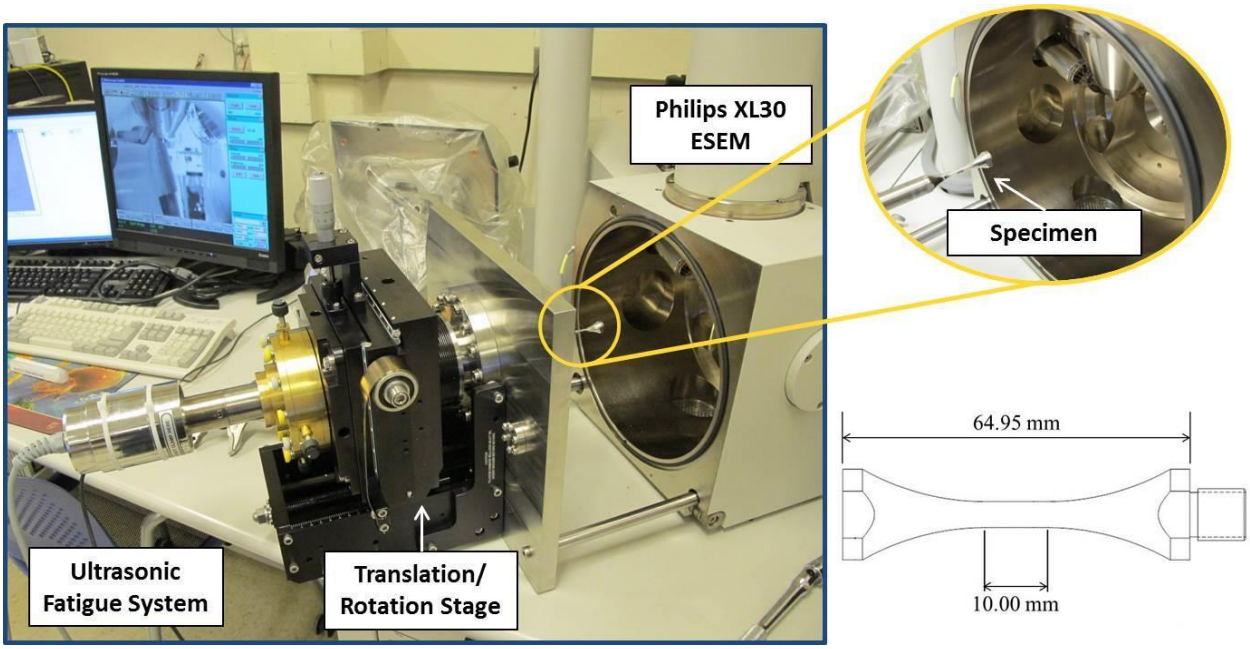

Figure 3.8: Ultrasonic fatigue scanning electron microscope (UF-SEM) system combining ultrasonic fatigue at 20 kHz with the high resolution imaging capabilities of a SEM.

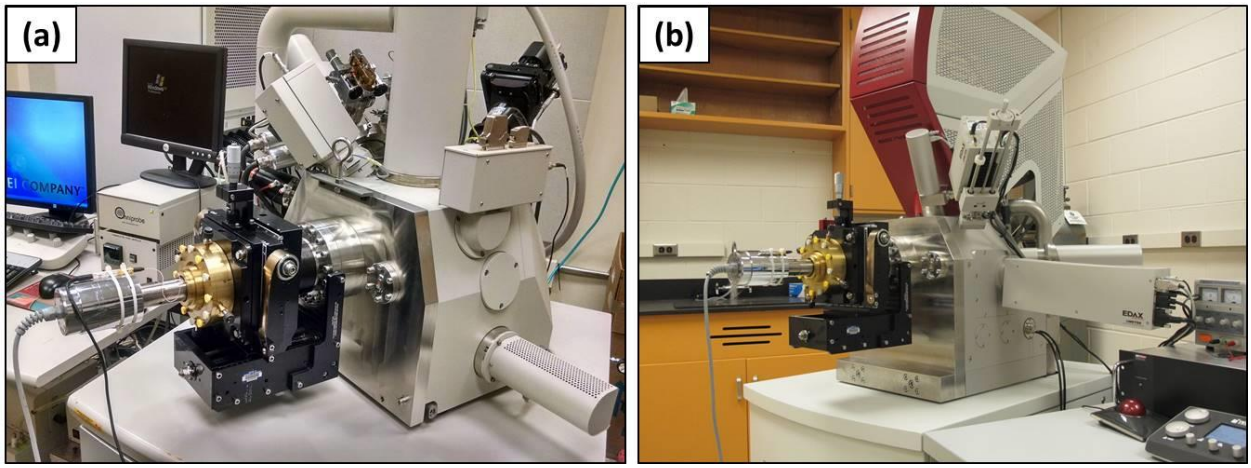

Figure 3.9: (a) UF-SEM system using a FEI Quanta 3D E-SEM (b) UF-SEM system using a Tescan Mira-3 FEG/SEM

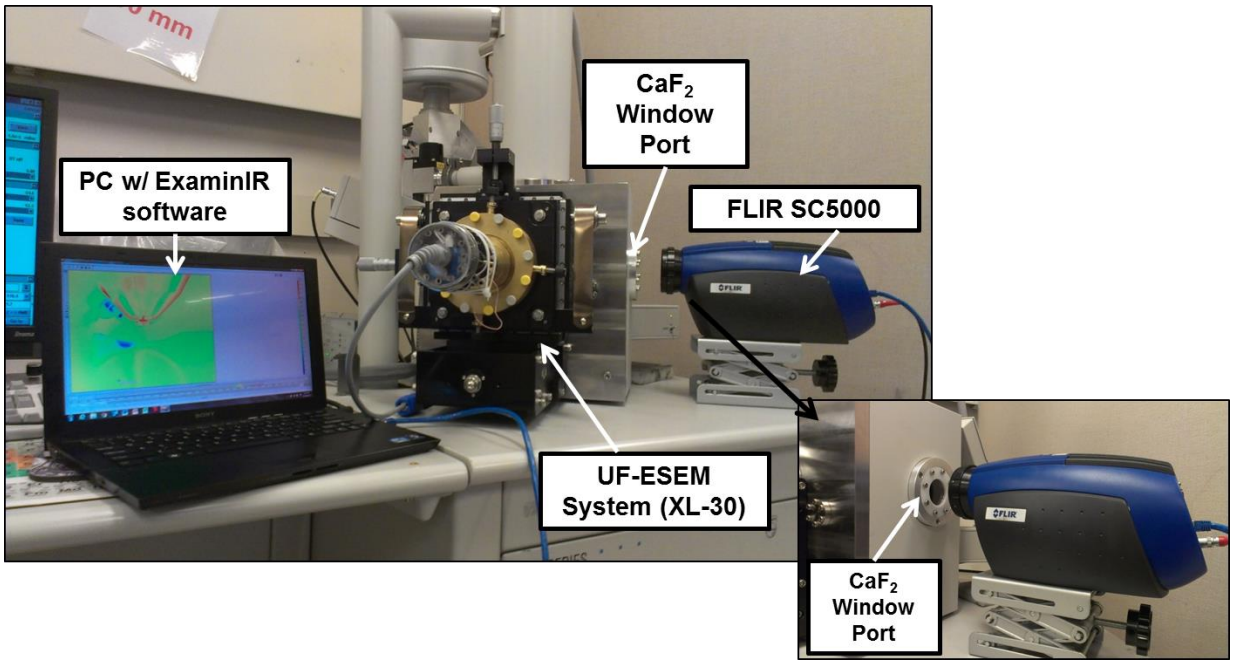

Figure 3.10: Experimental setup for characterization of temperature increase from ultrasonic fatigue cycling in vacuum

3.3.3 Fatigue Crack Growth Tests

3.3.3.1 Environments Studied

The present study investigates the effects of laboratory air, water vapor, oxygen, hydrogen, and vacuum on small fatigue crack growth rates. Table 3.2 lists the environments studied including pressures, the number of fatigue specimens tested in each environment, and the number of surface cracks grown from micro-notches with a surface length ($2c$) greater than 200 μm. Only cracks that were longer than 200 μm were considered in the results discussed in Chapter 4.

Table 3.2: Number of fatigue specimens tested in each environment

Environment	Number of Specimens	Surface Cracks > 200 μm
Laboratory Air	2	4
1330 Pa H_2O Vapor	1	3
1330 Pa O_2	1	1
1330 Pa H_2	1	1
665 Pa H_2O Vapor	1	2
133 Pa H_2O Vapor	3	8
133 Pa O_2	1	3
133 Pa H_2	1	1
65 Pa H_2O Vapor	3	7
1.7×10^{-4} Pa Vacuum	2	1

Relative humidity was not measured for the experiments run in laboratory air, but can typically range from 40-60%, which corresponds to water vapor pressures of nominally 1250 Pa -1900 Pa at 25°C and 101.3 kPa. For laboratory air, it is appropriate to refer to this as a partial pressure of water vapor. However, the term "partial" may not be accurate when describing the water vapor environments obtained by the ESEM as they are expected to be predominantly saturated water vapor. The water vapor environments of the ESEM were achieved by placing the system under vacuum and inserting the water vapor using a cycling procedure that ensures the only gas present in the SEM chamber is water vapor (and trace impurities) at the desired pressure

at the end of the process. A schematic of the Philips XL30 ESEM is shown in Figure 3.11. The water vapor is generated by a flask of water that is heated using a hot plate to keep a steady layer of water vapor above the liquid water. The same cycling process is used to obtain the tested pressures of oxygen and hydrogen.

3.3.3.2 Capturing Images of Fatigue Crack Growth

Surface images of fatigue cracks were captured using two different methods. In laboratory air tests images were taken using the Navitar optical system equipped with a 5-megapixel CCD. For the in-SEM tests, micrographs were captured using secondary electron imaging or using a back-scattered electron (BSE) detector for greater phase contrast. Flats were required to ensure that the images of the surface images of the crack remained in focus. Cycling was paused every 10,000 to 25,000 cycles, depending on the fatigue crack growth rate (FCGR), to observe damage and capture pictures for the subsequent determination of crack growth rates. Images were captured until the sample failed, defined as an inability of the control unit to maintain specimen resonance for a long fatal crack. In this material this occurred for cracks that grew to a depth of approximately 1.75 mm. Higher resolution micrographs of the surface cracks and fracture surfaces, described in Chapter 4, were obtained *ex situ* using a Tescan Mira-3 FEG-SEM.

3.3.3.3 Analysis of Fatigue Crack Growth Tests

Fatigue crack growth data are presented in the typical dc/dN vs. ΔK format. The surface FCGR, dc/dN, was calculated using the secant method and the stress intensity factor range, ΔK, was calculated using the equations of Newmann and Raju [129] for a surface crack in a finite elastic plate. Since the subsurface crack length (a) could not be directly measured, it was assumed that the crack advanced according to $c/a = 1$. Only the positive part of the load cycle at R = -1 was used in the calculation of ΔK, i.e. $\Delta K = K_{max}$.

The fatigue crack growth behavior is assumed to follow a power law equation, where the fatigue crack growth rate, *dc/dN*, is related to the cyclic stress intensity factor, Δ*K*, by the power law equation given by Equation 3.2.

$$\frac{dc}{dN} = C(\Delta K)^m \tag{3.2}$$

In Equation 3.2, *C* and *m* are constants that are influenced by many factors including material microstructure, environment, temperature, and load ratio.

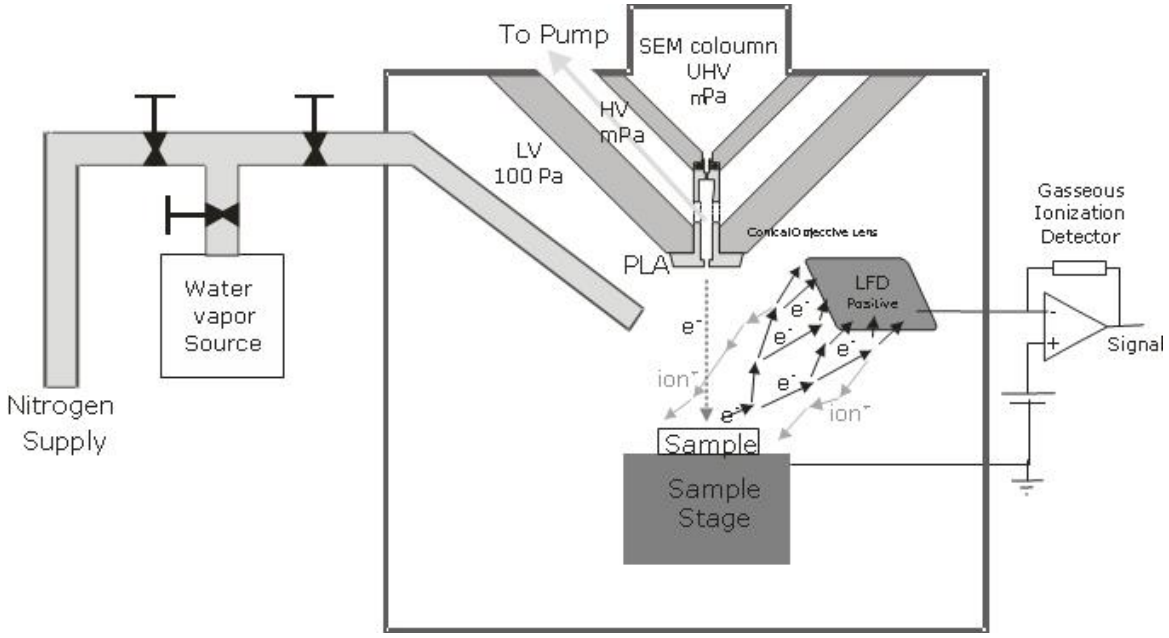

Figure 3.11: Schematic of environmental scanning electron microscope system. The water source is a flask of water heated using a hot plate to keep a steady layer of water vapor above the liquid water in the flask. The nitrogen supply line can be used to input other gases such as oxygen and hydrogen [130]

3.3.4 Fatigue Crack Initiation Tests

Studies to examine natural crack initiation were conducted on fatigue specimens with machined flats but containing no micronotches. Only laboratory air and vacuum studies were conducted. Experiments in laboratory air were carried out using the ultrasonic fatigue system described in Section 3.3.1 and shown in Figure 3.6. Vacuum tests were carried out using the UF-SEM system adapted for the Tescan Mira-3 FEG-SEM shown in Figure 3.9. Again, all tests were carried out at 20 kHz and R = -1, but the stress amplitude varied with test specimen from 225 – 500 MPa.

3.4 Microstructural Characterization

3.4.1 Metallographic Sample Preparation

Metallographic samples were prepared using several of the specimen blanks in order to characterize the microstructure of the Ti-6242S material. The blanks were sectioned in the radial (RD) and circumferential (CD) directions as shown in the schematic in Figure 3.12. The planes of RD represent planes normal to the fatigue specimen loading direction. The sectioned samples were mounted in Bakelite using a Buehler Simplimet 2 compression mounting press. Grinding was completed with successively finer grit silicon carbide papers from 400 to 1200 grit. Polishing was completed using 9 μm and 1 μm diamond suspensions on Buehler microcloth pads. Finally, a final polish was completed using colloidal silica suspension on a Buehler microcloth using a vibratory polisher for 8 – 12 hours. For determination of grain size, specimens were lightly etched using Kroll's reagent (2 – 4 ml hydrofluoric acid, 6 ml nitric acid, and 100 ml distilled water) by submersion for 5 – 10 seconds.

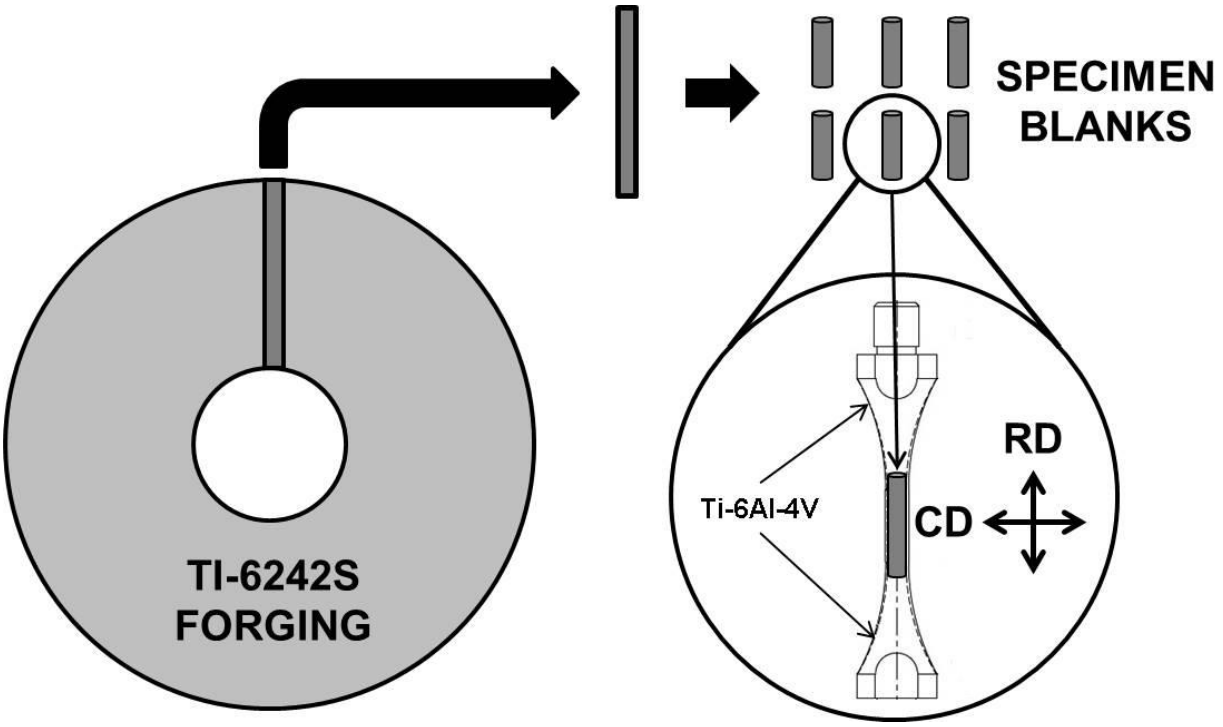

Figure 3.12: A schematic of orientation of blank extraction from the parent forging for making specimens for material characterization and fatigue specimens.

3.4.2 Optical Microscopy

Light optical microscopy was completed using a Nikon inverted optical microscope to examine the microstructure. Digital images were acquired at various magnifications and these were used to determine the average grain size and the volume fraction of the primary alpha (α_p) phase.

3.4.3 Scanning Electron Microscopy

Scanning electron microscopy (SEM) was used to characterize the material microstructure and complete surface and fracture surface investigations of fatigue specimens. Microstructure characterization was done using a Philips XL-30 FEG-SEM. High resolution micrographs shown in Chapter 4 and Chapter 5 were obtained *ex situ* using a Tescan Mira-3 FEG-SEM. Electron backscattered diffraction (EBSD) techniques were performed using both instruments in order to

gain information about crystallographic orientation and morphology. EBSD scans were carried out at 30 kV with scan step sizes 0.25 – 0.75 μm for microstructural characterization and 1 – 2 μm for large area scans used to identify critical sites for FIB micro-notch placement.

3.4.4 Grain Size and Volume Fraction Measurements

The grain size and volume fraction of the α_p phase were measured using mechanical and digital image analysis techniques. The grain size was measured using the linear intercept method described in ASTM E112. The volume fraction of α_p was determined using application of a point count method to threshold, binary images of the two-phase microstructure. A description of the procedure can be found in [83]. The measurements were also independently verified by collaborators at the Air Force Research Laboratory.

CHAPTER 4

INVESTIGATION OF MICROSTRUCTURAL AND ENVIRONMENTAL EFFECTS ON SMALL FATIGUE CRACK GROWTH USING COMBINED ULTRASONIC FATIGUE AND SCANNING ELECTRON MICROSCOPY

Chapter 4 discusses the results of a suite of experiments designed to characterize the small fatigue crack growth behavior of Ti-6242S and the influence of a range of gaseous environments on fatigue crack growth. The role of microstructure on the propagation of small fatigue cracks, particularly with respect to barriers impeding crack growth, was also investigated. Ultrasonic fatigue and scanning election microscopy techniques (UF-SEM) were used to capture crack growth behavior from focused ion beam (FIB) micro-notches. This technique led to new observations and insights into microstructural and environmental influences on small fatigue crack growth behavior in titanium alloys during ultrasonic fatigue. Section 4.1 presents the characterization of the microstructure and Section 4.2 describes the thermal measurements performed *in situ* to verify that large temperature rises did not occur. Section 4.3 presents small fatigue crack growth behavior for the range of environments examined and an analysis of the likely causes for the environmental effect is presented in Section 4.7. Sections 4.4 through 4.6 explore in more depth the crack growth behavior from micro-notches, including crack path morphology and fractographic analysis. Lastly, section 4.8 summarizes the findings.

4.1 Microstructural Characterization

Fatigue experiments were carried out on Ti-6Al-2Sn-4Zr-2Mo-0.1Si (Ti-6242S) specimens extracted from a forged pancake. The microstructure was nominally uniform throughout the forging, and thus specimens used in the characterization of microstructural features were assumed to be representative of the entire forging. The microstructure of the Ti-6242S used in this dissertation work is shown in Figure 4.1. An average primary α grain size of 12.5 ± 5.5 μm was determined by the linear intercept method. A plot of the grain size distribution of the α_p phase measured using orientation imaging microscopy (OIM) is shown in Figure 4.2. The area fraction of the primary α phase was approximately 30 ± 3% as measured using the point count method with the freely available image analysis program, ImageJ.

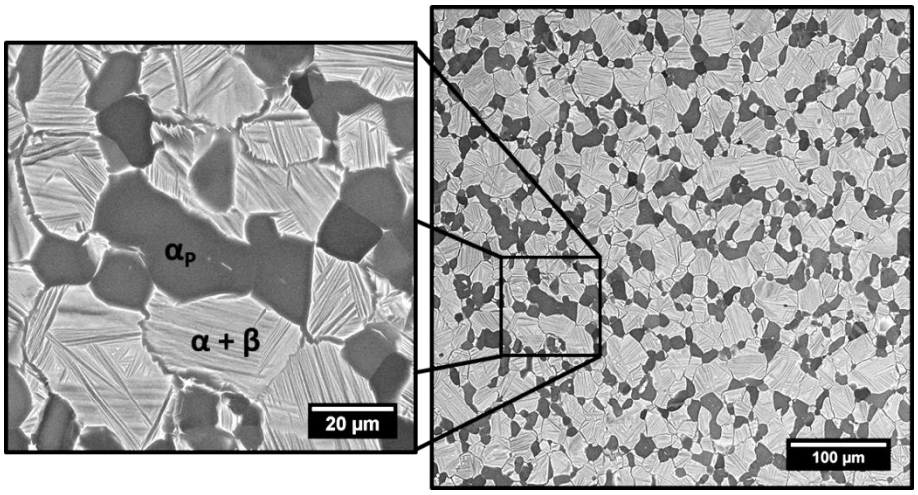

Figure 4.1: Backscattered electron micrograph of Ti-6242S material. The bimodal microstructure consisted of globular primary α grains in a transformed β matrix with an average primary α grain size of 12.5 ± 5.5 μm. The volume fraction of the primary α phase was approximately 30 ± 3%.

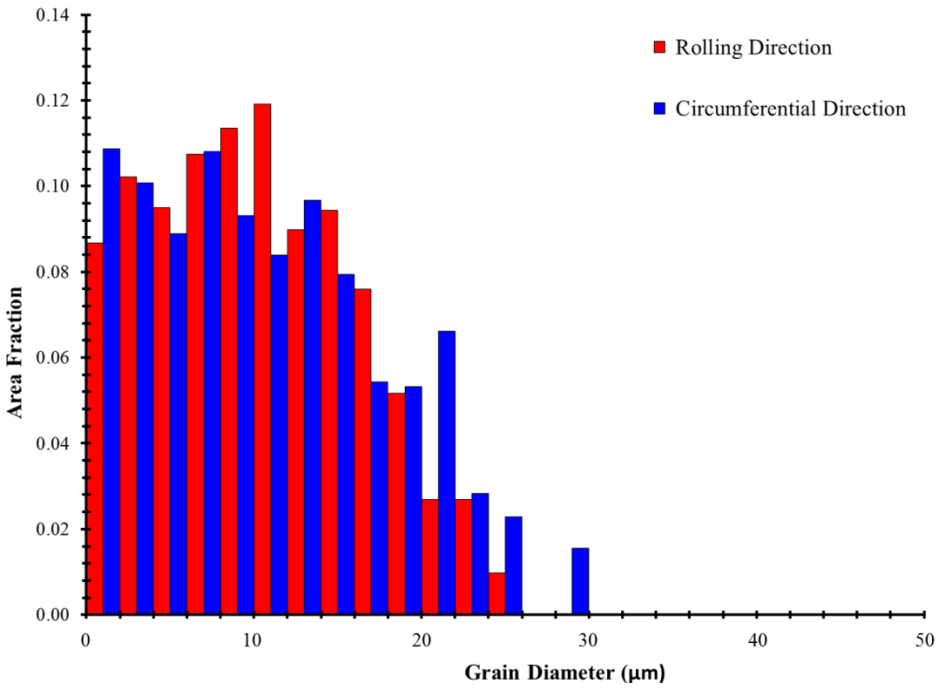

Figure 4.2: Grain size distribution of the α_p phase of Ti-6242S

The Young's modulus (E) and tensile yield strength (σ_y) of the supplied material were 121 GPa and 926 MPa, respectively. The Young's modulus was measured using a Jagdish Electronics Dynamic Elastic Properties Analyzer and the yield strength was determined from monotonic tensile testing.

The degree of microtexture present in the material was characterized through 300 x 500 μm^2 electron backscatter diffraction (EBSD) scans performed in both the circumferential and radial directions. An example of one of these scans and the corresponding pole figure map is shown in Figure 4.3. The material had a low, almost random, texture and no large macrozones or microtextured regions were detected. Microstructure and texture characteristics were verified by similar analyses of larger EBSD scans of approximately 3 x 3 mm^2, conducted on the same material by collaborators at the Air Force Research Laboratory (AFRL) at Wright-Patterson Air Force Base in Dayton, OH. Figure 4.4 shows a representative EBSD scan obtained at AFRL.

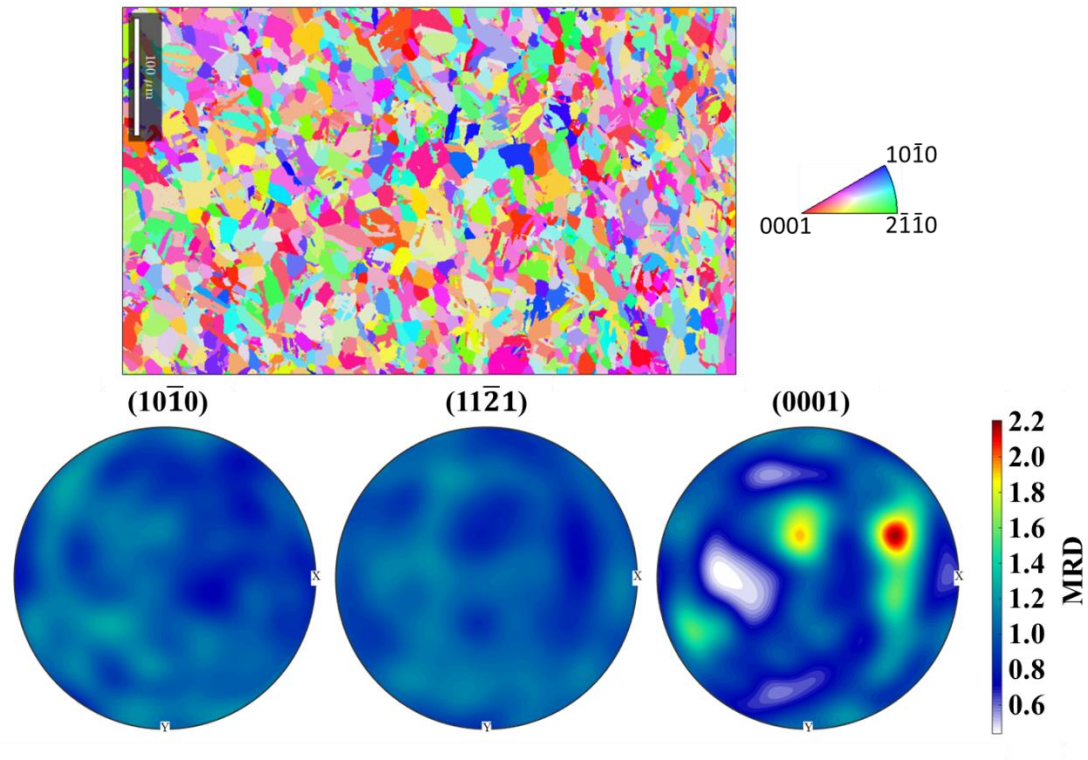

Figure 4.3: Inverse Pole Figure (IPF) map of 300x500 μm^2 area and corresponding pole figure (PF) map indicating low degree of material texture are shown. RD is normal to the image.

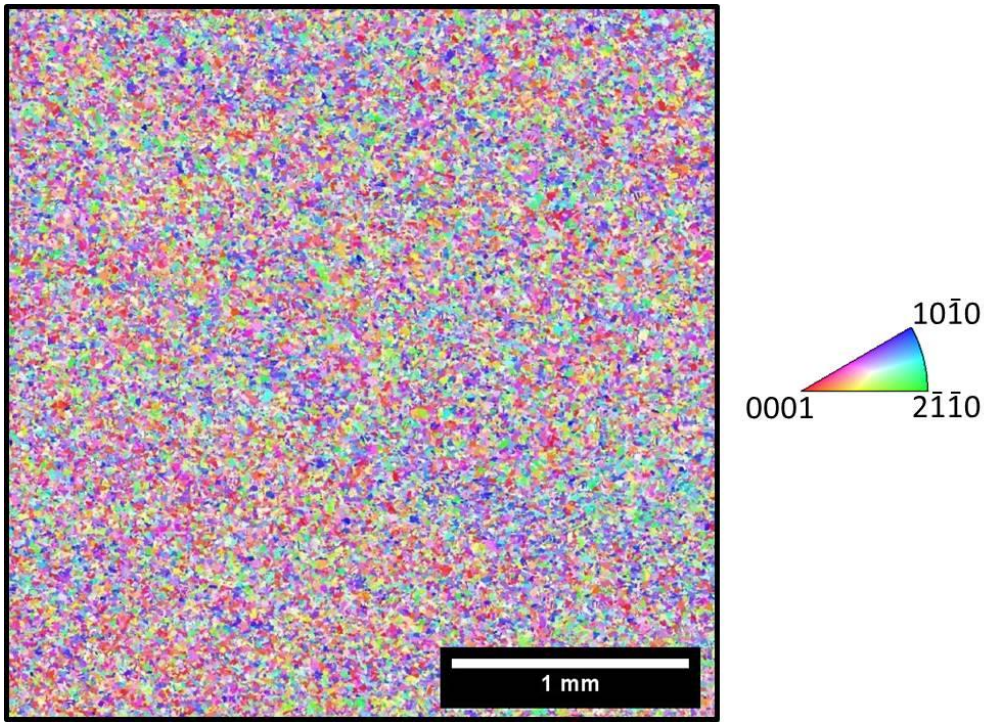

Figure 4.4: IPF of approximately 3 x 3 mm^2 area measured by AFRL collaborators that verifies that material has a low degree of texture

4.2 Macroscopic Thermal Characterization of Ultrasonic Fatigue in Vacuum

Ultrasonic fatigue cycling at 20 kHz in vacuum environments can lead to significant specimen heating, due to an absence of convective heat transfer and the forced air cooling normally available during ambient air testing. The lack of convection means that cooling can only be accomplished by conduction away from the specimen by the other load train components or by radiation. Displacements, and thereby strains, are greatest in the gage section of the specimen, so it is expected that this is where the highest temperatures will occur.

The rise in temperature associated with cycling in vacuum, assumed to be the worst-case scenario of all the environments investigated, was characterized using both thermocouples and infrared imaging. A K-type thermocouple was placed in contact with the gage section surface of a fatigue specimen, which was then cycled from 0 to 10^6 cycles at a duty rate of 200 ms/3000 ms

pulse/pause and allowed to cool in vacuum (σ_a = 400 MPa). Figure 4.5 shows the corresponding cooling rate for this experiment. The rise in temperature at 10^6 cycles was measured as approximately 7 °C, and the specimen took approximately 90 minutes to cool down to ambient temperature in vacuum after cycling was stopped. The temperature rise from vacuum cycling was also characterized using IR imaging analysis. The details of the IR imaging with in-SEM testing setup are described in Section 3.3.2.1. Using the same test procedure, the maximum rise in temperature associated with 10^6 cycles was measured to be 11 °C by IR imaging. Figure 4.6 shows the thermal maps at different numbers of cycles of a fatigue specimen gage section that was cycled in vacuum. The resolution of the thermal maps was 640 x 512 pixels. The temperature of both the lambda rod and the fatigue specimen increased with increasing numbers of cycles, but the highest temperatures occurred in the gage section of the specimen. These measurements were used as a guideline for subsequent fatigue crack initiation and growth studies in UF-SEM to ensure that the specimen temperature did not exceed 40 °C. Such a moderate increase in specimen temperature is not expected to significantly alter fatigue crack initiation and growth behavior in titanium alloys when compared to the room temperature behavior.

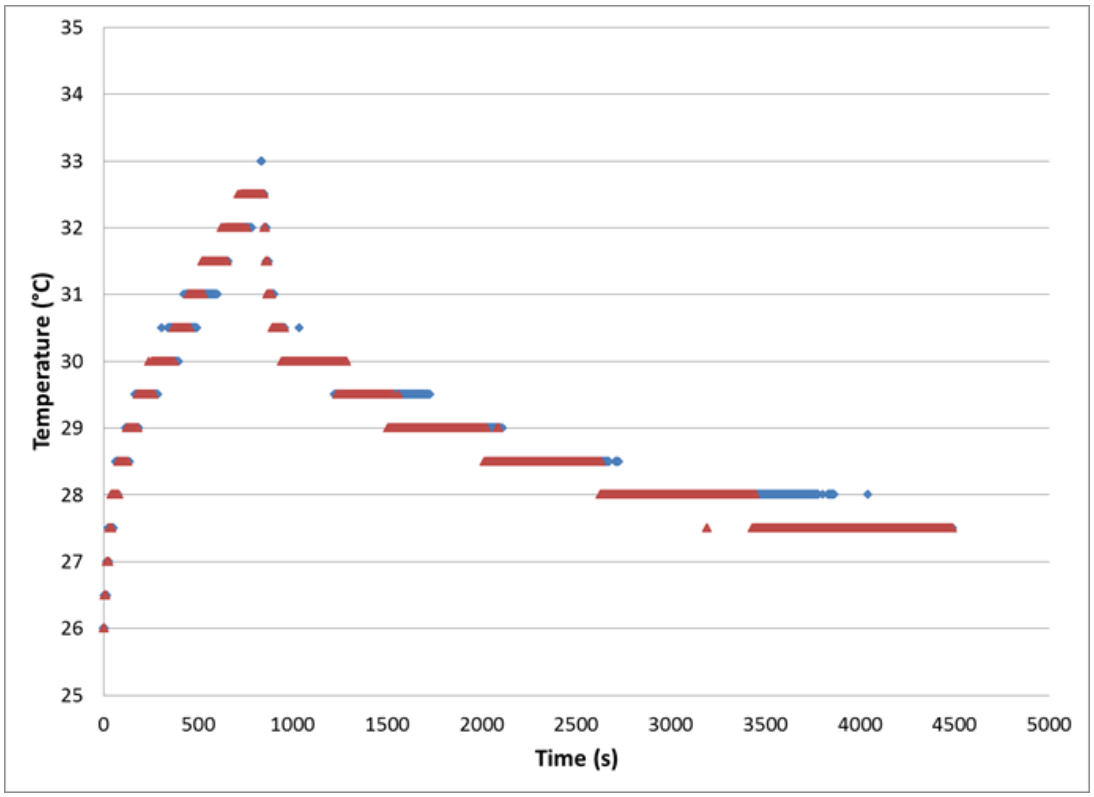

Figure 4.5: Heating curves are shown for a fatigue specimen that was cycled at nominally 20 kHz in vacuum at σ_a = 400 MPa for 10^6 cycles. Red and blue points represent two separate tests under the same conditions. The temperature rise measured using a K-type thermocouple was determined to be approximately 7 °C. The specimen took approximately 90 minutes to cool down to ambient temperature after cycling was stopped.

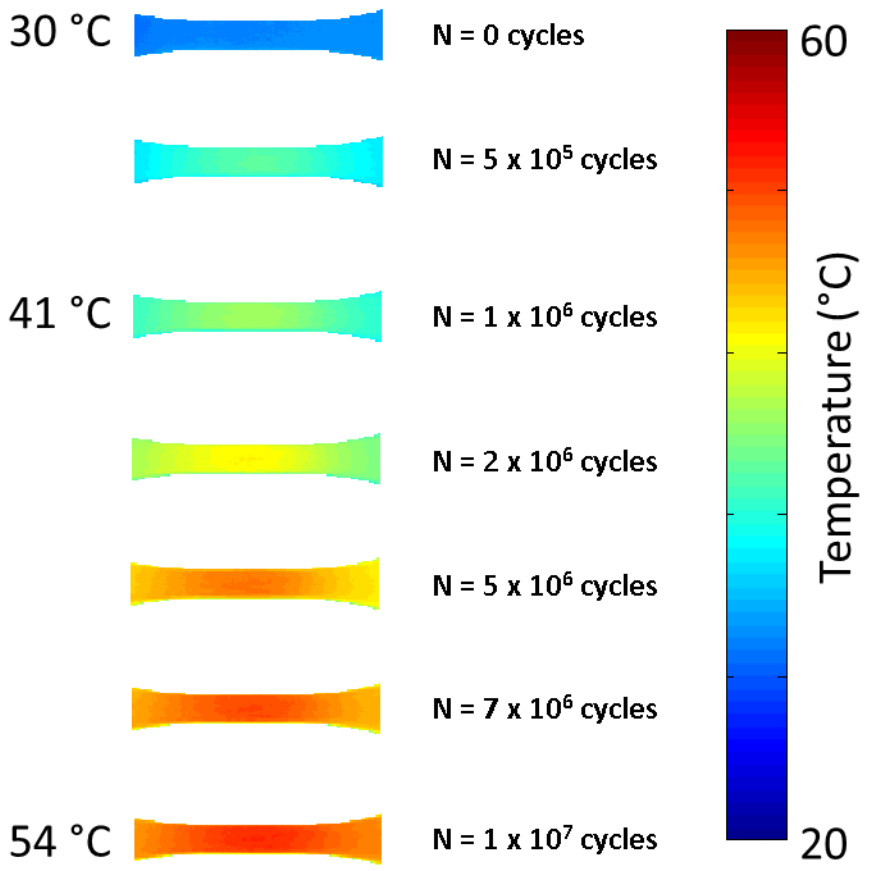

Figure 4.6: Thermal maps of the gage section of a fatigue specimen at different numbers of cycles that was fatigued in vacuum at σ_a = 400 MPa, using a duty cycle of 200 ms/3000 ms pulse/pause are shown. The highest temperatures occurred in the gage section and an increase in temperature of 11 °C was observed after 10^6 cycles.

4.3 Environmental Effects on Small Fatigue Crack Growth Rates

Small fatigue crack growth rates were significantly higher in each environment studied over that in vacuum (1.7 x 10^{-4} Pa) and depended strongly on the specific environment, as shown in Figure 4.7 and Fig. 4.8. The highest fatigue crack growth rates were observed in laboratory air and in the 1330 Pa H_2O vapor environment. A summary of the fatigue crack growth rates at a ΔK of 6.0 MPa-$m^{1/2}$ and Paris law constants for the environments studied is given in Table 4.1. By assuming Paris law behavior [131], the surface fatigue crack growth rate, *dc/dN*, is related to the cyclic stress intensity factor, ΔK:

$$\frac{dc}{dN} = C(\Delta K)^m$$

where C and m are constants, that are influenced by many factors including material microstructure, environment, temperature, and load ratio. The estimated values of C and m are provided in Table 4.1.

It is recognized that small crack growth behavior does not correlate well with the equations developed using the principles of linear elastic fracture mechanics. Indeed, the significant variability in fatigue crack growth rates for the environments studied, which can span several orders of magnitude (see Figure 4.8), is not captured by Paris law fitting. However, application of the Paris law equation provides an adequate representation of the general trend of the fatigue crack growth rate with increasing stress intensity and is an accepted means for comparison of FCGR between the different environments and with other published studies in the fatigue community.

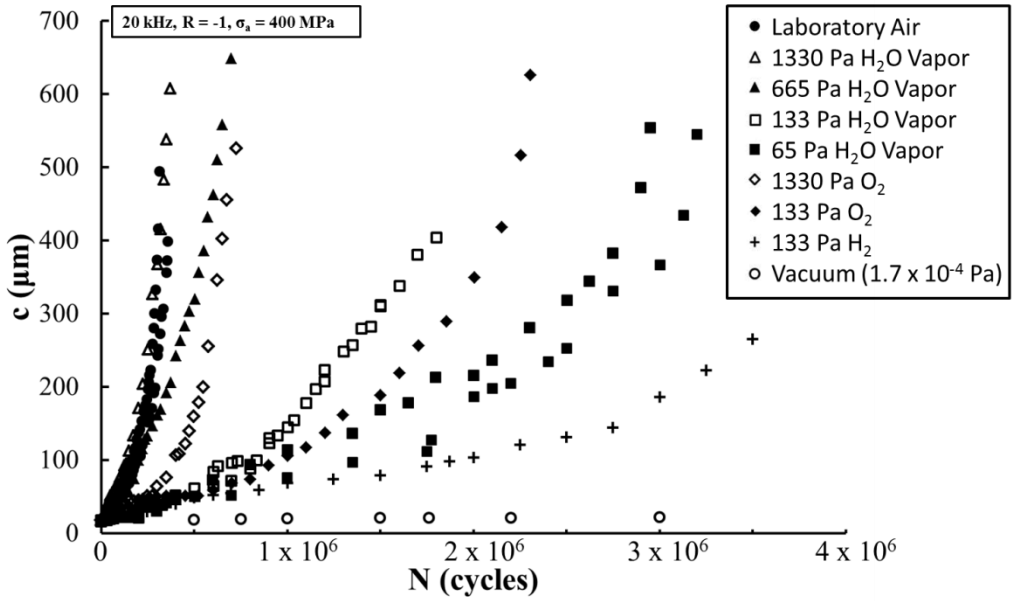

Figure 4.7: Crack length (*c*) vs. cycle number (*N*) for fatigue experiments of the environments studied is shown. Fatigue lifetimes decreased with increasing P_{H2O} and environmentally assisted crack growth was observed in all gases compared to a vacuum pressure of 1.7 x 10^{-4} Pa.

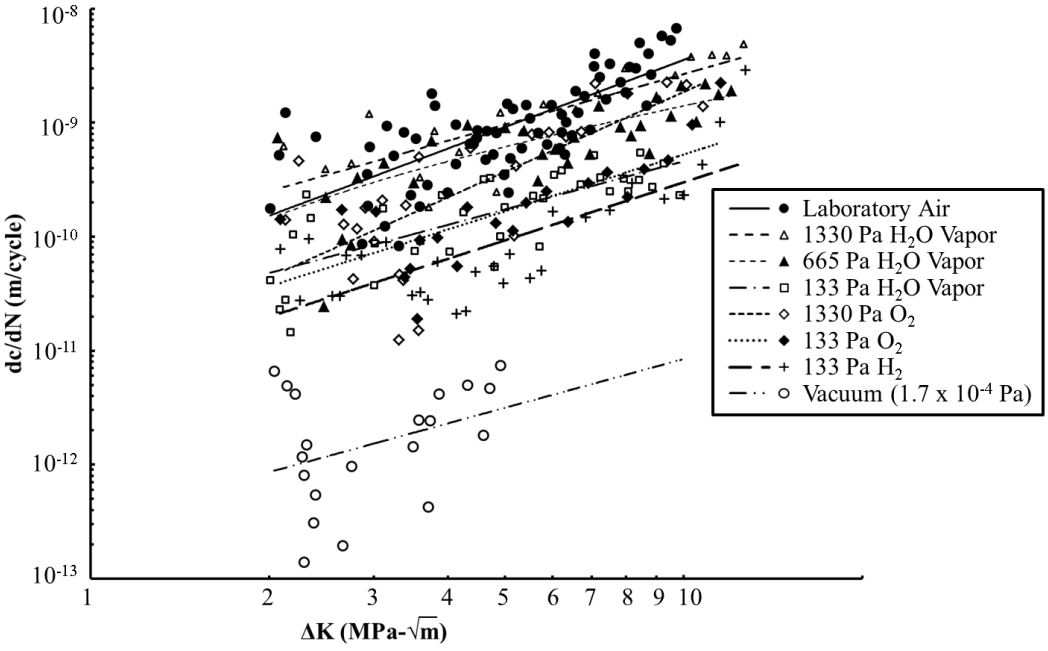

Figure 4.8: The fatigue crack growth rate (*dc/dN*) vs. Δ*K* for all of the environments examined is shown. The highest fatigue crack growth rates were observed in laboratory air and 1330 Pa H_2O vapor. A P_{H2O} of 1330 Pa corresponds to a relative humidity (RH) of ~40% in ambient air at 25 °C and 101 kPa. All tests were conducted using ultrasonic fatigue at 20 kHz and R = -1.

Table 4.1: Summary of fatigue crack growth rate data and Paris law parameters

Environment	$dc/dN_{\Delta K = 6.0}$ **(m/cycle)**	C **(m/cycle)**	m
Laboratory Air	1.32×10^{-9}	3.94×10^{-11}	1.96
1330 H_2O Vapor	1.26×10^{-9}	9.06×10^{-11}	1.47
665 H_2O Vapor	6.55×10^{-10}	5.14×10^{-11}	1.42
133 H_2O Vapor	2.24×10^{-10}	1.82×10^{-11}	1.40
65 H_2O Vapor	1.52×10^{-10}	1.07×10^{-11}	1.48
1330 O_2	5.72×10^{-10}	8.79×10^{-12}	2.33
133 O_2	2.35×10^{-10}	1.16×10^{-11}	1.68
133 H_2	1.27×10^{-10}	6.13×10^{-12}	1.69
Vacuum (1.7×10^{-4} Pa)	4.09×10^{-12}	3.21×10^{-13}	1.42

4.3.1 Fatigue Crack Behavior in Laboratory Air and Vacuum

Small fatigue cracks grew at an approximately three orders of magnitude higher rate in laboratory air than in vacuum, as shown in Figure 4.8. The fatigue crack growth rate in laboratory air was of the order 10^{-9} m/cycle and the fatigue crack growth rate in vacuum was of the order 10^{-12} m/cycle. No measurements of P_{H2O} in vacuum were taken. It is expected that P_{H2O} in a vacuum of approximately 10^{-4} Pa is of the same order of magnitude as the total pressure (~10^{-4} Pa) or lower, based on reported P_{H2O} values from other studies using similar vacuum levels [91].

Small fatigue crack growth rates were lowest in the vacuum environments of the Philips XL-30 ESEM and Tescan Mira3 FEG/SEM setups that had pressures of 3.7×10^{-4} Pa and 1.7×10^{-4} Pa, respectively. In all vacuum experiments where micro-notches were placed randomly with respect to the surrounding microstructure, the crack initiated well after 10^6 cycles and propagated for a small distance before crack arrest. An example of this crack arrest is shown in Figure 4.9.

After cracks had arrested for a minimum of 10^7 cycles, the stress amplitude was increased in 10% increments until crack growth resumed. The results of the vacuum experiment shown in Figure 4.9 are from a test in which an approximately 12 μm long crack was observed at 4 x 10^6 cycles, where σ_{max} = 400 MPa. Further cycling of the specimen to 10^7 cycles resulted in a small increase in crack advance (< 2 μm). Crack debris being expelled from the crack can be seen in Figure 4.9. A discussion of this feature and its possible means of formation are provided in Section 4.6.3. Growing fatigue cracks in vacuum using the same stress amplitudes used for environmental tests proved challenging because of their low growth rate (<10^{-12} m/cycle). Although the high spatial resolution of the SEM (< 5 nm) enables measurement of such low crack growth rates, time and cost restraints dictated that, initial in-ESEM vacuum tests were either step tested to higher stress amplitudes to cause fatigue failure (up to 700 MPa), or water vapor was introduced to accelerate crack growth. In additional studies using micro-notches placed in regions that were more favorable for crack initiation than other regions, cracks were observed to initiate at as little as 5 x 10^5 cycles in-SEM at a vacuum of 1.7 x 10^{-4} Pa. The α_p grains with a high basal Schmid factor favored fatigue crack initiation over grains not having high basal Schmid factors. This topic is covered in further detail in Section 4.4.

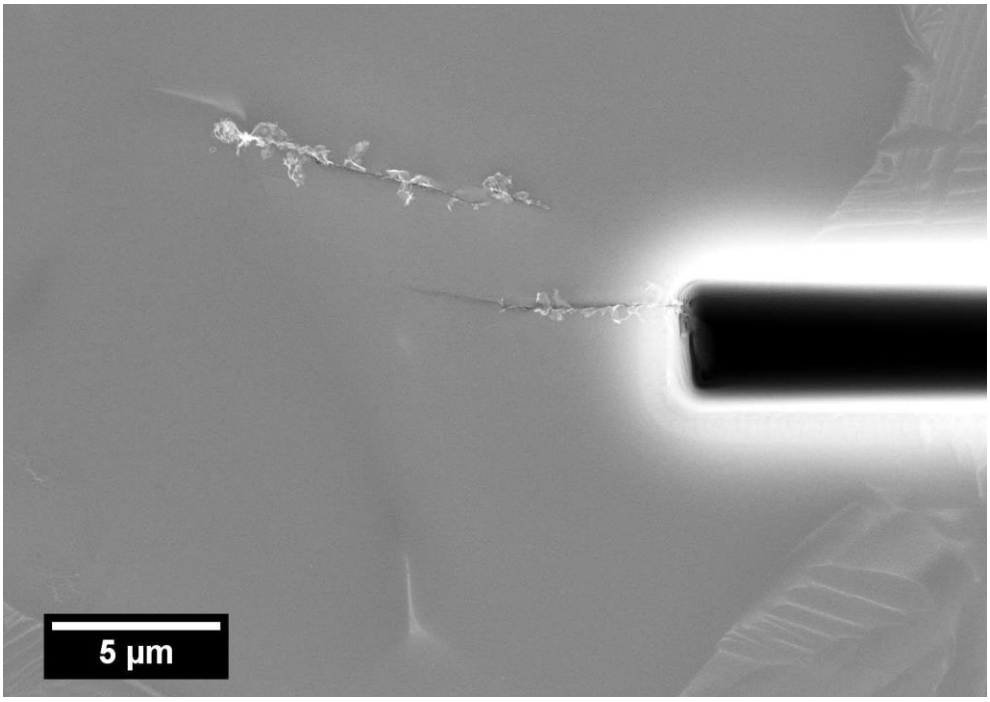

Figure 4.9: Early crack growth from a FIB micro-notch in a fatigue specimen cycled in vacuum is shown. Cracks in vacuum frequently propagated for only a few micrometers, usually within the first grain, before arresting for 10^7 cycles or more. The extruded crack debris is most likely a product of fracture surface oxidation and fully reversed loading.

4.3.2 Fatigue Crack Growth Behavior in Water Vapor, Oxygen, and Hydrogen

The partial pressure of water vapor (P_{H2O}) had a pronounced effect on small fatigue crack growth rates. As shown in Figure 4.10, increases in P_{H2O} led to dramatic increases in growth rates. At a P_{H2O} of 1330 Pa, the highest water vapor pressure tested in these experiments, the FCGR was essentially the same as that observed in laboratory air. While relative humidity was not measured for the experiments run in laboratory air, it typically ranges from 40-60%, which corresponds to water vapor pressures of nominally 1250 Pa -1900 Pa.

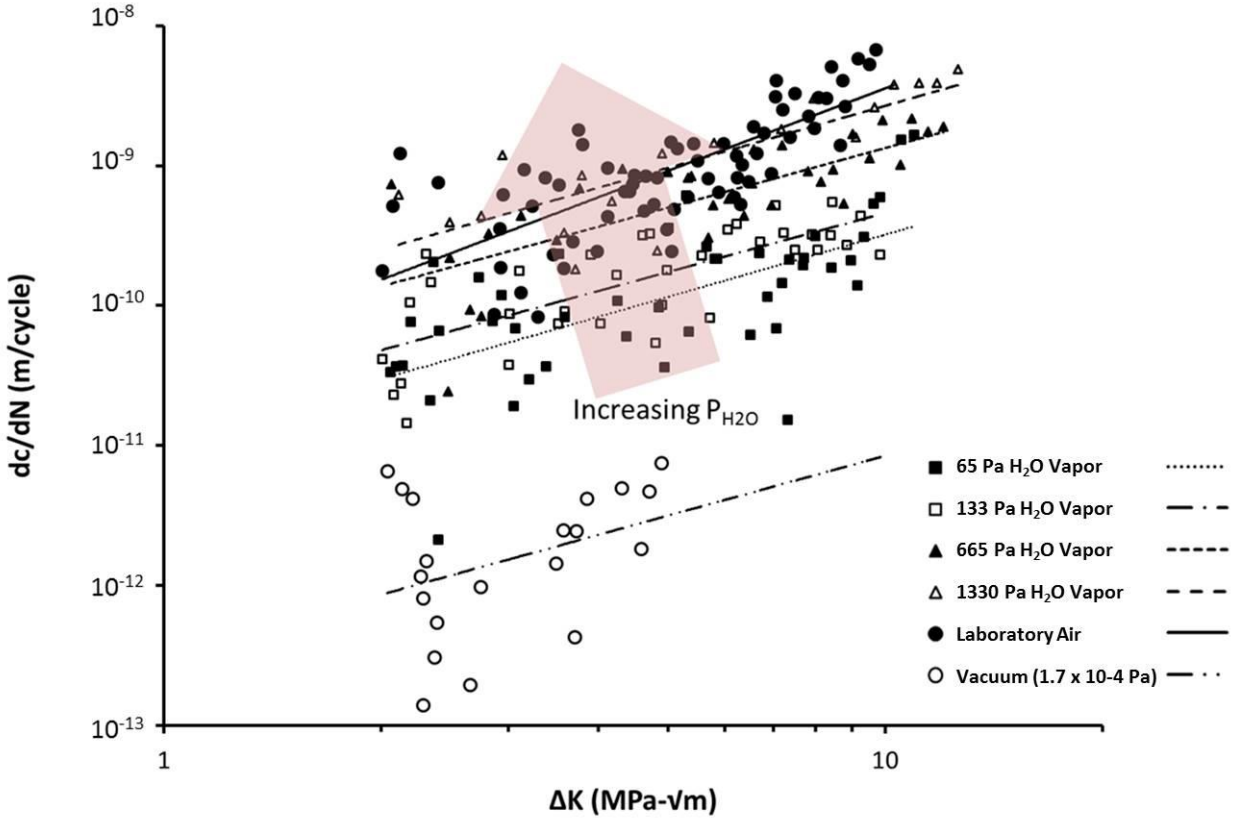

Figure 4.10: The fatigue crack growth rate (*dc/dN*) vs. Δ*K* for each H_2O vapor environment showing that fatigue crack growth rates increased with increasing water vapor pressure, with the lowest fatigue crack growth rates being observed in a vacuum of 1.7 x 10^{-4} Pa.

Figure 4.8 also shows an increase in small fatigue crack rates in gaseous O_2 over vacuum. The FCGR in O_2 gas at ΔK = 6.0 MPa-$m^{1/2}$ was 2.35 x 10^{-10} m/cycle and 5.72 x 10^{-10} m/cycle at pressures of 133 Pa and 1330 Pa, respectively. This represents a two orders of magnitude increase over the growth rate measured in vacuum (4.09 x 10^{-12} m/cycle). Interestingly, the FCGR of O_2 at 1330 Pa was about two times slower than that of laboratory air, where the P_{O2} is approximately 21,000 Pa, or about 15 times greater. The amounts of nitrogen and moisture present in the ultrahigh purity oxygen gas (99.993%) were not measured, but according to supplier specifications (PurityPlus Specialty Gases), nitrogen and water were less than 10 ppm and 3 ppm, respectively.

Fatigue crack growth tests in H_2O and O_2 gas at equivalent pressures of 1330 Pa and 133 Pa showed higher FCGRs in water vapor than in oxygen, with the FCGRs between H_2O and O_2 differing by a factor of 1-2 at both pressures. The fatigue crack growth rates for 1330 Pa and 133 Pa water vapor and oxygen are shown in Figure 4.11. Additionally, the FCGR for the crack grown in 665 Pa H_2O vapor was also higher than the FCGR for the crack grown in 1330 Pa O_2.

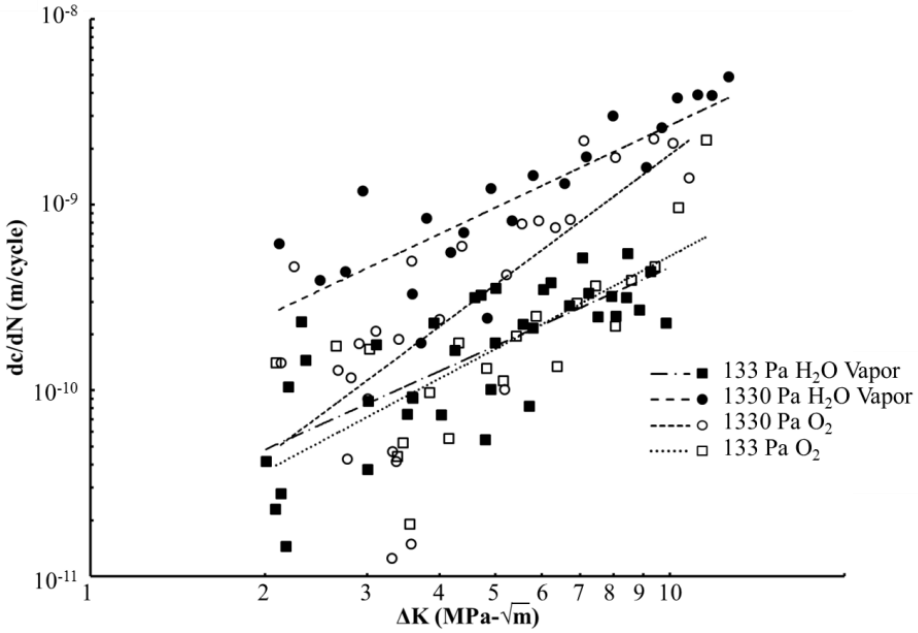

Figure 4.11: The fatigue crack growth rate (*dc/dN*) vs. Δ*K* for water vapor and oxygen at 133 Pa and 1330 Pa. At equivalent pressures, fatigue crack growth rates were higher in water vapor than oxygen. The difference in fatigue crack growth rates was also greater at 1330 Pa than 133 Pa.

A considerable increase in FCGR compared to vacuum was observed for a pressure of 133 Pa in gaseous H_2. The FCGR at ΔK = 6.0 MPa-$m^{1/2}$ in H_2 at 133 Pa was 1.27 x 10^{-10} m/cycle versus 4.09 x 10^{-12} m/cycle in vacuum. A comparison of crack growth rates in 133 Pa H_2, 133 Pa H_2O vapor, and 1330 Pa H_2O vapor is shown in Figure 4.12. Cracks grew slower in H_2 than H_2O at 133 Pa. The FCGR was also slower in H_2 than O_2 at 133 Pa. Research grade hydrogen (99.9999%) was used and the supplier specified impurity levels of oxygen, water, and nitrogen were 0.2 ppm, 0.5 ppm, and 0.3 ppm, respectively.

No fatigue crack growth rate data is available for the specimen tested in 1330 Pa H_2 because the specimen failed by natural crack initiation away from the micro-notches. Interestingly, cracks grew from all three micro-notches, but all three cracks arrested at the surface as shown in Figure 4.13. OIM analysis at the crack-tips of the arresting cracks showed the cracks arrested within grains having a basal or prismatic Schmid factor below 0.20. This is not expected to be a favorable orientation for crack growth, as will be discussed in Section 4.4. This observation also does not eliminate the possibility of subsurface crack growth. In the specimen at 1330 Pa H_2 a crack initiated at a remote distance from the micro-notch and had a fatigue life approximately three times shorter than the crack initiated and grown from a micro-notch in 133 Pa H_2. The failure lifetime was 1.42 x 10^6 cycles at 1330 Pa H_2 (naturally initiated crack) and 4.54 x 10^6 cycles at 133 Pa H_2 (crack initiation from a micro-notch). The site of natural crack initiation and the surrounding microstructure into which the crack propagated were markedly more favorable for fatigue crack growth than the micro-notch regions.

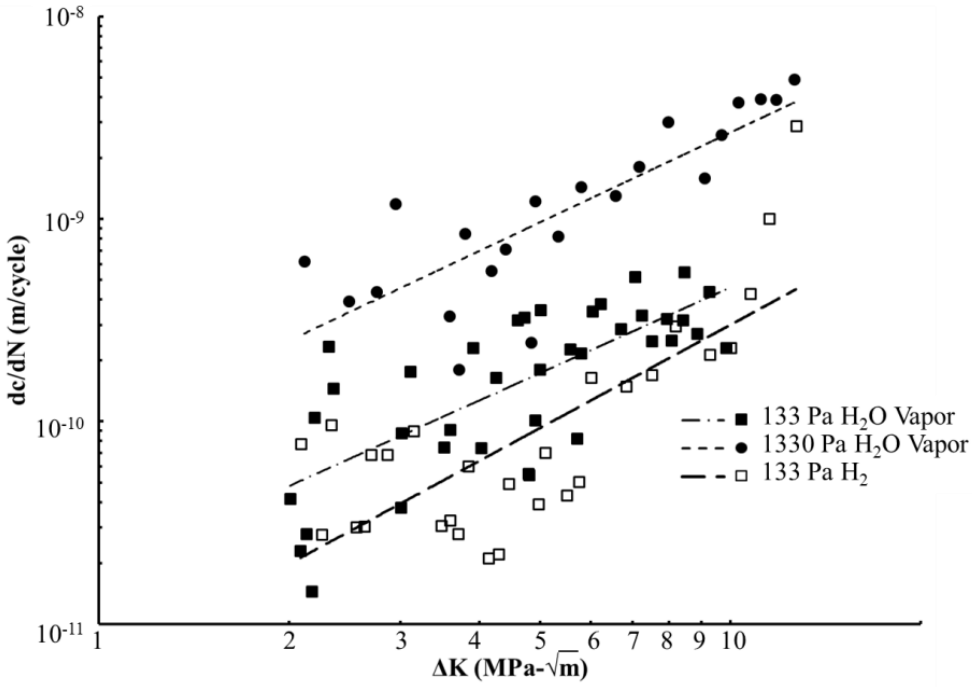

Figure 4.12: Fatigue crack growth rates in 133 Pa H_2 were lower than in 133 Pa H_2O. The growth rate for 1330 Pa H_2O vapor is also shown.

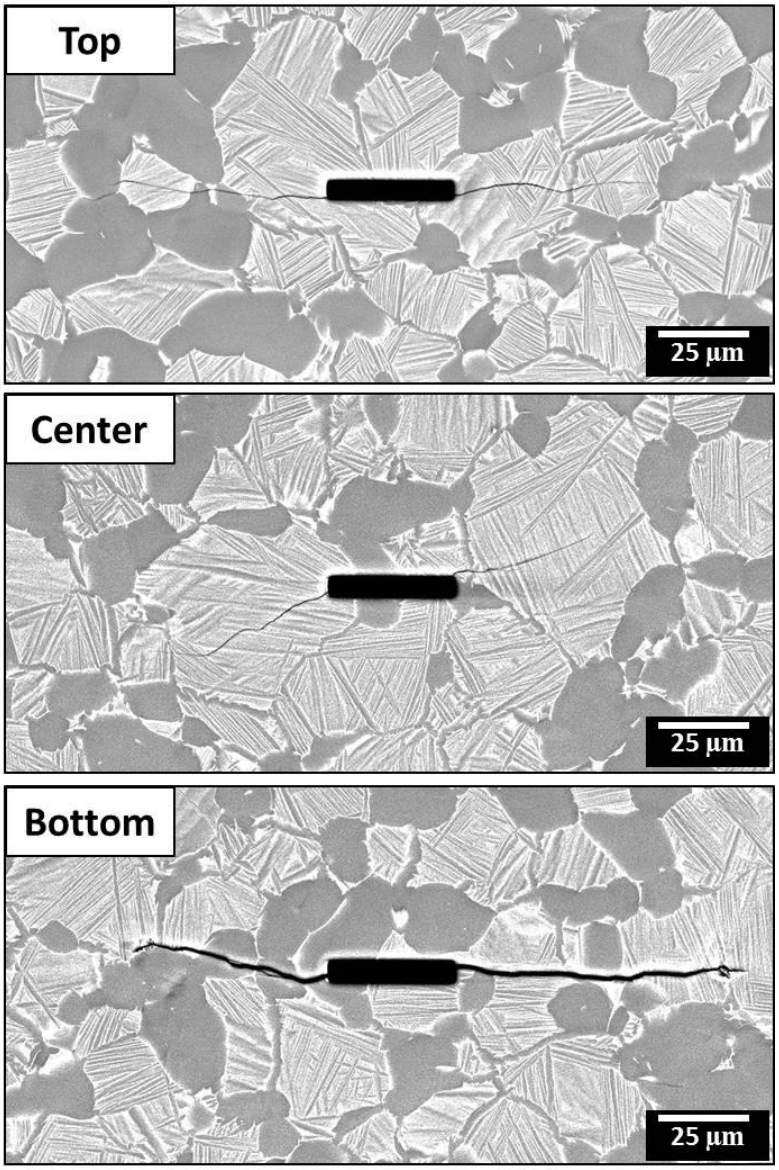

Figure 4.13: Fatigue cracks grown in 1330 Pa H_2 environment. All cracks arrested at similar surface lengths of approximately 150 µm. The fatal crack was naturally initiated in a more favorable microstructural neighborhood for fatigue crack growth.

4.4 Crack Initiation from FIB Micro-notches

This section reports the results regarding crack initiation from micro-notches. The behavior described in this section is based on surface observations in the neighborhood of the notch. It is possible that cracks initiated independently at the root of the notch, but this was not investigated in the present study.

4.4.1 Environmental Effects

Environment significantly influenced fatigue crack initiation lifetime, N_i, from FIB micro-notches, with the shortest initiation lifetimes occurring in laboratory air and the longest in vacuum. Here, crack initiation was defined as the formation of a discontinuity that extended from the micro-notch to a minimum length of 50 nm. As shown in Table 4.2, N_i ranged from 7 x 10^3 cycles to 3 x 10^4 cycles for laboratory air fatigue tests, while no cracks initiated prior to 10^6 cycles in high vacuum tests at the same stress amplitude (400 MPa) for randomly placed micro-notches. N_i for cracks grown in low vacuum P_{H2O} experiments fell between these values, with a range of 2.6 x 10^4 to 3 x 10^5 cycles to initiate an observable crack. In vacuum tests where micro-notches were placed in favorable grains for crack initiation, N_i was as short as 5 x 10^5 cycles in vacuum.

Table 4.2: Fatigue crack initiation lifetime[a] ranges from randomly located FIB micro-notches for each test environment.

Environment	Cycles to observed crack initiation
Laboratory air	7,000 – 30,000
133 Pa H_2O vapor	26,000 – 300,000
65 Pa H_2O vapor	40,000 – 105,000
1.7 x 10^{-4} (vacuum)	>10^6

[a] Crack initiation was defined as the formation of a crack at least 50 nm long on the surface.

4.4.2 Microstructural Effects

Crack initiation behavior was also influenced by the microstructural neighborhoods at the micro-notch tips. Although the number of tests is limited, it is apparent that the ease of basal slip in the local microstructure was critical to fatigue crack initiation. Specifically, when the notch tips ended in primary α grains favorably oriented for basal slip, early crack initiation was observed. Cracks tended to initiate later or decelerate in grains that were not favorably oriented for basal slip. In general, cracks initiated earlier in α_p grains, than transformed β grains.

In several cases and independent of the environments studied, crack initiation did not occur in one or more micro-notch tip neighborhoods before the specimen failed from another micro-notch. The common characteristic of the "non-initiating" micro-notch tips was their location in primary α grains with orientations such that basal planes were nearly perpendicular to the nominal crack growth direction, and which therefore exhibited low basal Schmid factors for the prescribed specimen loading direction. Figure 4.14 shows a FIB micro-notch end located in this type of grain with an IPF map indicating the orientation of the crystal lattice overlaid. Table 4.3 summarizes the microstructural characteristics of grains located at micro-notch ends in fatigued specimens in laboratory air, 65 Pa H_2O vapor, and 133 Pa H_20 vapor environments, for which a surface fatigue crack did not initiate before fatigue fracture occurred from another micro-notch on the sample at 3.9 x 10^5 cycles, 2.9 x 10^6 cycles, and 3.5 x 10^6 cycles, respectively. The basal Schmid factors ranged from 0.14 to 0.20, and the inclination of the basal plane trace with respect to the loading axis (φ) was 13° to 17°. These grains also had high prismatic Schmid factors (0.47-0.49), yet crack initiation did not occur on these planes.

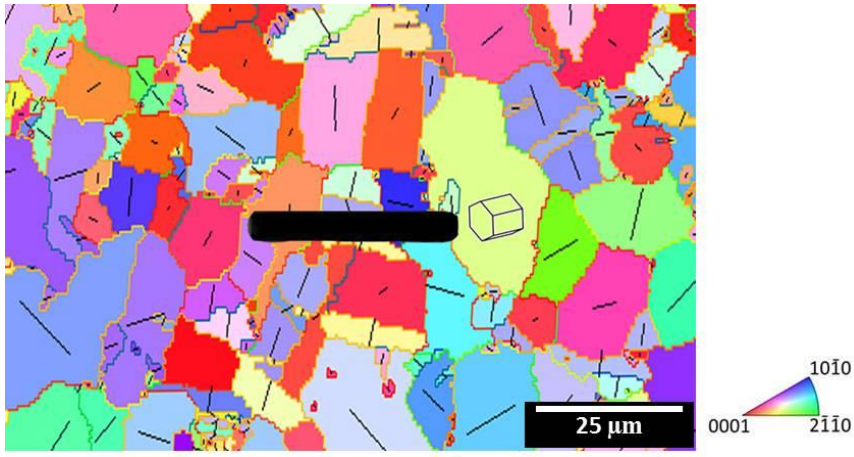

Figure 4.14: An OIM map of the local microstructure of a FIB micro-notch where a crack did not initiate from the right side after 3 x 10^6 cycles in 65 Pa H_2O. A diagram of the orientation of the hcp crystal lattice of the unfavorable α_p grain is also shown. Loading direction is vertical.

Table 4.3: Microstructural characteristics of grains located at micro-notch ends where no cracks initiated.

Environment	Basal Schmid factor	Prismatic Schmid factor	φ (°)
Laboratory air	0.15	0.47	17
133 Pa H_2O vapor	0.14	0.49	13
65 Pa H_2O vapor	0.20	0.48	15

The effect of basal plane orientation on fatigue crack initiation has been studied previously, but those studies mainly focused on the role of microstructure on small crack growth rather than environmental effects. Bache et al. [34] examined short crack growth behavior in a near α titanium alloy and also concluded that the orientation of the basal plane in which a fatigue crack initiates plays a significant role in determining fatigue life scatter. Szczepanski et al. [74] observed a moderate effect of the microstructure adjacent to micro-notches on fatigue crack initiation lifetimes at 20 kHz in a microtextured $\alpha + \beta$ titanium alloy. Specifically, neighborhoods that were favorably oriented for basal and prismatic slip tended to promote early fatigue crack initiation. The present study demonstrates that both environment and neighborhood play a significant role in small crack initiation behavior from micro-notches in titanium alloys even at the high frequencies associated with ultrasonic fatigue.

4.5 Surface Crack Path Observations

4.5.1 Characterization of Fatigue Crack Growth in Relation to Microstructure

Cracks propagated transgranularly along specific crystallographic planes in the small crack region and up to crack lengths of approximately 1 mm. In primary α grains, cracks tended to propagate along basal planes in the early stages of growth. An example of this is shown in Figure 4.15 for an in-ESEM test in a 133 Pa saturated water vapor environment. Here, an overlay of the grain orientation maps from EBSD with crack paths is provided to demonstrate that cracks propagated along basal planes in primary α grains. Another example of early propagation along

basal planes is shown in Figure 4.18 for a test in laboratory air, where the crack propagated along basal planes in two primary α grains before arresting at a high angle α/α grain boundary.

In environments that contained water vapor and oxygen, a significant preference for crack propagation along basal planes was observed in α_p grains, while propagation along basal and prismatic planes occurred at similar frequencies in transformed β grains, as shown in Figure 4.16. Here, a more detailed analysis of the surface crack path orientation with respect to the measured slip plane traces for basal, prismatic, and pyramidal (a-type) slip planes of the relevant grain is shown. In grains where the surface crack path orientation aligned with more than one slip plane trace, it was denoted as <a> type. If no match was observed, the correlation was marked as unknown. Figure 4.16 shows that propagation along basal plane traces was predominately observed in α_p grains. In the transformed β grains, no preference for crack propagation along basal, prism, or pyramidal planes was observed. Additionally, in low pressure environments and in vacuum, the number of unknown crack path orientations with respect to crystallographic planes increased, especially in transformed β grains.

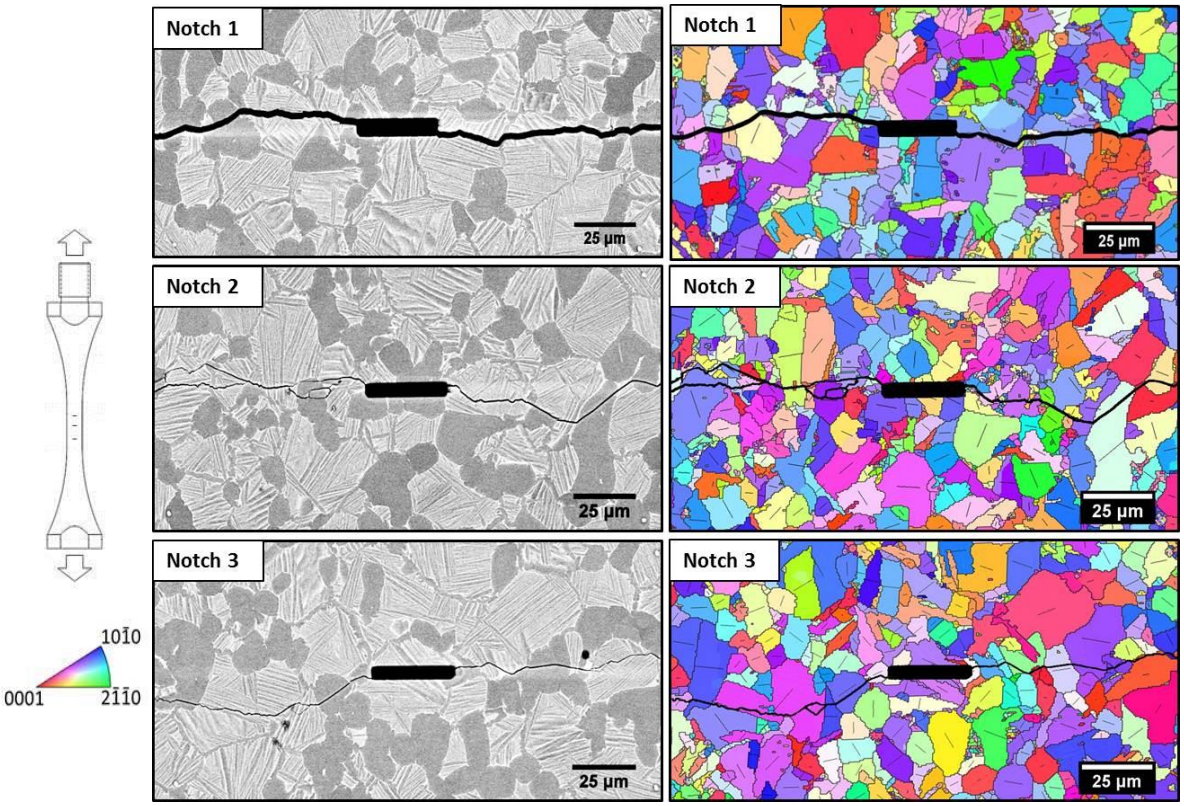

Figure 4.15: Small fatigue cracks propagated in a 133 Pa H_2O vapor environment from three FIB micro-notches machined into the same test specimen. The specimen failed at a fatal crack that was initiated and grown from Notch 1. Transgranular, crystallographic crack growth was observed in each case.

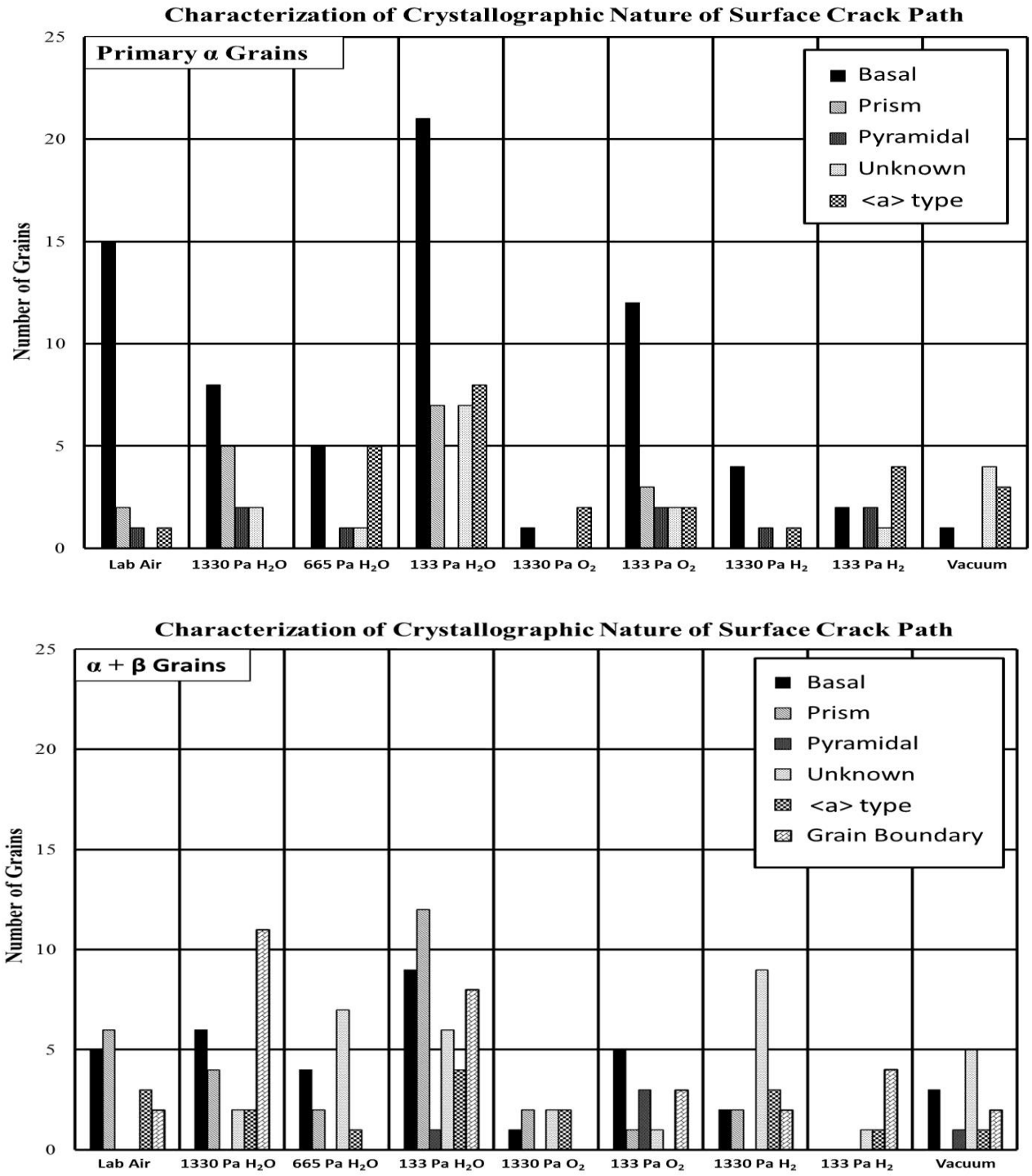

Figure 4.16: A graph of the tendency for the surface crack path to align with slip plane traces of basal, prismatic, and pyramidal planes is shown. In grains where the surface crack path orientation aligned with more than one slip plane trace, it was denoted as <a> type. If no match was observed, the correlation was marked as unknown. A significant preference for cracking along basal planes was observed in α_p grains, while cracking along basal and prismatic planes occurred at similar frequencies in transformed β grains.

Cracks propagating in vacuum had transgranular crack paths that were more perpendicular to the loading axis of the specimen than cracks propagating in air. While some crystallographic crack growth was seen in vacuum as evident by Figure 4.16, the surface crack path appeared less smooth than that observed in laboratory air. Measurements of the relative heights of the fatigue crack path from the centerline of the FIB micro-notch for crack lengths $2c \leq 200$ μm for each P_{H2O} studied are shown in Figure 4.17. This can be interpreted as a measure of crack path tortuosity, indicating whether the crack path adhered closely to crystallographic planes or if the crack propagation plane rather preferred being normal to the loading direction regardless of specific crystallographic planes. Additionally, the deviation of the crack path above and below the micro-notch centerline decreased with decreasing P_{H2O}, indicating the crack propagation plane preferred being normal to the loading direction regardless of specific crystallographic planes at lower P_{H2O}.

In environments containing water vapor (>65 Pa) and oxygen, the surface crack path strongly correlated with single slip planes (mainly basal planes in α_p grains), and faster crack growth rates were observed compared to vacuum and hydrogen. Vacuum and H_2O vapor environments at the lower pressures had flatter crack paths than laboratory air and also lower fatigue crack growth rates. The crack paths were also more difficult to classify in terms of correlation with specific crystallographic planes and would frequently change slip planes within a grain, producing a characteristic zig-zag behavior. These observations point to multiple slip systems being operative at the crack-tip. As discussed in Section 2.2.2.1, other studies have suggested that the nature of slip at the crack-tip is correlated with crack growth rates. Bowen et al. [77] investigated the effects of crystallographic orientation on crack growth rates in Ti-6Al-4V and observed that symmetric deformation about the crack-tip leads to nominally flat fracture surfaces and lower

fatigue crack growth rates. It was reasoned that symmetric deformation about the crack-tip acts as a toughening mechanism, thereby increasing the ability of the microstructure to accumulate more cycles before crack advance. Asymmetric deformation about the crack-tip correlated with faster crack growth rates because slip was localized within a single slip system. These observations were in line with studies by Krupp et al. [78] on a β-Ti alloy that showed that crack growth rates were higher if a single slip system was activated at the crack-tip than if multiple slip systems were activated. The results of the present work are in agreement with both of these studies.

Bache et al. [97] have also suggested that oxygen may lower the stacking fault energy in titanium, thereby promoting single slip. A more recent study by Qian et al. [132] that studied the effect of oxygen solutes on strengthening effects in α-Ti using TEM showed that oxygen interacts strongly with screw dislocation cores and has strong pinning effect on screw dislocations. More work is needed to determine the mechanisms governing this behavior and the effect it may have on small crack growth behavior in environments containing water vapor and oxygen at ultrasonic frequencies.

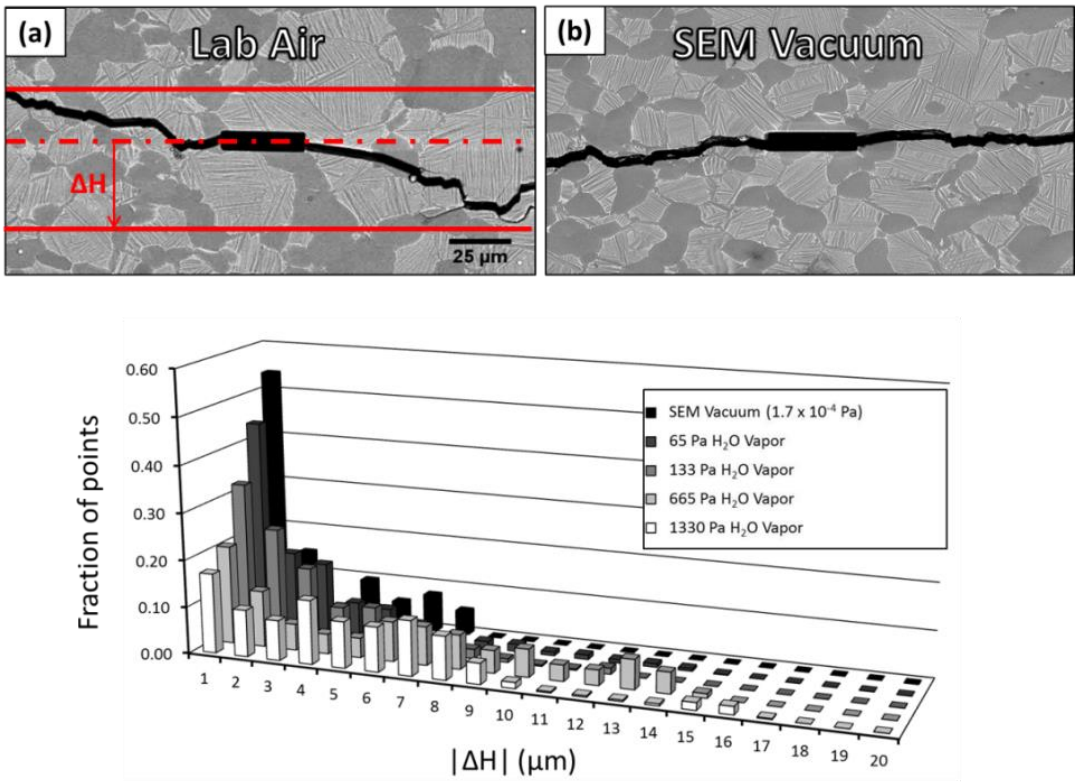

Figure 4.17: Measurements of the relative heights of the fatigue crack path from the centerline of the FIB micro-notch for each P_{H2O} studied are shown. The deviation of the crack path above and below the micro-notch centerline decreased with decreasing P_{H2O}, indicating the crack propagation plane preferred being normal to the loading direction regardless of specific crystallographic planes at lower P_{H2O}.

4.5.2 Effects of Microstructural Barriers on Fatigue Crack Growth

Significant local variability in the small fatigue crack growth rate was observed in each environment, and was frequently correlated with the interaction of the crack-tip with microstructural features such as high misorientation angle grain boundaries and phase boundaries. Figure 4.18 shows a fatigue crack that propagated in laboratory air along basal planes in two neighboring primary α grains for 3.0 x 10^4 cycles before arresting for the duration of the test (3.1 x 10^5 cycles) at an α/α grain boundary with a misorientation of approximately 80° (where the misorientation is defined using the axis/angle method, in which the minimum angle about any arbitrary axis needed to bring the two grains into coincidence is provided). Figure

4.19 shows a fatigue crack grown in 133 Pa H_2O vapor that arrested for approximately 10^5 cycles at an $\alpha/\alpha+\beta$ phase boundary. The misorientation angle between these two grains was low and likely not responsible for the reduction in crack growth rate observed at this boundary. Rather, this reduction may likely be an effect of the crack crossing from a primary α grain to a transformed β phase region, as lamellar regions have higher fatigue crack growth resistance [25]. Crack arrest at the grain boundary may also have been affected by the low basal Schmid factor of the transformed β region, as grains that are unfavorably oriented for basal slip have been observed to impede crack growth in titanium alloys [83].

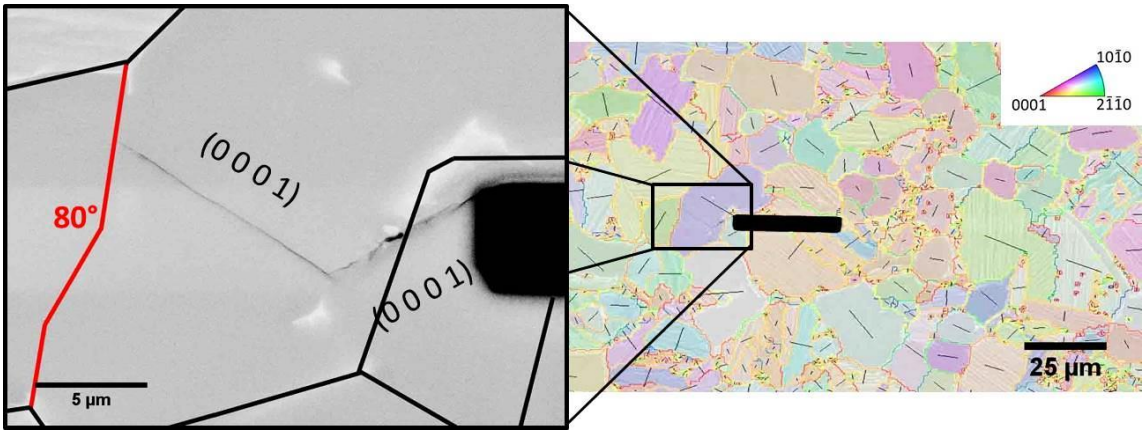

Figure 4.18: A small fatigue crack was initiated and grown in laboratory air. The right image shows the local microstructure surrounding the notch with the IPF map overlaid, where black lines denote basal plane traces. The SEM micrograph on the left shows the fatigue crack propagated along basal planes and arrested at a high angle α/α grain boundary after 3.0 x 10^4 cycles.

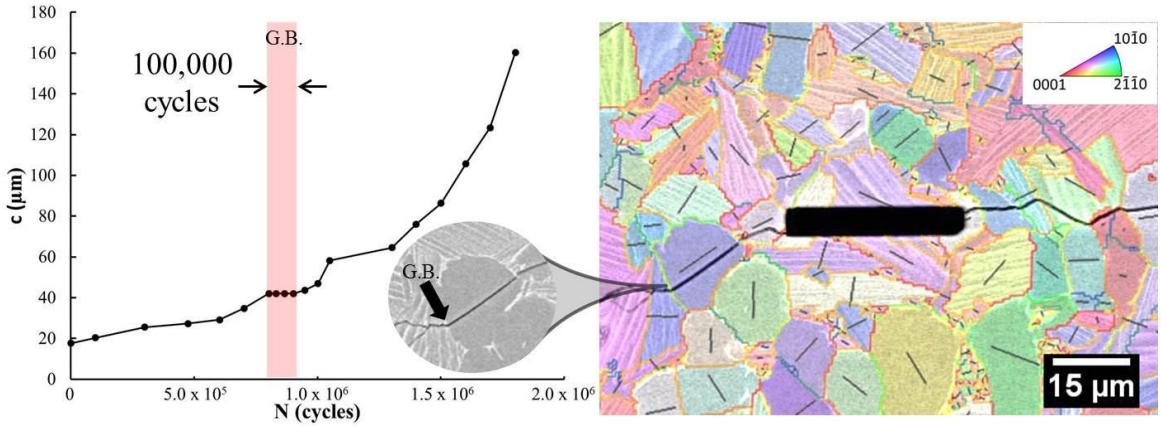

Figure 4.19: A small fatigue crack was initiated and grown in 133 Pa H_2O vapor. A micrograph of the local microstructure surrounding the notch and the propagated crack with the IPF map overlaid is shown. The black lines denote basal plane traces. The left side fatigue crack propagated along basal planes in α grains and arrested at the $\alpha/\alpha+\beta$ phase boundary indicated by the arrow for approximately 10^5 cycles.

In order to highlight the influence of environment on small crack growth behavior, especially as it relates to microstructural barrier effects, experiments were conducted in which the environment was changed as a crack grew to a grain boundary. The results of an experiment in which a crack was initiated and grown from a FIB micro-notch in laboratory air followed by cycling in vacuum is shown in the annotated *c* vs. *N* plot of Figure 4.20. The fatigue crack was initiated in lab air and allowed to propagate in air for 10^5 cycles. Position (a) in Figure 4.20 shows the location of a crack-tip near a grain boundary at this point. The UF-SEM system was then used and the specimen was cycled for 10^7 cycles in vacuum. Very little crack growth was observed during this period as shown by Fig. 4.20(b) and the crack arrested at the grain boundary. The environment was returned to laboratory air and the crack grew through the grain boundary within 4,000 cycles (1 pulse). The crack growth rates in laboratory air both before and after the vacuum cycling were approximately 10^{-9} m/cycles. It is possible that subsurface crack growth occurred during fatigue cycling in vacuum. Nevertheless, these experiments demonstrate that the efficacy of barriers such as grain boundaries to short fatigue crack propagation may

depend significantly on environment. Cracks in laboratory air have higher fatigue crack growth rates than vacuum and are less likely to decelerate or arrest for long periods at grain boundaries. This is in agreement with the notion that localized slip along a single slip system in air is more severe than the symmetric deformation behavior possibly active in vacuum. It has also been suggested that an arrested crack may re-initiate at the other side of the grain boundary. This was not detected in this work, but cannot be ruled out.

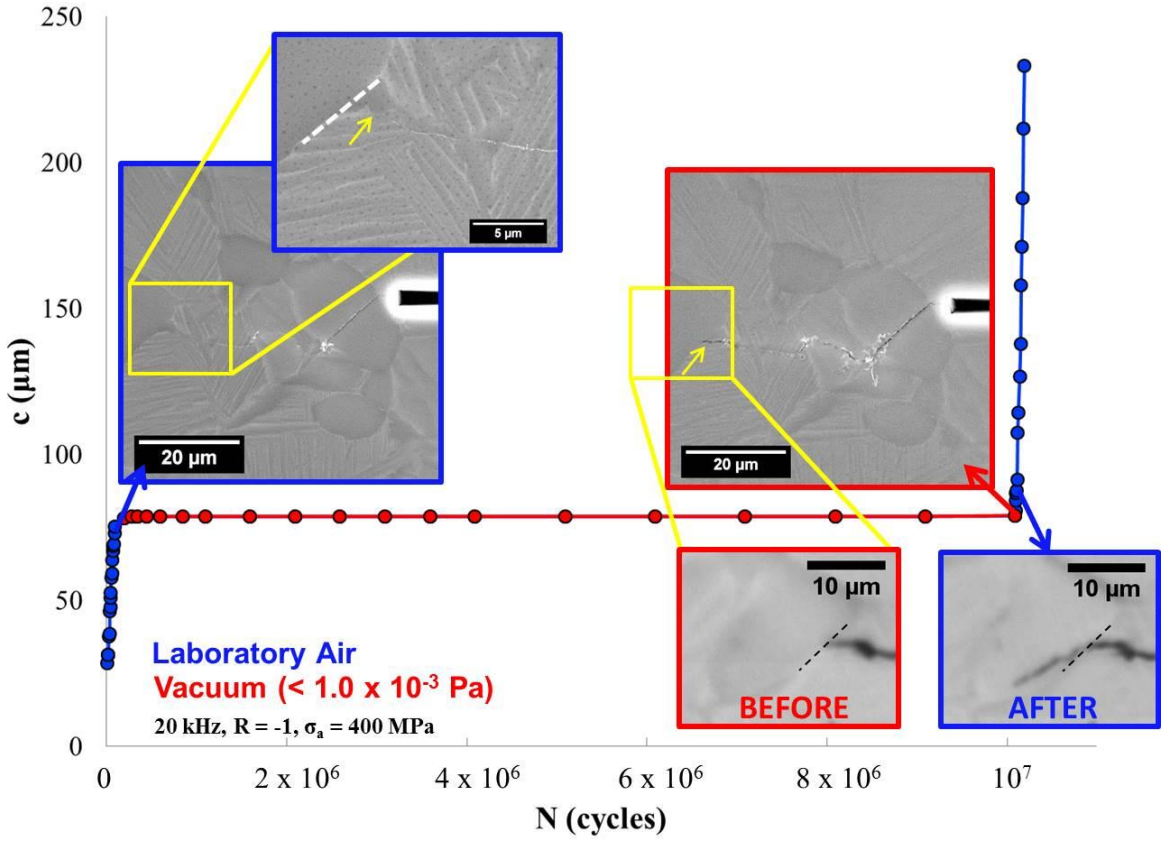

Figure 4.20: Crack length (c) vs. cycle number (N) for a small fatigue crack initiated in laboratory air and then fatigued in vacuum is shown. The fatigue crack was grown in laboratory air for 10^5 cycles before the system was placed in vacuum and cycled for an additional 10^7 cycles. The crack was arrested at the indicated grain boundary and very little crack growth was observed during fatigue in vacuum. After the specimen was returned to the laboratory air environment, the crack grew past the grain boundary and returned to an expected fatigue crack growth rate for laboratory air. It is evident that the efficacy of barriers such as grain boundaries to short fatigue crack propagation may depend significantly on environment.

4.6 Fractographic Analysis of Fatigue Cracks

Fractographic examination of the fatigue fracture surfaces produced in this work revealed that they were generally similar for the various environments studied, despite marked differences in small fatigue crack growth rates. In other words, there were no abrupt transitions in fracture surface appearance when a transition was made between environments, although some distinct micro-features could be observed on fatigue fracture surfaces, especially those produced in vacuum, as compared to air. This section discusses these observations.

4.6.1 Laboratory Air and Vacuum Observations

Representative fracture surfaces of the early crack growth regions for cracks grown in vacuum and laboratory air showed the greatest difference in appearance. As shown in Figure 4.21 and 4.26, smoother, more faceted regions were generally observed in laboratory air compared to vacuum. Large areas of finer, ductile fracture, as shown in the higher magnification image of Figure 4.22, were observed on the vacuum fracture surfaces. While smooth facet-like features were seen in the vacuum and laboratory air fracture surfaces, these rougher, small-scale ductile fracture regions were only observed on fracture surfaces of specimens tested in vacuum. For example, Figure 4.23 shows the fracture surface of another specimen fatigued in vacuum where the finer scale ductile fracture features were produced, similar to those observed in Figure 4.22. Figure 4.23 also shows high resolution images of two facet-like features. High magnification imaging of these facet-like features shows a surface character more indicative of a slowly advancing crack rather than a fast, cleavage type mechanism. This is in line with the slow crack growth rates in vacuum and the idea that it likely takes many cycles to traverse these features.

Figure 4.24 (a) shows a fractograph from an investigation on fatigue crack propagation of Ti-6Al-4V in vacuum (10^{-5} – 10^{-7} Pa) environments conducted by Oguma and Nakamura [133]. They observed a granular region on sub-surface fracture surfaces of specimens failed at 60 Hz, R = 0.1, σ_{max} = 600 MPa, and N_f = 5.53 x 10^7 cycles. These regions are similar in appearance to the fine scale regions that were formed on fracture surfaces produced by crack propagation in vacuum in this work. They reasoned that the cause of these fine granular regions was a cold-welding, or re-bonding, of surfaces at the crack-tip followed by microstructure refinement under continued cycling. This mechanism is also proposed as an explanation for the slower propagation of cracks in vacuum compared to laboratory air. They also acknowledged that the difference in crack growth rates in air versus vacuum could not be fully understood based on crack closure effects alone. This behavior is plausible in relation to this study given that tests were conducted under fully reversed loading conditions (R = -1) in which case any operative crack closure mechanisms would be amplified.

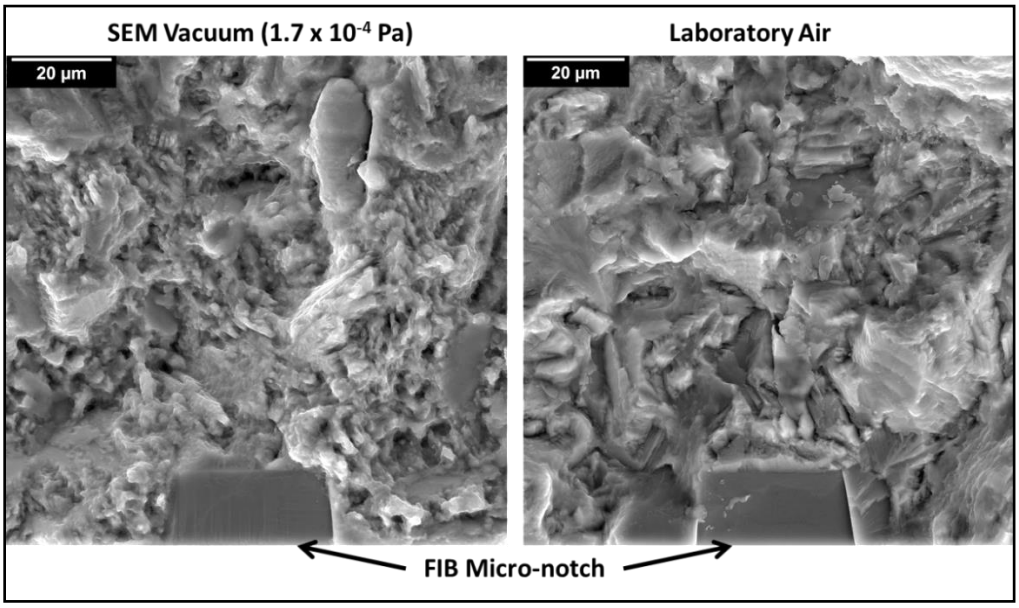

Figure 4.21: Comparison of fracture surfaces from vacuum and laboratory air test is shown. More smoother, faceted regions occurred in laboratory air. Significant areas of finer, ductile fracture features occurred in vacuum.

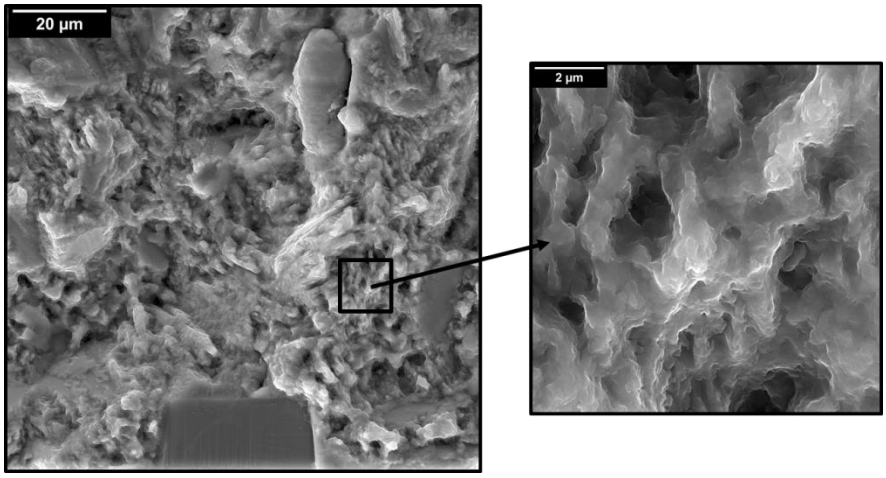

Figure 4.22: High magnification of ductile fracture in vacuum test. Such regions are not observed in laboratory air.

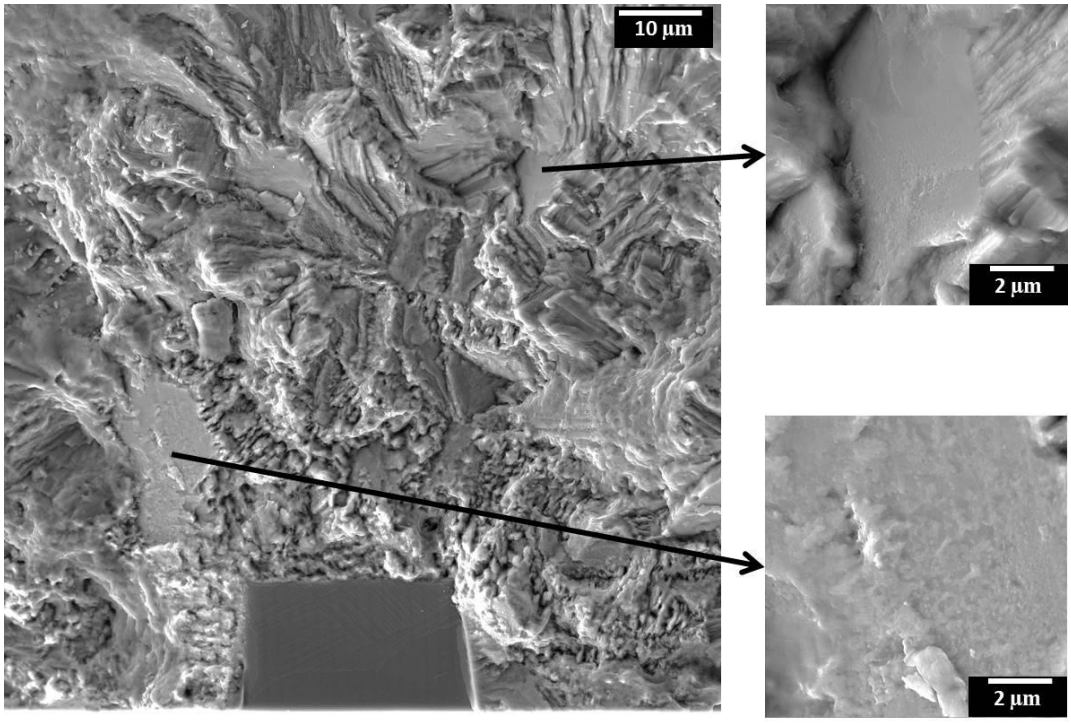

Figure 4.23: A fracture surface produced by fatigue in vacuum is shown. Fine, ductile fracture regions are observed similarly to the fracture surface shown in Figure 4.22. High magnification images of two facet-like features are also shown. The roughness of these features is more indicative of a slowly advancing crack rather than a fast, cleavage type mechanism.

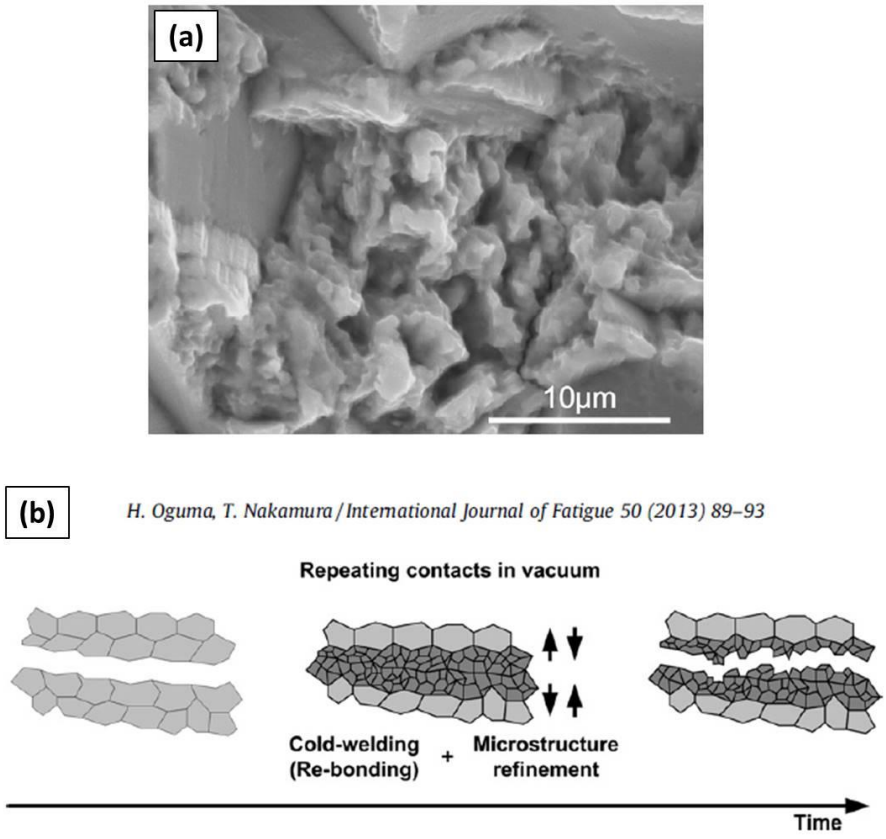

Figure 4.24: (a) A similar fine, ductile fracture region from fatigue in vacuum of a Ti-6Al-4V alloy specimen tested by Oguma and Nakamura [133] is shown. (b) A schematic of the mechanism for formation of these regions is illustrated. Cold-welding of fresh crack surfaces at the crack-tip leading to microstructure refinement with repeated cycling is proposed.

Evidence of crystallographic, microstructurally sensitive fatigue crack growth was observed on laboratory air fracture surfaces, in agreement with surface crack path observations. The fracture surfaces of fatal cracks propagated in laboratory air showed primary α grain faceting during early crack growth. EBSD maps of fractured primary α grains that intersected the specimen surface indicated that low ΔK crack advance (< 5.0 MPa-m$^{1/2}$) took place mainly along basal planes, but likely took fewer numbers of cycles for facet formation. Higher magnification micrographs of smooth faceted surfaces showed little to no striation-like markings (Figure 4.26), in contrast with the features shown on a faceted primary α grain in Figure 4.25. The presence of

these markings can indicate a more ductile fracture process, as compared to faster, brittle cleavage-like fracture. This was in agreement with the observed increase in fatigue crack growth rate in laboratory air versus vacuum environments, where a faster fracture in laboratory air produced fewer fatigue markings on faceted planes. Some facets with coarse band-like features were also observed in the laboratory air experiments, but not in the saturated water vapor and vacuum environments at equivalent crack lengths.

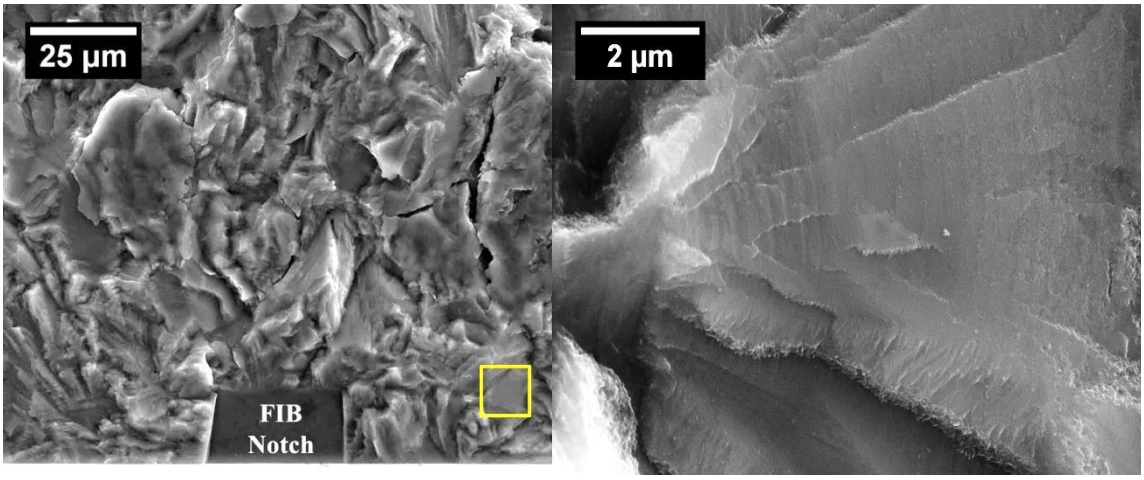

Figure 4.25: SEM micrograph of the fracture surface of a fatal crack propagated in the 133 Pa saturated water vapor environment. The right image is a magnification of the yellow box in the left image, and shows a macroscopically smooth primary α facet with distinct crack growth features indicating that the facet was created by a slowly advancing crack ($dc/dN \approx 1.8 \times 10^{-10}$ m/cycle) rather than a cleavage mechanism. The crack propagation direction is from bottom to top.

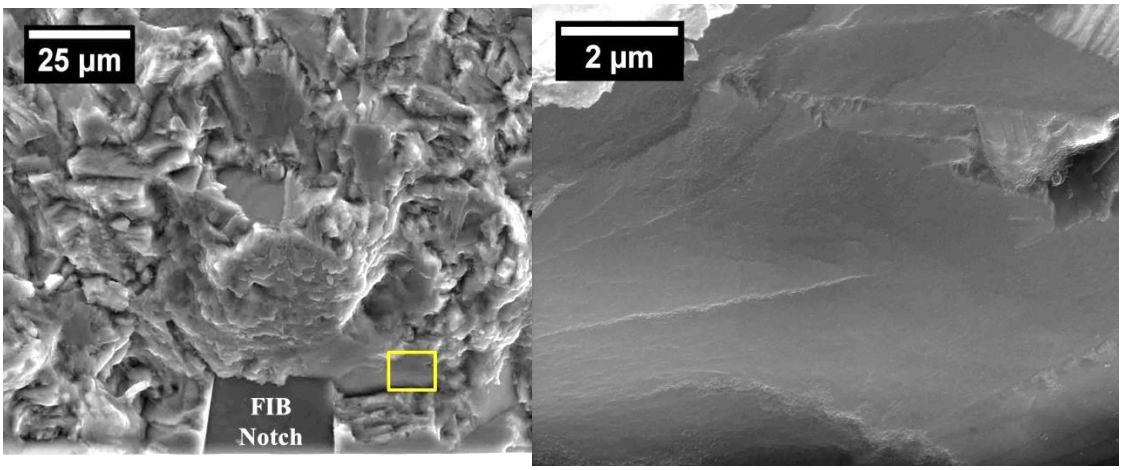

Figure 4.26: SEM micrographs of the fracture surface of a fatal crack propagated in laboratory air. At right is a magnification of the yellow box in the left image, and shows a macroscopically smooth primary α facet with no striation-like features. The crack propagation direction is from bottom to top ($dc/dN \approx 6.2 \times 10^{-10}$ m/cycle).

4.6.2 Fracture Surface Observations from Water Vapor, Oxygen, and Hydrogen Testing

Figure 4.27 shows representative fracture surfaces of the early crack growth regions from specimens tested in laboratory air, 1330 Pa H_2O vapor, and 1330 Pa O_2. Similar features, namely macroscopically smooth surfaces and material indicative of fracture surface contact, can be seen on all three surfaces. No significant difference in fracture surface characteristics could be discerned between these three environments, even though FCGRs differed by about a factor of two between the 1330 Pa H_2O vapor and 1330 Pa O_2. A similar fracture surface appearance between laboratory air and 1330 Pa H_2O vapor was observed. This does not mean that the fatigue crack growth processes in these two environments were the same, but the similar appearance of the fracture surfaces is in line with the similar FCGR.

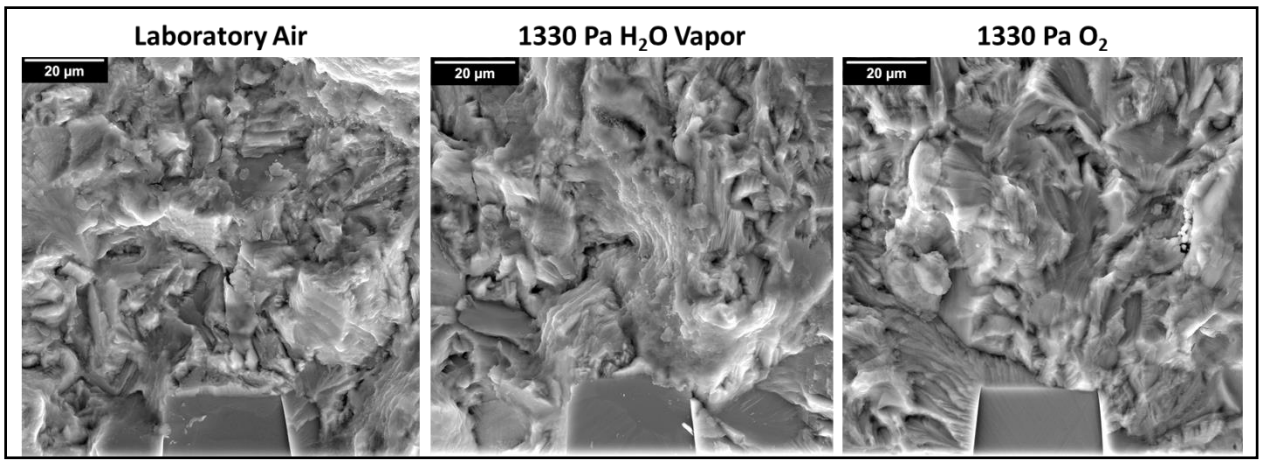

Figure 4.27: Comparison of fracture surfaces from laboratory air, 1330 Pa H_2O vapor, and 1330 Pa O_2 test. No significant differences were observed.

In environments containing only water vapor, fatigue cracks also propagated crystallographically and were microstructurally sensitive in the low ΔK regime. Observed fracture surface features for the two low vacuum water vapor environments (65 Pa and 133 Pa) were similar, consistent with the moderate difference in fatigue crack growth rate between them. Example fractographs obtained in the early crack growth region for laboratory air, 133 Pa H_2O, and 65 Pa H_2O are shown in Figure 4.28. Smooth faceted crack growth across primary α grains was observed for $\Delta K < 7.0$ MPa$\sqrt{m}$, as shown in Figure 4.28. Correlation of primary α grain facets with the adjacent surface EBSD maps showed that faceting predominantly occurred along basal planes. Higher magnification imaging of faceted surfaces revealed crack growth markings, or bands, indicative of a slowly advancing crack, rather than a cleavage-like fracture mechanism. The frequency of primary α facets decreased with increasing crack length. This is attributed to an increase in the crack-tip stress intensity as the crack gets longer and thus, an increase in plastic deformation at the crack-tip.

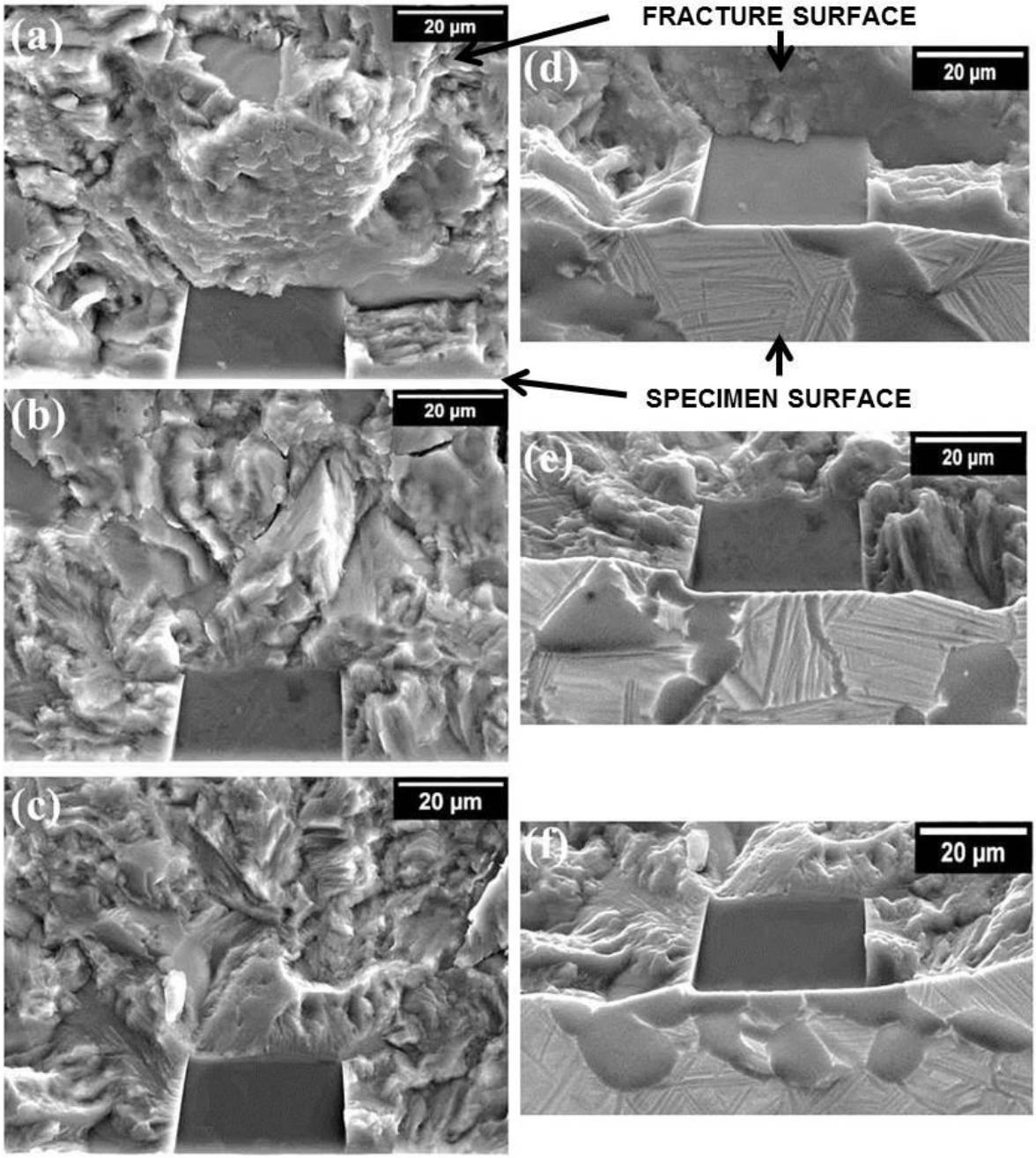

Figure 4.28: Fracture surfaces of fatal cracks for (a) laboratory air, (b) 133 Pa H_2O vapor, and (c) 65 Pa H_2O vapor. The images on the left show the specimen fracture surface as viewed along the loading direction. The images on the right show the corresponding fracture surfaces on the left with a BSE image of the adjacent surface microstructure as viewed by a 45° tilt with respect to the loading direction. Faceted fracturing is observed in each of the test environments in the early stage crack growth region.

4.6.3 Evidence of Oxide Formation of Fatigue Fracture Surfaces

In many of the *in situ* tests material was extruded from the crack faces, which then adheres to the specimen surface, as shown in Figure 4.29. This phenomenon was observed in numerous tests and depended on the local microstructure and environment. The test shown in Figure 4.29 was conducted in vacuum, and exhibited a transition from a feather-like extrusion in a primary α grain to a more globular morphology in the adjacent transformed β region. The frequency and amount of extruded material observed on specimen surfaces was greater in fatigue tests conducted in vacuum and partial pressures of water vapor than in laboratory air. However, the specimens tested in laboratory air were subjected to high velocity air jets, which likely removed extruded material. Sugano et al. [134] observed similar ribbon-like extrusions on the surface of titanium alloy specimens in vacuum fatigue tests at a pressure of 6.7×10^{-3} Pa, R = -1, and 10^8 cycles at approximately 1 kHz, which occurred at slip bands on the specimen surface. They also observed a decrease in intensity and fraction of these extrusions in specimens fatigued in laboratory air versus vacuum environments. In this dissertation work, the intensity of these features increased with increasing numbers of cycles, especially for arrested cracks. Thus, it is reasonable that the intensity and occurrence of these features would be greater in vacuum than laboratory air testing that exhibited higher FCGR and lower lifetimes. The mechanism for the creation of these features may also be related to crack closure effects and oxide layer formation. Under the fully reversed loading conditions used in this work, fracture surface contact during the unloading portion of cycling would likely lead to the destruction of the oxide layer, which would form again during loading. The continuous destruction and regeneration of the oxide layer could lead to a build-up of oxide material. More simply, the rubbing together of the opposing fracture surfaces may also be the cause of these features.

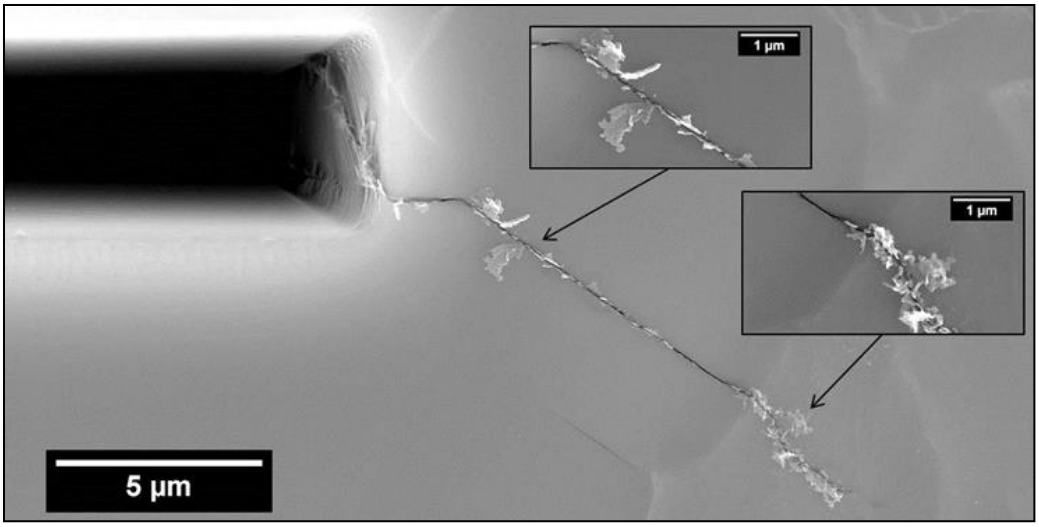

Figure 4.29: SEM micrograph of extruded material from a surface crack of a specimen fatigued in vacuum (3.7×10^{-4} Pa). The extruded material transitions from a thin feather-like structure in the primary alpha grain to a globular extrusion upon entering the adjacent lamellar region.

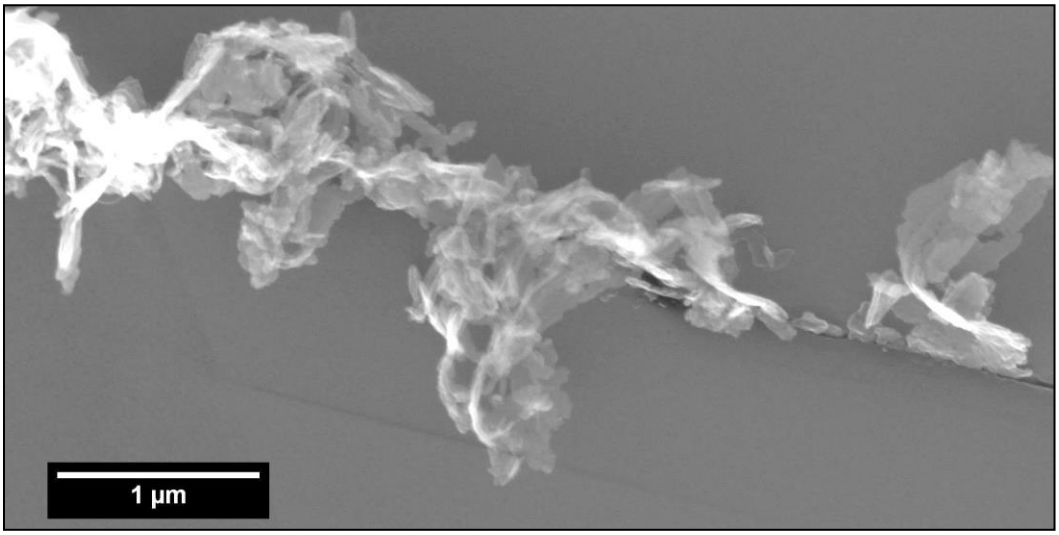

Figure 4.30: High magnification image of material from a surface crack of a specimen fatigued in vacuum.

4.7 Process of Environmental Effects of Small Fatigue Crack Growth

This section discusses the processes that govern the observed environmental effects on small crack growth rates in ultrasonic fatigue. As reviewed in Section 2.3.1, the possible processes responsible for the environmental effect on small fatigue crack growth rates in titanium alloys are: crack-tip blunting, oxidation or adsorption assisted cracking, and hydrogen assisted cracking. The reference fatigue crack growth rate for a purely mechanical fatigue crack will be taken as the vacuum environment. The first section provides a description of the possible processes leading to enhanced fatigue crack growth in each of the environments studied, specifically, vacuum, water vapor, oxygen, and hydrogen. Section 4.7.2 will detail the steps in the processes that control environmentally assisted crack growth behavior based on calculations relating the observed fatigue crack growth rates and the proposed reactions that take place at the crack-tip.

4.7.1 The Processes for Environmental Influence on Small Fatigue Crack Growth

4.7.1.1 Intrinsic (Vacuum) Fatigue Crack Growth

In prior studies that investigated fatigue crack growth in titanium alloys in vacuum, FCGRs were lower in vacuum than in air [133-137]. The present study shows the same result, even though tests were conducted at 20 kHz instead of the lower frequencies (0.5 – 60 Hz) associated with conventional fatigue testing. Given that the surface and fracture surface observations of cracks grown in vacuum included crack growth on non-crystallographic planes, branching and reinitiating of cracks, and ductile fracture regions, crack-tip blunting may be a significant process in vacuum testing. Fresh surfaces produced at the crack-tip of cracks propagating in vacuum are not subject to the same degree of oxide layer formation as cracks growing in air, water vapor, and oxygen environments. In the absence of a passivating oxide layer or adsorbed gas molecules,

dislocation glide on slip planes at the crack-tip is likely easier and the amount of irreversible slip per cycle would be expected to be less in the vacuum environment. This enhanced slip activity, and possibly the activation of multiple slip systems can ultimately result in the fatigue crack in vacuum being able to withstand more cycles before crack advance than would be observed in air. Further sliding could then lead to crack-tip blunting and lower crack growth rates in vacuum. The possibility of rewelding of crack face surfaces may also contribute to the lower fatigue crack growth rates in vacuum as discussed in Section 4.6.1.

Another possible explanation for lower crack growth rates in vacuum is that there is local heating at the crack tip. Sugano et al. [134] reported a sharp increase in fatigue lifetimes (of nominally 500,000 cycles) for a pressure reduction from 10 Pa to 1 Pa in pure Ti up to a testing frequency of 1 kHz. They attributed this increase to gas absorption processes and internal frictional heating of the specimen in vacuum that led to increased plasticity at the crack-tip. A model was postulated for which heating of active slip planes at the crack-tip, on the order of 200°C, caused a decrease in fatigue crack growth rates through crack-tip blunting and the development of compressive residual stresses around the plastic zone of the crack-tip. In the present study, the overall specimen temperature was maintained to within 40°C of the ambient temperature using a pulse/pause duty cycle, so temperature is not believed to have a significant effect on the observed crack growth behavior. This is further substantiated by the significant differences observed in crack growth rates even for quite low partial pressures of gases, where substantial differences in temperature from that in vacuum would not be expected.

4.7.1.2 Effects of Water Vapor and Oxygen on Small Fatigue Crack Growth Behavior

The processes responsible for the detrimental effects of water vapor and oxygen on fatigue crack growth rates in titanium alloys are not yet resolved. In the present study, the growth rates

of small fatigue cracks at H_2O pressures of 1330 Pa and 133 Pa were consistently higher than in O_2 at equivalent pressures, while the rates for 1330 Pa H_2O and laboratory air were similar. The differences in fatigue crack growth rates in oxygen and water vapor at the same pressure suggests a difference in the role of each species in promoting increased FCGRs over vacuum, possibly stemming from a difference in oxidation behavior.

Oxide formation on fresh surfaces at and near the crack-tip has been suggested as a potential cause for the observed increase in FCGR in laboratory air, water vapor, and oxygen environments [91, 92]. The oxide develops from chemical reactions involving Ti and H_2O or O_2 molecules with the characteristics of the oxide depending on many factors including material microstructure, surface condition, gas pressure, and temperature [124, 127]. Hydrogen is also produced as a byproduct of oxide formation in laboratory air and water vapor containing environments, and likely plays a significant role in the increased FCGR in these environments compared to oxygen. Chemical reactions of Ti with H_2O and O_2 that lead to oxide formation are given in Equations 4.1 and 4.2. While the exact steps and products of these reactions are still debated, there is some agreement on the more likely reactions at low pressures based on work by [138] and [116] this is represented by Equations 4.1 and 4.2.

$$Ti + H_2O \rightarrow TiO + H_2 \tag{4.1}$$

$$Ti + O_2 \rightarrow TiO_2 \tag{4.2}$$

Water Vapor

The effects of moisture levels in atmosphere and at low pressures on oxidation kinetics has been studied in many metallic materials including aluminum alloys, magnesium alloys, high strength steels, and titanium alloys. Furthermore, it is commonly accepted that most transition metals dissociate chemisorbed water at room temperature. This dissociation may be complete,

partial, or a combination of the two. In titanium alloys, water vapor reacts with fresh titanium surfaces to produce a stable oxide layer, similarly to oxide formation with exposure to pure oxygen. However, the formed TiO monolayer is not as passive or as thick as the native (oxygen produced) oxide layer, which is mainly comprised of TiO_2. Additionally, no titanium oxides higher than TiO are observed with water vapor exposure to pure titanium surfaces at room temperature, as shown in Equation 4.1 [115, 127].

Several researchers have used Auger electron spectroscopy (AES) and x-ray photoelectron spectroscopy (XPS) to find that exposure to water vapor leads to the presence of hydrogen and hydroxides within the oxide layer [98, 115, 127]. These products may form by an intermediate reaction step in the dissociation of water molecules on Ti surfaces. Gao et al. [98] also reported that oxidation by H_2O is less severe than by O_2 at room temperature, suggesting that H and OH may play an important role in oxide layer formation in the presence of water vapor. The production of hydroxides and hydrogen atoms in oxidation by water vapor, but not oxygen, may be critical to processes leading to faster fatigue crack growth behavior in water vapor compared to oxygen. Indeed, Gao et al. investigated surface reactions and fatigue crack growth in Ti-5Al-2.5Sn and Ti-6Al-4V at 5 Hz in water vapor and reasoned that enhanced fatigue crack growth in water vapor was the result of embrittlement by hydrogen produced by the Ti and H_2O reaction. More recently, Smith and Piascik [91] used XPS analysis to study the fracture surface of Ti-6-2-2-2-2 samples fatigued in 67 Pa water vapor environments at room temperature at loading frequencies of 0.5 and 5 Hz. By conducting XPS analysis of fracture surfaces, they found that a hydroxide based film is formed at 24 °C and an oxide/hydroxide film is formed at 177 °C. At the water vapor pressures investigated in this work, a significant amount of water vapor can be dissociated at fresh Ti surfaces and result in increased concentrations of atomic hydrogen.

Hydrogen atoms can then diffuse into the crack-tip plastic zone, where hydrogen has been shown to embrittle titanium alloys [106]. Increased hydrogen uptake can also be facilitated by formation of a hydroxide-based film, rather than the more passive native or oxygen produced oxide layer. Based on this, it is proposed that increased small fatigue crack growth rates in laboratory air and water vapor are caused by the adsorption of water vapor molecules on fresh crack surfaces, generation of an oxide/hydroxide layer, and hydrogen assisted cracking as shown in the schematic of Figure 4.31. More work is needed to determine if the interaction of the diffused hydrogen atoms and whether or not hydrogen embrittlement or hydrogen enhanced local plasticity (HELP) mechanisms are operative.

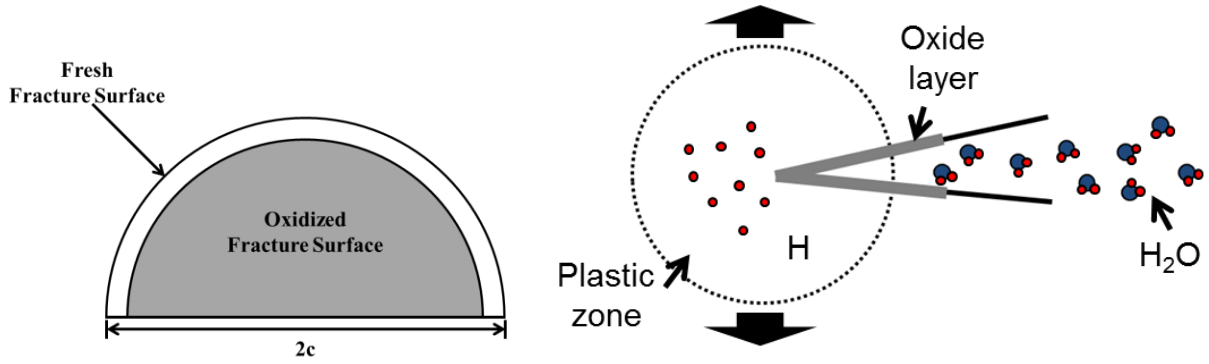

Figure 4.31: A schematic illustrating the proposed process of increased fatigue crack growth rates in the presence of water vapor is shown. First, water vapor molecules migrate to the crack-tip. During the loading portion of the fatigue cycle, a fresh fracture surface is created in front of the oxidized fracture surface. The water vapor reacts with the fresh fracture surface, generating a newly oxidized surface and releasing hydrogen atoms that diffuse into the crack-tip plastic zone. The crack growth rate is accelerated by impeded reverse slip due to both the oxide layer and diffused H that can cause hydrogen embrittlement or HELP behavior [106].

Oxygen

The rapid convergence of FCGRs in O_2 gas to laboratory air FCGRs at oxygen pressures that are approximately 15 times less than ambient is in agreement with the fast formation and saturation behavior of titanium oxidation even in the presence of small amounts of oxygen. Even at the vacuum pressures used in this study (1.7×10^{-4} Pa), it is possible that trace amounts of oxygen present in the SEM chamber may have influenced oxidation behavior, and thus FCGRs. Vaquila et al. [116] observed that titanium oxidation proceeds immediately upon exposure to even lower pressures of O_2 (4×10^{-7} Pa) with a negligible oxygen adsorption stage. This finding is consistent with other investigations, which reported a fast adsorption of oxygen at the top most surface layer followed by a slower uptake of oxygen until saturation [115, 124].

General agreement is that the topmost oxide layer is composed primarily of TiO_2. In some cases TiO_2 has been identified as the only product of the reaction of titanium with oxygen as indicated by Equation 4.2 [116]. However, some researchers have observed lower oxidation states present near the oxide/metal interface [124]. The kinetics of the oxidation reaction with titanium have been found to be highly dependent on the pressure as well as the exposure time. The oxidation efficiency of oxygen as compared to water vapor also varies with temperature. For example, Gallerie et al. [126], observed oxidation is faster by water vapor than oxygen at 1123K. However, at 300K oxygen appears to be a more efficient oxidizer than water vapor [127].

In the present work, the cause of increased small fatigue crack growth rates is reasoned to be the fast adsorption of oxygen atoms on fresh crack surfaces near the crack-tip, and subsequent formation of an oxide layer that impedes reverse slip of slip planes during the unloading portion of the fatigue cycle. This causes increased irreversibility and higher FCGRs. Work by Swanson and Marcus [139] points to the possibility of such a mechanism. They performed fatigue

experiments on pure titanium in vacuum and the isotope oxygen-18 to obtain a better understanding as to whether increased FCGRs in oxygen are the result of cyclic stress corrosion or if gaseous species are transported into the material and internal interaction with the deformation behavior occurs (higher ΔK of 22 MPa-$m^{1/2}$). AES and Secondary Ion Mass Spectroscopy (SIMS) were used at fatigue crack surfaces to determine that oxygen was transported into the metal by the passing fatigue crack. It was postulated that the interstitial oxygen atoms then interacted with the metal, significantly modifying the local plastic behavior and the fracture strain near the crack-tip.

The stable oxide layer that forms also passivates the surface; it is likely that only a thin monolayer of oxide is necessary to affect FCGRs given the fast formation and saturation behavior of its formation. This proposed process is supported by the lower FCGR in oxygen compared to water vapor at similar pressures, as there would be no accompanying hydrogen enhanced cracking mechanism in O_2 gas. The protective nature of the oxide layer would also limit hydrogen enhanced cracking mechanisms that may occur due to hydrogen impurities in the environment. Many researchers have shown that oxide films on surfaces slow down or completely inhibit absorption of hydrogen by titanium [140, 141]. In fact, the reaction probability of gaseous hydrogen was found to decrease by up to five orders of magnitude if the titanium had been pre-covered with monolayers of oxygen [142].

Oxide layer formation has been shown to increase crack closure effects, thereby lowering the local crack-tip stress intensity and causing lower fatigue crack growth rates [143]. In this study, fatigue experiments were carried out under fully reversed loading and crack closure effects may be significant. However, no crack closure measurements were made and the contribution of crack closure effects to small fatigue crack growth rates is unknown. It is reasonable to postulate

that the rapid formation of the oxide layer combined with the destruction of this layer by the contacting crack surfaces would result in more oxide debris being formed with repeated cycling in oxygen containing environments. However, no substantial increase in the amount of oxidation on fracture surfaces for specimens failed in laboratory air or oxygen versus vacuum or hydrogen was observed.

4.7.1.3 Effects of Hydrogen on Small Fatigue Crack Growth Behavior

The first step in the reaction of hydrogen gas with pure titanium is a dissociative adsorption of hydrogen. Elsworth et al. [144] reported that the sticking coefficient of hydrogen on titanium at 293 K was approximately 0.085, derived from multiple sorption experiments. It has also been concluded that dissociation of H_2 molecules on the titanium surface is the rate-limiting step, and that hydrogen diffuses into titanium in the form of atoms [145]. Once diffused, the hydrogen atoms can either locate within the titanium lattice to cause hydrogen embrittlement processes or react further to produce titanium hydrides. The processes determining which route the diffused hydrogen atoms will ultimately take and the effects of diffused hydrogen atoms and hydride formation on the mechanical properties of titanium alloys are not well understood.

A possible mechanism for the increased fatigue crack growth rates in H_2 environments compared to vacuum observed in this study is hydrogen enhanced local plasticity (HELP) caused by diffused atoms within the titanium lattice. Robertson and Birnbaum [146] summarized numerous TEM studies that reported the influence of hydrogen on dislocation mobility. Shih et al. [106] also observed a change in fracture mechanism from stress-induced hydride formation and cleavage to a hydrogen assisted localized plasticity mechanism in the case where crack growth rates were too high for hydride cleavage. During this process, the presence of hydrogen gas causes slip localization in areas of increased hydrogen concentration. E. Tal Gutelmacher et

al. [147] examined the effects of high pressure hydrogen gas (~0.5 MPa) at 350 °C on a duplex and beta annealed Ti-6Al-4V alloy using X-ray diffraction (XRD), SEM and TEM microscopy, a hydrogen determinator, and thermal desorption spectroscopy (TDS). They did not observe hydride precipitation and reasoned that this was due to the relatively small hydrogen concentration absorbed, approximately 44 to 312 ppm wt. for duplex Ti-6Al-4V. Since this study was done at a higher pressure than the work by Shih, it is more likely that hydride precipitation was not observed because they were studying unstressed samples. Nonetheless, they concluded that hydrogen induces strain in both beta-annealed and duplex Ti-6Al-4V by increasing their unit cell volumes and enhancing dislocation motion as measured by TEM.

Another possible mechanism for the moderately increased FCGR in H_2 gas compared to vacuum during ultrasonic fatigue is the strain-induced hydride formation model proposed by Shih et al. [106]. At low stress intensities (less than K_{Ic} of the α phase), corresponding to slow crack growth rates, fracture proceeded by a stress-induced hydride formation and cleavage mechanism as observed by *in situ* TEM observations of cracking in an α-Ti alloy. They observed the nucleation and growth of hydrides at elastic singularities and that the accommodation of the stress field around the hydride was partially elastic and partially plastic. The presence of hydrides at the crack-tip was shown to decrease the local stress intensity at the crack-tip. Continued cracking occurred once the local stress intensity exceeded the critical stress intensity for hydride fracture. It is important to note that the work of Shih et al. was carried out at a much higher H_2 pressure of 13 – 16 kPa.

The proposed process for increased FCGRs in H_2 gas compared to vacuum during ultrasonic fatigue is likely governed by hydrogen-dislocation interactions, or HELP mechanisms. Hydride formation is unlikely given the low pressures of H_2 gas used in this work (133 and 1330 Pa).

However, more work is needed to determine the presence of hydrides at small fatigue crack-tips, if any. The surface crack path observations of a flatter crack, with less instances of well-defined cracking along crystallographic planes than observed for laboratory air and vacuum tests suggests a difference in crack-tip plasticity.

4.7.2 Estimation of Rate Controlling Process of Environmental Effect

Previous studies have examined the mechanisms of environmental effects leading to increased fatigue crack growth rates in ultrasonic fatigue [88, 113]. The rate-determining mechanism for these effects is often based on calculations of the time required for gas transport and chemical reactions to take place at the crack-tip compared to the time available, i.e. the loading period of the crack and average fatigue crack growth rate. This analysis is used here for the environmental effects on small fatigue cracks observed in the present study.

The mechanisms of the influence of gaseous hydrogen and water vapor were investigated for an aluminum alloy by Wei et al. [148, 149]. Titanium and aluminum are both highly reactive metals with similar atomic size. In the proposed model by Wei et al., the processes for increased fatigue crack growth rates in the presence of water vapor are described in three steps:

1. Water vapor molecules migrate to the crack-tip by impeded molecular transport, i.e. Knudsen flow [150];
2. Water molecules react with freshly formed titanium surfaces at the crack-tip. Hydrogen atoms form from the complete dissociation reaction of water molecules. Hydroxyl groups form from the partial dissociation reaction;
3. Hydrogen atoms diffuse from the crack surface to the crack-tip plastic zone, causing hydrogen assisted cracking.

These steps operate in sequence and the resulting crack growth rate is governed by the slowest process, or rate-limiting step. To determine the rate-limiting process the time needed for each step is estimated in the following.

Calculations assume the case of a 100 μm long (c = 50 μm) surface crack in a 133 Pa water vapor environment at a stress amplitude of 400 MPa at room temperature. The total volume of the Philips XL-30 ESEM chamber can be estimated assuming a cylindrical pressure vessel radius of 0.142 m and a height of 0.180 m yielding a total volume of approximately 0.0114 m^3.

In order to determine the number of water vapor molecules required to affect the crack growth on the next loading cycle the average fatigue crack growth rate (approximately 2 x 10^{-10} m/cycle) and the assumption of a uniformly advancing semi-circular crack front is used. The surface area is calculated to be about 1.6 x 10^{-8} m^2. The surface concentration of titanium can be estimated using Equation 4.3:

$$C_{Ti} = \frac{d\rho_{Ti}}{M_{Ti}} \tag{4.3}$$

where d is the a-type lattice constant of alpha aluminum (3 x 10^{-10} m), ρ_{Ti} is the density of titanium (4.5 x 10^6 g/m^3), and M_{Ti} is the atomic mass of titanium (48 g/mol). The surface concentration of titanium is estimated to be 2.8 x 10^{-5} mol/m^2. Assuming that all sites are available for the surface reaction of Ti with H_2O in a surface area of 1.6 x 10^{-8} m^2, the amount of water vapor molecules needed to migrate to the crack-tip by Knudsen flow to affect crack growth for the next loading cycle is estimated to be of the order 10^{-13} mol.

The time needed for 10^{-13} mol of water vapor molecules to migrate to the crack-tip by Knudsen flow can be estimated by Equation 4.4.

$$t_1 = \frac{N}{JA} = \frac{N}{\frac{P}{\sqrt{2\pi MRT}} 2c\frac{4\sigma c}{E}} = 8\,x\,10^{-2}\,sec \tag{4.4}$$

where N is the number of water vapor molecules (10^{-13} mol), J is the flux of water molecules through a fatigue crack in mol/(m^2-s), A is the area of the crack opening, P is the pressure of the water vapor, M is the molecular weight of water (18 g/mol), R is the gas constant, T is the temperature, c is the half crack length, σ is stress amplitude, and E is the Young's modulus (121 GPa).

The time needed for 10^{-13} mol of water molecules to react with the freshly formed crack surface can be calculated by Equation 4.5, assuming a first order reaction:

$$t_2 = -\frac{1}{4k_c}(\ln N_f - \ln N_o) = 6 \times 10^{-4}\ sec \tag{4.5}$$

where k_c is the reaction rate constant for water-titanium reaction (of the order 10^3 Pa^{-1} s^{-1}), N_f is the amount of the remaining water vapor molecules (assuming $N_f = 10^{-14}$ mol), N_0 is the original amount of the water vapor molecules (10^{-13} mol).

The final step, the time needed for hydrogen atoms to diffuse to the plastic zone, t_3, can be estimated by assuming that the hydrogen concentration profile ahead of the crack tip can be modeled by a steady-state diffusion in a semi-infinite body with a fixed concentration source. If the distance of diffusion exceeds the crack extension per cycle, then hydrogen assisted crack growth will occur for the next cycle. The time needed for diffusion is calculated by:

$$t_3 = \frac{1}{D}\left(\frac{dc/dN}{4}\right)^2 = 3 \times 10^{-6}\ sec \tag{4.6}$$

where D is the diffusion coefficient (1.0 x 10^{-15} m^2/s [151]) and dc/dN is the crack growth rate. The dc/dN term was assumed to be 2.0 x 10^{-10} m/cycle, which is the average fatigue crack growth rate from cracks grown in 133 Pa water vapor environments.

A comparison of t_1, t_2, and t_3 shows that the time needed for the transport of water molecules to the crack-tip is significantly longer than the time needed for the adsorption reaction or

subsequent hydrogen diffusion. Thus, gas transport to the crack-tip is likely the rate-limiting step. This is consistent with the results of [98]. It should be noted that the simplified model used here does not account for additional mechanisms such as pumping of species into the crack-tip by the opening and closing of the crack, as well as the many dependencies of gas adsorption mechanisms, such as microstructure, surface roughness, and surface composition. Therefore, more study is needed to pin down the processes active under ultrasonic fatigue and this is discussed in Chapter 6.

4.8 Summary and Conclusions

An *in situ* combined ultrasonic fatigue scanning electron microscope system (UF-SEM) for high resolution observations of fatigue damage accumulation and subsequent crack initiation and growth behavior was designed and built. The system was used in an investigation of the microstructural and environmental dependence of crack initiation and propagation from FIB micro-notches in Ti-6242S. In-SEM small fatigue crack growth behavior in vacuum, water vapor, oxygen, and hydrogen gas was compared to fatigue tests in laboratory air using a different ultrasonic fatigue instrument that operates using the same principles as the UF-SEM system.

A pronounced increase in small fatigue crack growth rate was observed in laboratory air compared to vacuum (2 – 3 orders of magnitude) at an ultrasonic frequency of 20 kHz. Fatigue crack growth rates also increased with increasing pressures of H_2O vapor, oxygen, and hydrogen gas. Additionally, at a P_{H2O} of 1330 Pa the FCGR was essentially the same as that observed in laboratory air of comparable humidity. Fatigue crack growth tests in H_2O and O_2 gas at equivalent pressures of 1330 Pa and 133 Pa showed higher FCGRs in water vapor than in oxygen as well. Based on these results, water vapor is determined to be more detrimental to fatigue crack

growth behavior than oxygen and hydrogen. Furthermore, water vapor is likely the main species responsible for higher crack growth rates in laboratory air compared to vacuum.

Cracks frequently decelerated or arrested at high angle α/α and $\alpha/\alpha+\beta$ grain boundaries, and demonstrated sensitivity to microstructure that has typically been observed in small crack growth behavior. Surface crack path observations also showed that crack propagation was increasingly crystallographic with increasing pressures of water vapor and oxygen. In vacuum and low pressure hydrogen environments, crack paths were flatter than in laboratory air and more difficult to classify in terms of correlation with specific crystallographic planes. Crystallographic crack growth has been correlated with smoother, faceted fracture surface features and higher crack growth rates in previous studies due to the greater severity of single slip at the crack-tip [78].

The findings presented in this dissertation are in agreement with these investigations. Specifically, laboratory air produced fracture surfaces had more faceted features compared to fracture surfaces generated in vacuum testing. Large areas of finer, ductile fracture were observed on fracture surfaces produced by crack growth in vacuum. The surface and fracture surface observations of cracks grown in vacuum, including crack growth on non-crystallographic planes, branching and reinitiating of cracks, and ductile fracture regions, suggests multiple slip systems are operative at the crack-tip. This indicates crack-tip blunting may be a significant process in vacuum testing.

Small fatigue crack growth rates in laboratory air and water vapor are caused by the adsorption of water vapor molecules on fresh crack surfaces, generation of an oxide/hydroxide layer that impedes reverse slip, and hydrogen assisted cracking. Similarly, the cause of increased small fatigue crack growth rates in oxygen is suggested to be the fast adsorption of oxygen atoms

on fresh crack surfaces near the crack-tip, and subsequent formation of an oxide layer that impedes reverse slip of slip planes during the unloading portion of the fatigue cycle. The key difference in the processes governing increased FCGR in oxygen compared to water vapor is the absence of a hydrogen assisted cracking mechanism in oxygen. Finally, for the low pressures of hydrogen gas studied under ultrasonic fatigue loading, hydrogen enhanced local plasticity at the crack-tip is likely responsible for increased FCGR in hydrogen compared to vacuum.

CHAPTER 5

EXAMINING MICROSTRUCTURAL AND ENVIRONMENTAL INFLUENCES ON FATIGUE CRACK INITIATION IN VERY HIGH CYCLE FATIGUE OF TI-6242S

In Chapter 4, the processes related to microstructural and environmental effects on small fatigue crack growth from FIB-machined micro-notches were described. It was evident that both the local surface microstructure of the FIB notch and the surrounding environment played a significant role in the time needed to initiate a small crack. Crack initiation from FIB notches located in favorably oriented grains in vacuum was delayed compared to laboratory air, where favorably oriented grains were determined to be α_p grains with a high basal Schmid factor. Although the study of the mechanisms of fatigue crack initiation and growth from notches and other defects remains critical to fatigue life prediction, it is also important to study natural crack initiation as a function of local microstructure. The study of natural fatigue crack initiation may also help to develop better insight into the role of environment on small crack growth behavior, especially as it relates to the rate of damage accumulation and strain localization processes.

This chapter presents the results of an investigation into the mechanisms of natural fatigue crack initiation in the very high cycle fatigue regime in Ti-6242S in laboratory air and vacuum. In the context of this work, natural initiation signifies the initiation of surface fatigue cracks without the presence of notches or other geometric discontinuities. The main objective of this portion of the study was to determine if fatigue crack initiation mechanisms in laboratory air differed from those in vacuum, and if so, to propose a process for this behavior.

An additional question under investigation was whether the observed difference in fatigue life for laboratory air versus vacuum testing, in this work and others, is attributed mainly to differences in initiation behavior, growth behavior, or both.

Section 5.1 discusses the results of fatigue lifetime experiments carried out in laboratory air and vacuum. Section 5.2 describes the locations, in terms of microstructure and microstructure neighborhoods, of crack initiation in specimens fatigued in these two environments. Fracture surface observations are discussed in Section 5.3. The details surrounding the different types of fatigue crack initiation mechanisms observed in this material are explained in Section 5.4. Finally, Section 5.5 summarizes findings pertaining to fatigue crack initiation in Ti-6242S in the VHCF regime.

5.1 Fatigue Lifetime

Fatigue failure lifetimes from ultrasonic fatigue testing in laboratory air and vacuum (1.7 x 10^{-4} Pa) ranged from 10^5 to 10^8 cycles, as shown in Figure 5.1. A comparison of fatigue lifetimes in laboratory and vacuum showed that fatigue lifetimes were shorter in laboratory air. Fatigue failures in the range of $10^7 – 10^9$ cycles were infrequent and fatigue specimens tended to survive until runout, defined as 1 x 10^9 cycles, or failed at shorter lifetimes, less than 10^7 cycles.

Fatigue cycling in vacuum experiments was paused and SEM images of the specimen surface were captured at different numbers of cycles. This enabled estimation of the initiation lifetime for nascent (nonfatal) and fatal cracks. To search for nascent cracks, high resolution images of the specimen flats were captured using the SEM in backscattered electron (BSE) mode. The enhanced contrast of BSE images enabled manual identification of nascent cracks as short as approximately 5 μm in a 2.75 x 2.75 mm^2 field of view as shown in Figure 5.2. However, this procedure was not done for laboratory air testing, so comparisons of crack initiation lifetime are

described using the failure lifetime in the case of laboratory air. Nascent cracks were detected as early as 10^6 cycles in vacuum for a stress amplitude of 450 MPa. A nascent crack also initiated before 2.5 x 10^7 cycles in a fatigue specimen that survived until a runout of 10^8 cycles in vacuum at σ_a = 450 MPa. In general, a longer fatigue life correlated with the presence of more nascent cracks on the specimen surface in both laboratory air and vacuum.

Fatigue life data for three specimens that were initially fatigued in vacuum for approximately 10^8 cycles and then cycled in laboratory air until failure are shown in Figure 5.1. Interestingly, the number of cycles to failure in laboratory air after vacuum testing for these specimens was similar to the failure lifetimes of specimens fatigued only in laboratory air. Surface observations showed that two of the three specimens failed from newly initiated cracks in laboratory air, despite the confirmed presence of pre-existing nascent cracks from cycling in vacuum, as many as 11 in one specimen. None of the vacuum initiated nascent cracks propagated during cycling in laboratory air. The third sample failed on the (unmonitored) curved region of the fatigue specimen, thus it was unknown whether this sample failed from a preexisting nascent crack or a crack initiated in laboratory air.

Direct integration of the Paris law enables estimation of the number of cycles (N_f) for growth of an initial crack size (a_o) to a final crack length (a_f) as shown in Equation 5.1. The dimensionless factor F was set to 1. The Paris law parameters C and m were determined for small cracks grown from FIB micro-notches in laboratory air and vacuum as discussed in Section 4.3. Using an a_o of 13 μm, which is approximately equal to the average α_p grain size, and an a_f of 2 mm, the approximate radius of the fracture region at specimen failure, the fatigue lifetime in air and vacuum at $\Delta\sigma$ = 400 MPa is calculated to be 2.7 x 10^5 cycles and 1.2 x 10^8 cycles, respectively. In comparison, the minimum fatigue lifetime measured for a specimen failed in

laboratory air only was 5 X 10^5 cycles at σ_a = 400 MPa and only one sample failed before 10^8 cycles in vacuum at this same stress. This suggests the number of cycles needed to initiate a crack takes up a significant portion of fatigue lifetime.

$$N_f = \frac{2}{(m-2)CF^m\Delta\sigma^m\pi^{m/2}}\left[\frac{1}{a_o^{(m-2)/2}} - \frac{1}{a_f^{(m-2)/2}}\right] \quad (5.1)$$

Fatal cracks initiated from surface locations only in both environments. This is different from the fatigue behavior of a Ti-6246 alloy tested at 20 kHz, as studied by Szczepanski and coworkers that exhibited fatigue crack initiation from both surface and subsurface locations [11]. The findings regarding the microstructural characterization of crack initiation locations investigated in the present study are discussed in the next section.

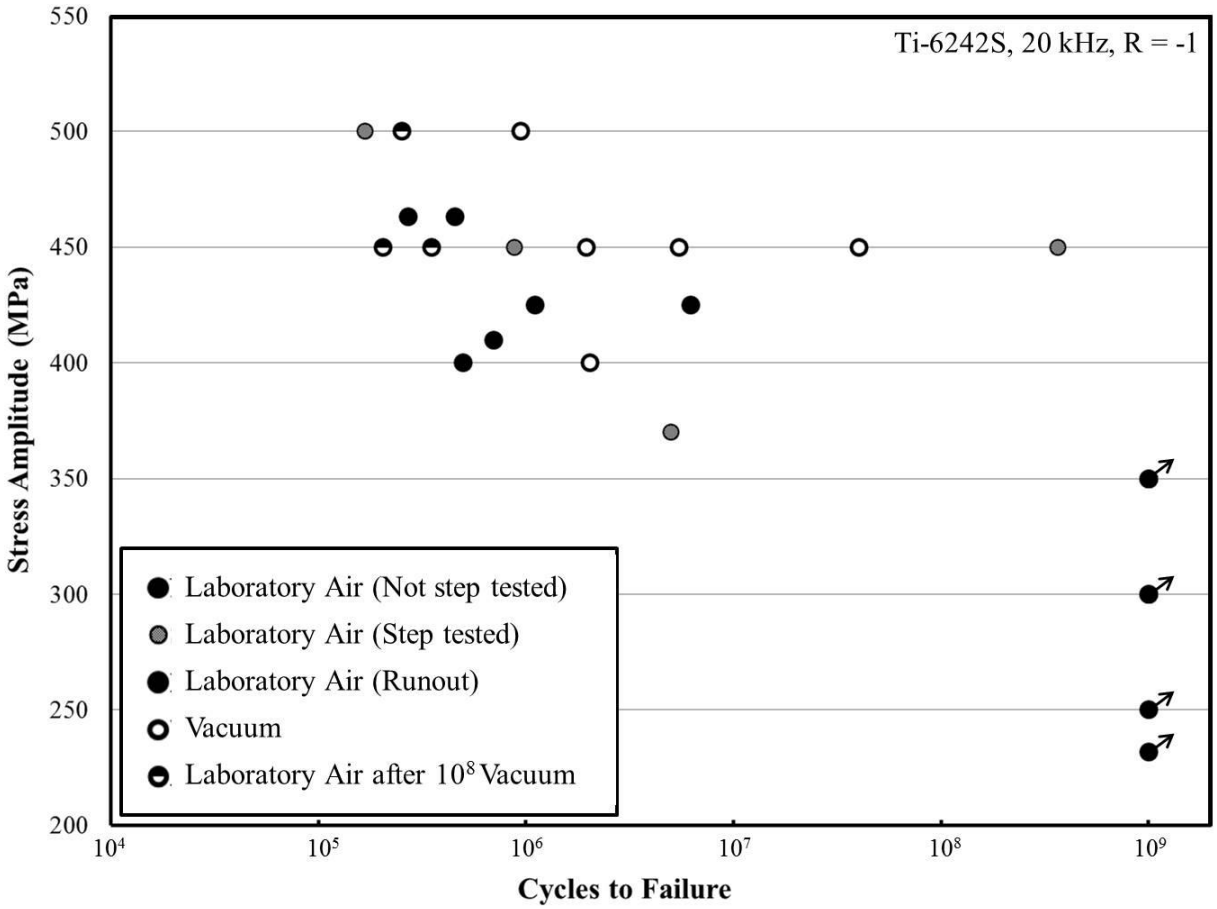

Figure 5.1: Fatigue lifetime behavior of Ti-6242S tested in both laboratory air and vacuum with step test runouts and final failures. In general, fatigue lifetimes were shorter in air than in vacuum. The failure lifetimes of three specimens that were cycled in vacuum for 10^8 cycles at 450 MPa, followed by cycling in air until failure are also shown. The failure lifetimes of these samples are similar to the failure lifetimes of virgin samples failed in laboratory air.

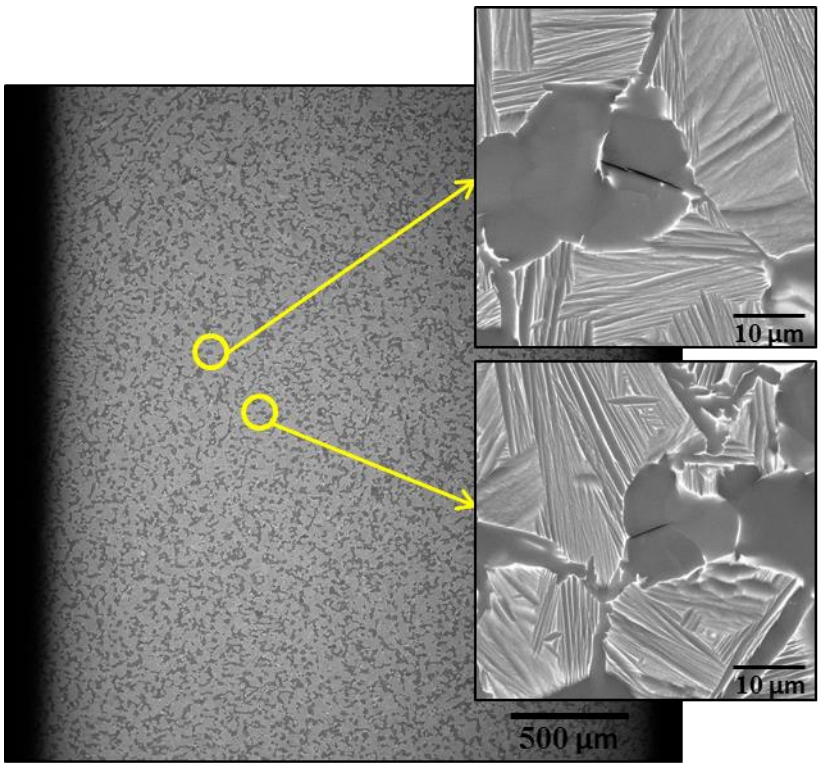

Figure 5.2: A 2.75 x 2.75 mm^2 backscattered electron micrograph of a portion of a fatigue specimen gage section after 2.5 x 10^7 cycles in vacuum at σ_a = 450 MPa is shown. Four images were captured along the flat gage section on both sides of the specimen at various numbers of cycles in order to check for the initiation of fatigue cracks, such as the two shown in the magnified images at right.

5.2 Crack Initiation Locations

Fatal fatigue cracks initiated from surface locations only in vacuum and laboratory air, as confirmed by both surface and fractographic analysis. Fatal and nascent cracks initiated on both the curved and flat surfaces of the gage region of the fatigue specimens. OIM analysis was used to characterize the local microstructure of fatigue crack initiation sites in the cases where cracks initiated on the specimen flats. This is discussed in detail in Section 5.4.

Most fatigue specimens had a single fatal crack and one to several non-fatal, nascent cracks; the number of nascent cracks increased with increasing numbers of cycles as indicated in Table 5.1. Greater numbers of nascent cracks were identified in vacuum tests, which had longer fatigue

lifetimes than laboratory air tests. An example of these nascent cracks is shown in Figure 5.3. Figure 5.3 also shows that nascent cracks produced extruded material in a similar manner to that observed for small fatigue cracks grown from FIB micro-notches (Section 4.6.3).

The majority of nascent cracks in vacuum and air occurred parallel to and at/near grain boundaries between two α_p grains (Type #1). However, fatal and nascent fatigue cracks also initiated within α_p grains (Type #2). Schematics of Type #1 and Type #2 cracks are shown in Figures 5.8. No initiation sites were found within the transformed β regions. This is in agreement with numerous studies that investigated fatigue crack initiation in near α and $\alpha + \beta$ titanium alloys at low stress amplitudes [27].

Nascent cracks that initiated in vacuum often did not propagate or, if they did, they extended only a small distance into neighboring regions as shown in Figure 5.4(a). In fact, nascent cracks in vacuum typically spanned one α_p grain at most, with the longest observed to be 16 μm and spanning two α_p grains. However, nascent cracks formed in laboratory air would frequently propagate into neighboring grains as shown in Figure 5.4(b), and several cracks spanned 2-3 grains, even though shorter fatigue lives were observed in the air tests. In some cases nascent cracks initiated in laboratory air were much longer, with the longest measuring approximately 450 μm and spanning more than 25 grains. Additionally, a histogram of the distribution of the lengths of nascent cracks (Figure 5.5) shows that nascent cracks in vacuum were typically shorter than nascent cracks in air. The average length of nascent cracks in vacuum and laboratory air was 8.5 ± 3.1 μm and 13.0 ± 7.8 μm, respectively. These dimensions are similar to the average grain size of the α_p phase (≈ 12 μm), also indicating these microstructural features are the critical features for fatigue crack initiation.

Table 5.1: Summary of the number of nascent cracks observed on flat fatigue specimen surfaces

Specimen No.	Environment	Stress Amplitude (MPa)	N_f	# of Nascent Cracks
1	Vacuum	400	5.5×10^7	4
2*	Vacuum	450	1.0×10^8	11
3*	Vacuum	450	1.0×10^8	7
4	Vacuum	500	5.3×10^7	5
5	Lab Air	425	6.2×10^6	1
6**	Lab Air	425	1.1×10^6	2
7**	Lab Air	450	8.7×10^5	3
8**	Lab Air	450	3.7×10^8	11
9	Lab Air	500	1.0×10^6	3

* Specimen was fatigued in laboratory air until failure after 10^8 cycles in vacuum. The number of nascent cracks shown was measured after vacuum cycling

**Specimen was cycled at lower stresses until runout, and nascent cracks may have been initiated during this portion of the fatigue life. N_f represents the failure life at the maximum σ_a indicated.

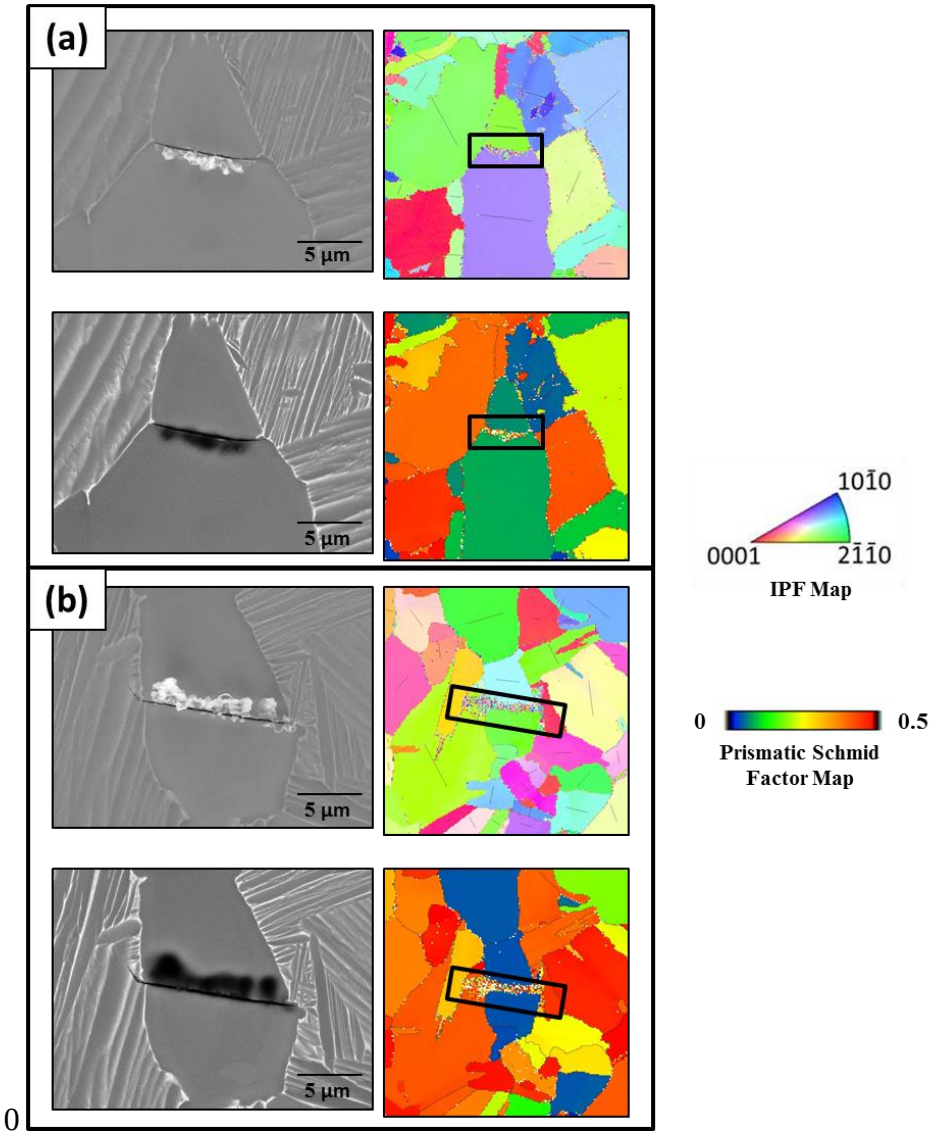

Figure 5.3: Two examples of nascent cracks initiated in a fatigue specimen tested at σ_a = 450 MPa in vacuum. Corresponding OIM maps of the local grain orientation and prismatic Schmid factor are also provided. The extruded material at the crack was also observed in small crack growth from FIB notches and is discussed in Section 4.6.3.

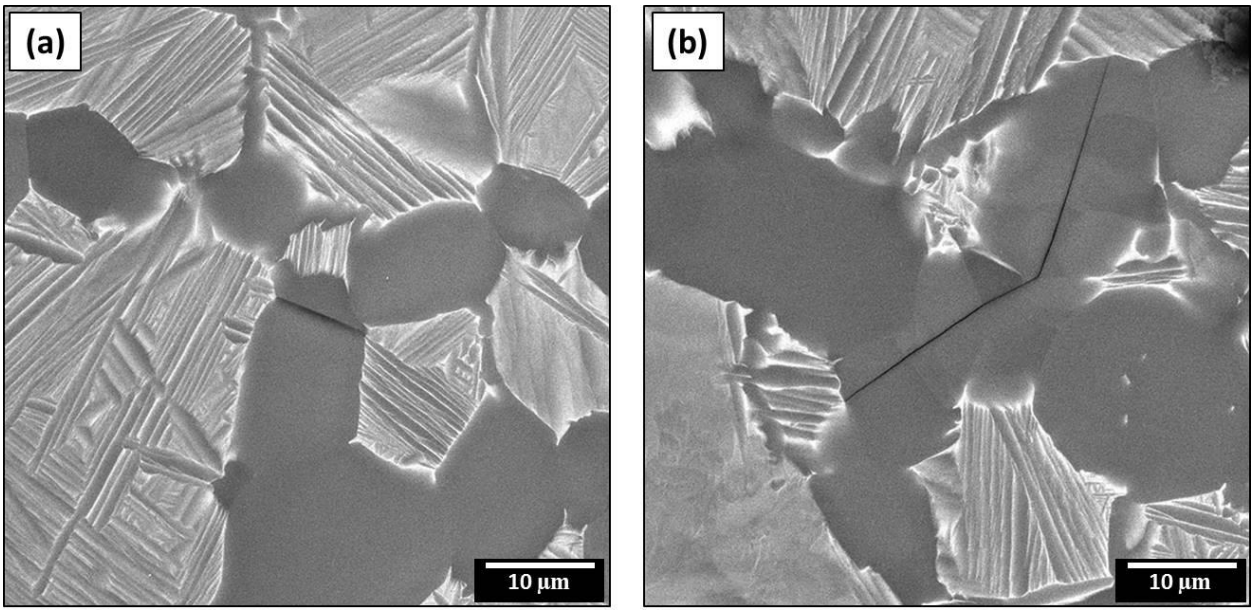

Figure 5.4: Examples of nascent cracks initiated in vacuum (a) and laboratory air (b) are shown. Nascent cracks in vacuum typically spanned one α_p grain, while nascent cracks formed in laboratory air would frequently propagate into neighboring grains.

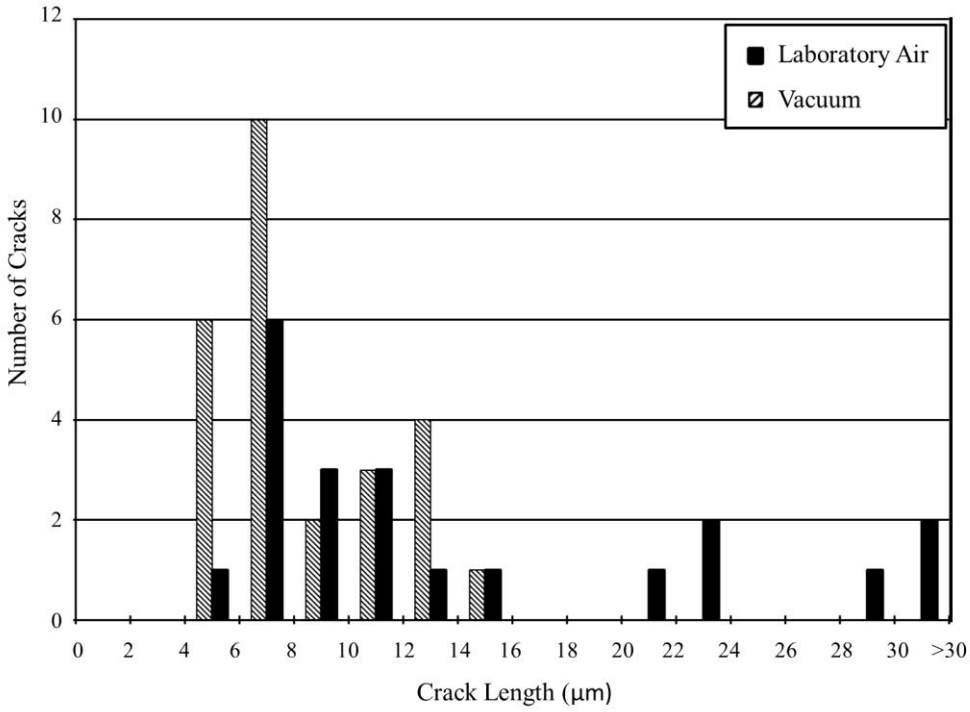

Figure 5.5: A histogram of the length of nascent cracks initiated in laboratory air and vacuum is shown. The average length of nascent cracks in vacuum and laboratory air was 8.5 ± 3.1 µm and 13.0 ± 7.8 µm, respectively.

5.3 Fractographic Analysis

Figure 5.6 shows a representative fracture surface for a fatal crack grown during ultrasonic fatigue testing in laboratory air. Fractographs of the specified regions are also shown indicating the fracture surface morphology at different stages of crack growth. The region of fatigue crack initiation was determined using the river like markings that "point" to the crack initiation site that can be seen in the low magnification image of the entire fracture surface in Figure 5.6. In this example, the fatigue crack initiated from the highlighted α_p grain facet as determined by visual inspection of the fracture surface and adjacent surface OIM analysis. A higher magnification image of the faceted α_p grain where the fatigue crack is determined to have initiated is shown in Figure 5.6(A). Facets of one or multiple grains could be identified at the fatigue crack initiation site on the fracture surface of all specimens failed in both laboratory air and vacuum.

A comparison of fatigue crack initiation regions in specimens failed in laboratory air and vacuum is shown in Figure 5.7, where no significant difference in appearance of the faceted grain of crack initiation was observed. However, the features in the early crack growth regions differed between the two environments. Smooth facet-like features were seen in both the vacuum and laboratory air fracture surfaces, but rougher, small-scale ductile fracture regions were only observed on fracture surfaces of specimens tested in vacuum. This is in agreement with fracture surface observations of faceted grains in the early crack growth region of specimens fatigued in laboratory air and vacuum discussed in Section 4.6. In Section 4.6, smoother, faceted regions occurred in laboratory air and significant areas of finer, ductile fracture features occurred in vacuum.

Faceted fracture was observed predominantly in the fatigue crack initiation region, with the frequency of facets decreasing with increasing crack length. The difference in the occurrence of facets between the two environments is consistent with the observation that crack growth rates in air were faster than crack growth rates in vacuum observed in Chapter 4, and that faceted fracture has been linked to higher crack growth rates [110, 152].

The angle between the facet plane normal and the loading axis was measured using quantitative tilt fractography, which involves capturing images of the fracture facets at two different angles to determine their inclination. No difference in the facet plane orientation of the α_p grain where fatigue crack initiation took place with respect to the loading direction was observed between the laboratory air and vacuum environments. The average orientation of the facet plane normal to the loading axis was approximately 35° in laboratory air and vacuum. The facet plane orientation of subsurface facets within the region of fatigue crack initiation was not measured.

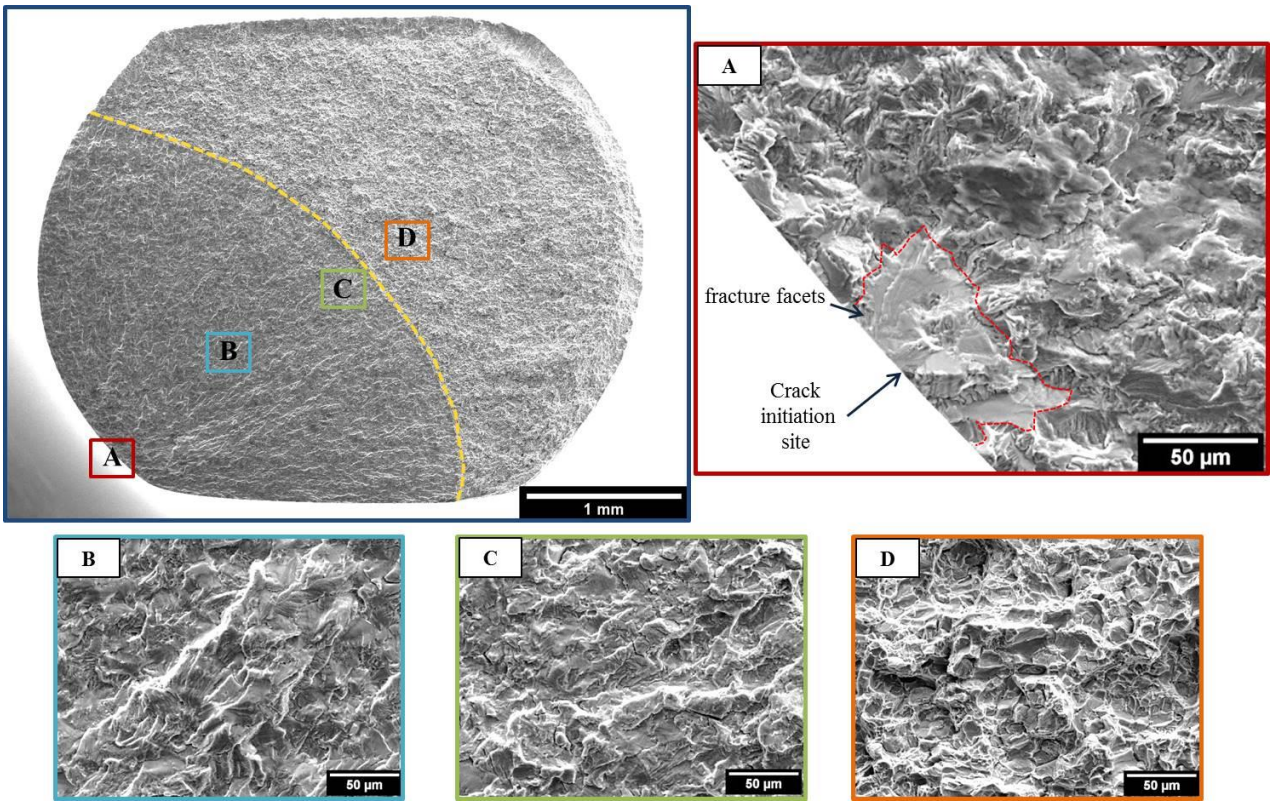

Figure 5.6: Fracture surface of fatigue specimen failed in laboratory air, σ_a = 425 MPa, N_f = 6.24 x 10^6 cycles. Higher magnification images of the fatigue crack initiation site (A) and other fracture surface regions B and C at various crack lengths are shown. The fracture surface created by breaking the specimen in half after the fatigue test was stopped is shown in D.

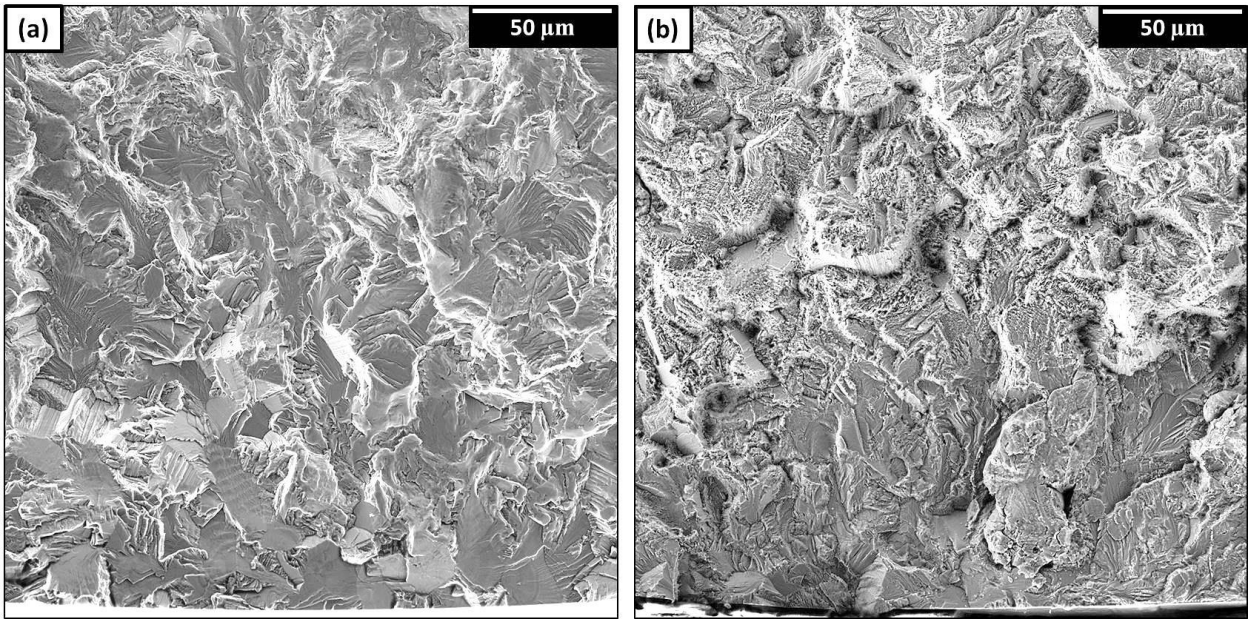

Figure 5.7: Examples of fracture surfaces produced by fatigue in (a) laboratory air and (b) vacuum are shown. Smooth facet-like features were seen in both the vacuum and laboratory air fracture surfaces, but rougher, small-scale ductile fracture regions were only observed on fracture surfaces of specimens tested in vacuum.

5.4 Types of Fatigue Crack Initiation

In general, two types of fatigue crack initiation modes were observed in the present study. In this section, the terms "hard grain" and "soft grain" are used extensively to describe the characteristics of favorable neighborhoods for crack initiation. These terms are used frequently in the literature to describe fatigue crack initiation and fracture mechanisms, but how they are defined may differ. In the present work, the term 'hard grain' will refer to any grain that is unfavorably oriented for prismatic slip; specifically, when the prismatic Schmid factor (μ) was less than 0.25. No such requirement was used for the basal or pyramidal Schmid factors, due to their higher CRSS values compared to prismatic slip [36]. Indeed, grains leading to Type #1 crack initiation were often unfavorably oriented for prism slip, but well-oriented for basal slip. The term 'soft grain' will refer to a grain with a prismatic Schmid factor in the range of 0.25 to 0.50. It is recognized that Schmid factor may be only one of several criteria needed to fully

describe fatigue crack initiation processes, and that surface analysis in general may be insufficient. However, in the present work, Schmid factor analysis in combination with surface neighborhood characteristics were shown to be useful in determining favorable sites for crack initiation. The types of fatigue cracks that were initiated can be described as follows:

1. Type #1: Cracks initiated parallel to and at or near a low misorientation grain boundary between two similarly oriented α_p grains. The two α_p grains can be classified as hard compared to neighboring region, which can be described as soft. The grain boundary between these grains typically has a low misorientation (< 30°).
2. Type #2: Cracks initiated from a high misorientation grain boundary between two grains. One grain can be classified as hard and the other grain as soft. The hard grain where the crack is initiated is a primary alpha grain and the soft grain can be either an α_p or $\alpha + \beta$ grain. OIM analysis shows that the cracks initiated on or near the basal plane of the α_p grain.

A schematic of both types of fatigue cracks is shown in Figure 5.8. The frequency of each type of crack is summarized in Table 5.2. Type #1 fatigue cracks were the most frequently observed for both environments. No nascent cracks that could be categorized as Type #2 were detected on the flat surfaces of laboratory air specimens. Four of the 25 nascent cracks initiated in vacuum were determined to be Type #2. In a limited number of instances, the nascent or fatal crack could not be categorized as either Type #1 or Type #2. A more detailed discussion of fatigue crack initiation mechanisms is provided in the following sections.

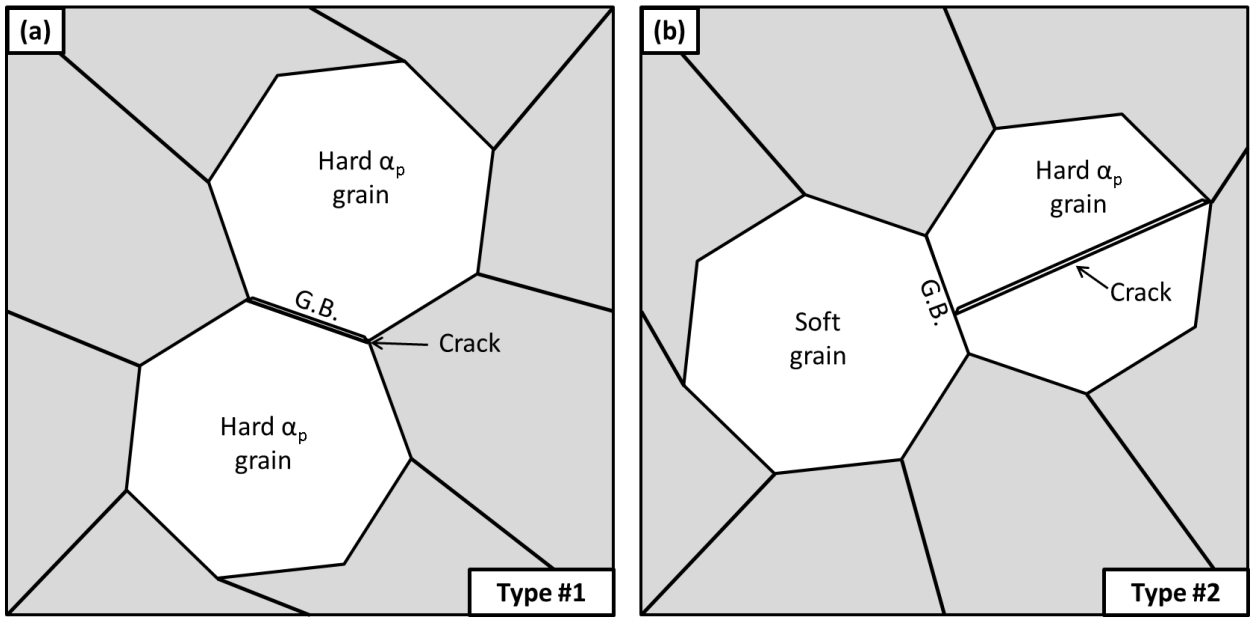

Figure 5.8: A schematic of (a) Type #1 and (b) Type #2 fatigue crack initiation processes. Type #1 fatigue cracks were the most frequently observed for both environments.

Table 5.2: Summary of fatigue crack initiation mechanisms observed in fatigue specimens failed in laboratory air and vacuum

	Laboratory Air	**Vacuum**
Fatal Cracks	2	2
Type #1 (Fatal)	1	2
Type #2 (Fatal)	1	0
Nascent Cracks	20	25
Type #1 (Nascent)	18	21
Type #2 (Nascent)	0	4
Not Classified	2	0
Total Cracks	22	27

5.4.1 Type #1: Fatigue Crack Initiation Along Low Misorientation Grain Boundaries

A representative example of Type #1 fatigue crack initiation is shown in Figure 5.9. Grain A and Grain B were two hard α_p grains that initiated a fatigue crack at their shared grain boundary. The basal Schmid factors for Grain A and Grain B were 0.28 and 0.26, respectively. The maximum prismatic Schmid factor for Grain A and Grain B was 0.04. The two grains shared a low misorientation grain boundary that was misoriented by approximately 13°. The surrounding microstructure consisted of numerous grains, both α_p and lamellar $\alpha + \beta$, that had soft orientations. All near neighbor grains had maximum prismatic Schmid factors above 0.25.

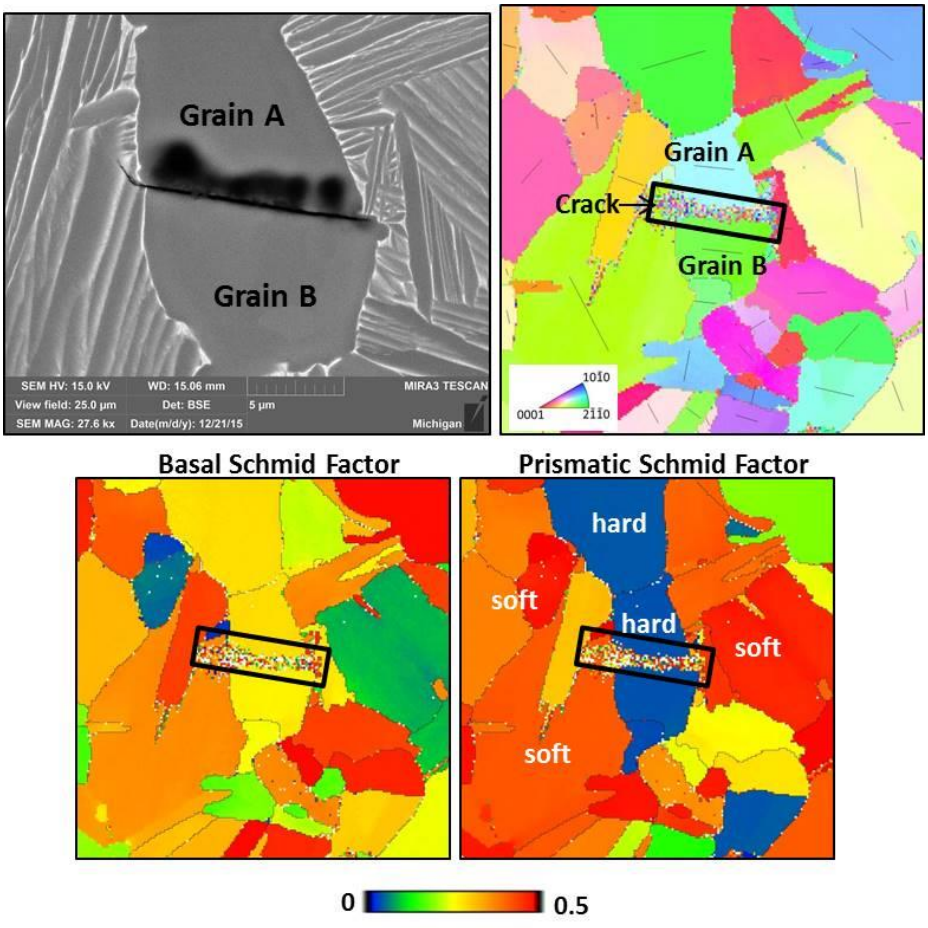

Figure 5.9: An example of a Type #1 nascent fatigue crack initiated in vacuum is shown. Grain A and Grain B initiated a crack at their low misorientation grain boundary of approximately 13°. Basal and prismatic Schmid factor maps of the microstructural neighborhood are also shown. The two α_p grains can be classified as hard compared to the surrounding soft microstructure.

No significant difference in the orientations of grains exhibiting Type #1 crack initiation behavior was observed between cracks initiated in laboratory air and vacuum. Because the grains across the grain boundary where crack initiation occurred were similarly oriented only the orientation of one of the α_p grains was used in the following analysis. Figure 5.10 shows an IPF map of the grain orientations associated with Type #1 initiation in both laboratory air and vacuum. There is little difference in the orientations of these grains for either environment. Figure 5.11 shows the distributions of the basal, prismatic, and pyramidal (a-type) Schmid factors for these same grains for both laboratory air and vacuum. The distribution of the angle of the basal plane normal with respect to the loading axis is also plotted in Figure 5.12. In laboratory air, the basal Schmid factor was in the range of 0.27 – 0.50 and in vacuum the range was 0.28 – 0.50. The prismatic Schmid factor was in the range 0.05 – 0.33 in laboratory air and 0.04 – 0.34 in vacuum. There were some instances in laboratory air and vacuum where the prismatic Schmid factor of the hard grains was greater than 0.25. However, the value never exceeded 0.35 in either environment and a softer neighborhood region may offset this moderate increase in prismatic Schmid factor. Lastly, the moderate to high basal Schmid factor range is consistent with the observations of faceted fatigue crack initiation along basal planes on fracture surfaces from fatal cracks initiated by the Type #1 mechanism. This suggests that basal slip in the hard grains may precede faceted fatigue crack nucleation.

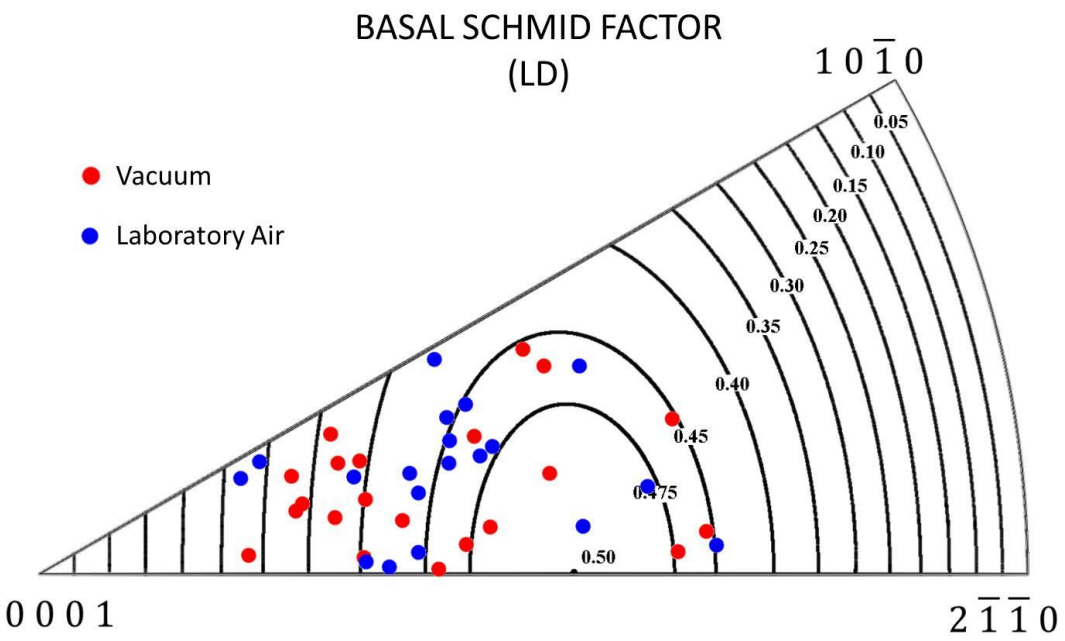

Figure 5.10: An IPF map of the orientations of grains leading to Type #1 fatigue cracks in laboratory air and vacuum testing. Iso-curves of the basal Schmid factor are also plotted. The orientations of grains were similar in laboratory air and vacuum, with basal Schmid factors ranging from 0.27 to 0.50.

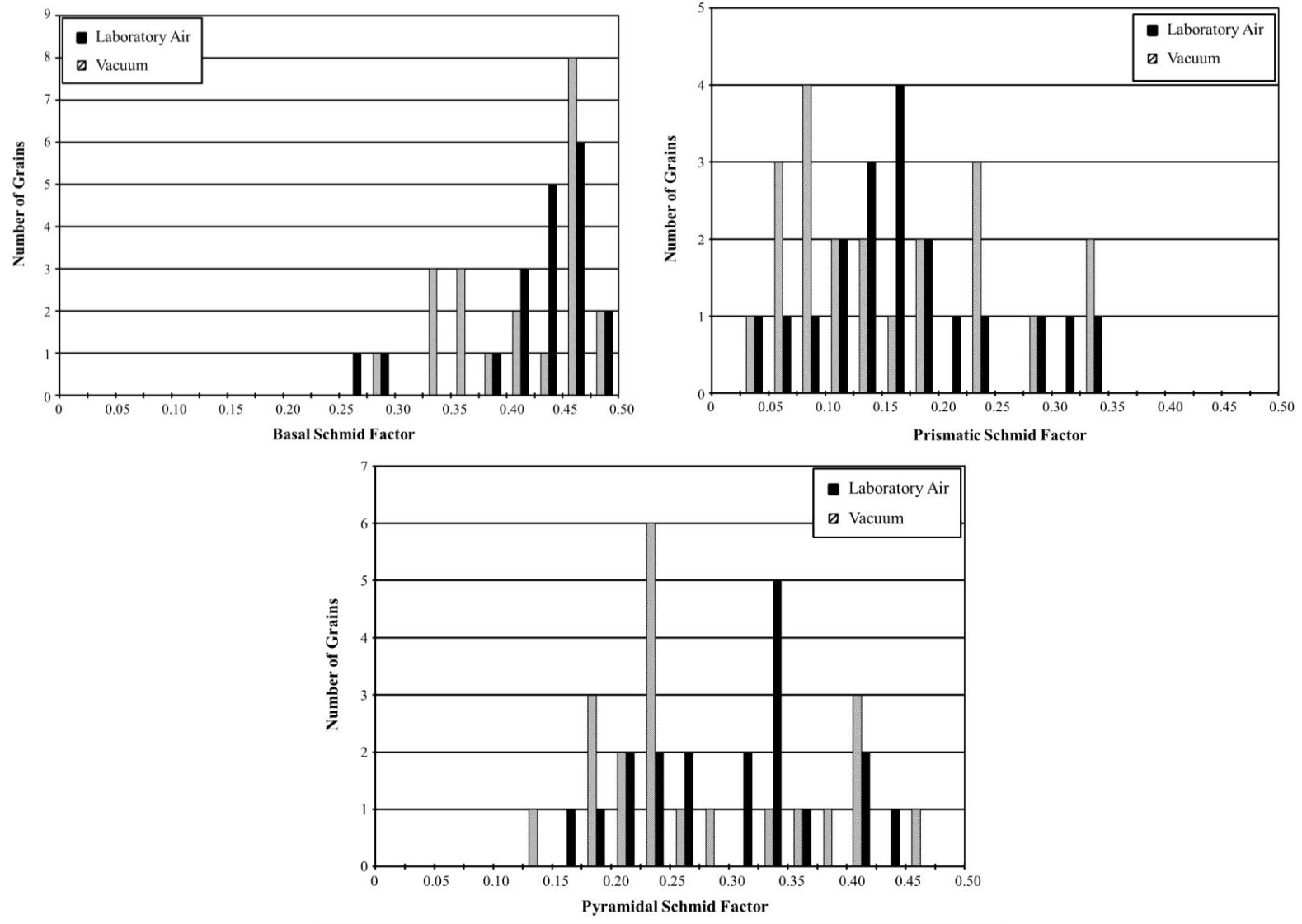

Figure 5.11: Distributions of basal, prismatic, and pyramidal Schmid factors of α_p grains leading to Type #1 fatigue cracks. No significant differences in range or distribution are observed for cracks initiated in vacuum compared to laboratory air.

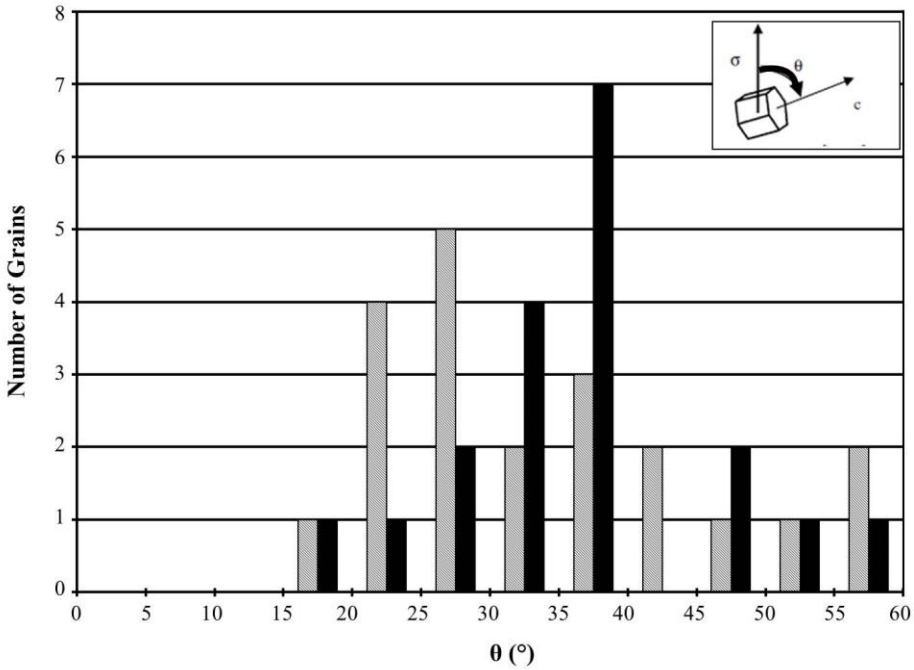

Figure 5.12: A distribution of the angle between the basal plane normal and the loading axis (θ) is shown for grains where Type #1 cracks initiated. The average angle in laboratory air was approximately 36° and the average angle in vacuum was approximately 34°.

The mechanism responsible for the initiation of Type #1 fatigue cracks is proposed to be an increase of stress in the two similarly oriented hard α_p grains by load shedding of the soft surrounding microstructure. Fatigue cycling causes local strain accumulation in the weak surrounding microstructure that is favorable for dislocation slip. After a critical level of deformation – wherein the weak neighborhood is unable to sustain the local and far-field applied nominal stresses – is attained, load shedding from the weak neighborhood occurs and the stress is increased in the hard α_p grain pair. It is possible that dislocation pileups at the grain boundaries between the hard α_p grains and the soft neighborhood may also play an important role. The dislocation pileups that result from persistent, planar slip in the soft grains may impinge on the hard α_p grains, causing both a local shear and/or normal stress to develop. The low misorientation grain boundary acts as a defect for the subsequent fatigue crack initiation that

occurs as a result of the combination of the applied stress and the normal stress developed from dislocation pileups. TEM imaging of the dislocation structures developed in the hard and soft grains is needed to confirm the proposed mechanism for Type #1 crack initiation.

5.4.2 Type #2: Fatigue Crack Initiation by Stroh Mechanism

Type #2 surface fatigue crack initiation is characterized by crack initiation from a high misorientation angle grain boundary between a hard and soft grain. This type of fatigue crack was observed in both laboratory air and vacuum, but was much less frequent than Type #1 cracks. An example of a Type #2 fatigue crack is shown in Figure 5.13. The crack is initiated at the boundary between Grain A and Grain B. Grain A, the soft grain, had a maximum basal and prismatic Schmid factor of 0.42 and 0.37, respectively. A prismatic slip band within Grain A can also be seen. Grain B, the hard grain, had a maximum basal and prismatic Schmid factor of 0.40 and 0.10, respectively. The crack was initiated along the basal plane trace of the hard α_p grain. It is likely that the crack was initiated on a basal plane, but subsurface analysis is needed to confirm if this was the case.

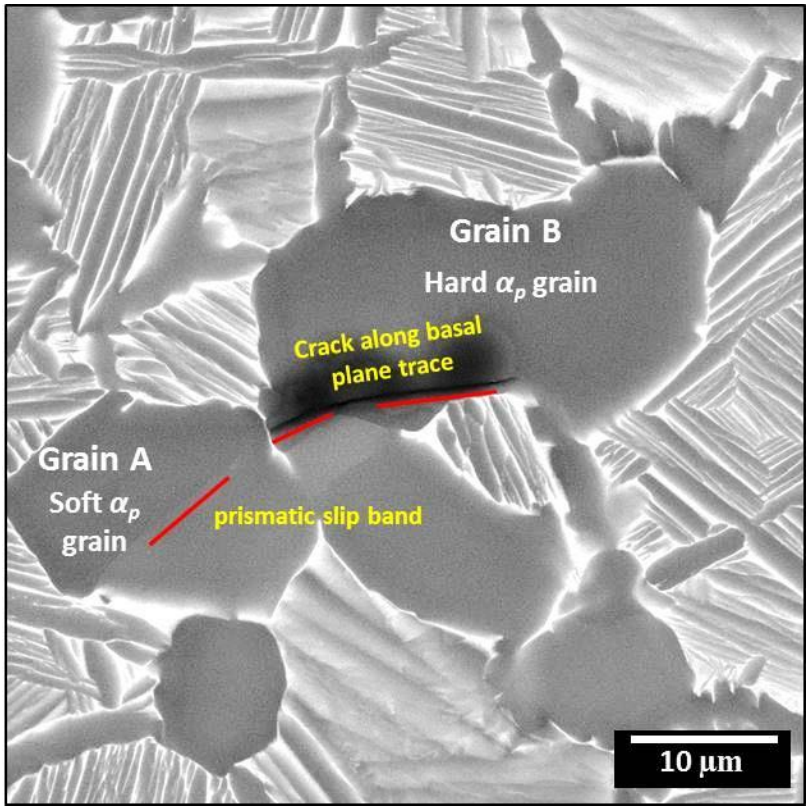

Figure 5.13: An example of a nascent crack that initiated from a high misorientation grain boundary (65°) between a soft (Grain A) and hard (Grain B) α_p grain. The crack was likely initiated on or near the basal plane Grain B. A slip band parallel to the prismatic plane trace of the soft grain is also visible.

Five examples of the Type #2 fatigue crack initiation mechanism were analyzed, with four being produced in vacuum and one in laboratory air. An IPF map showing the orientations of the hard and soft α_p grains that led to Type #2 cracks in vacuum tests is shown in Figure 5.14. The basal Schmid factors for the soft and hard grains were in the range of 0.07 – 0.42 and 0.22 – 0.46, respectively. Soft grains had a prismatic Schmid factor in the range of 0.37 – 0.50 and hard grains had a prismatic Schmid factor in the range of 0.03 – 0.13. The misorientation of the boundary between the two grains was approximately 65° - 88° (wherein the high misorientation is a consequence of the hard/soft grain character).

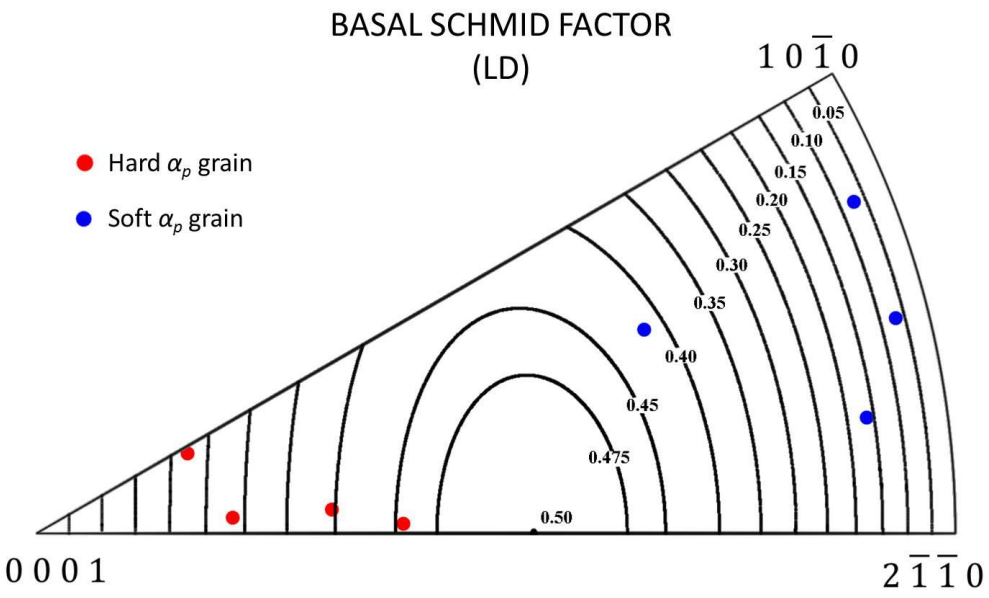

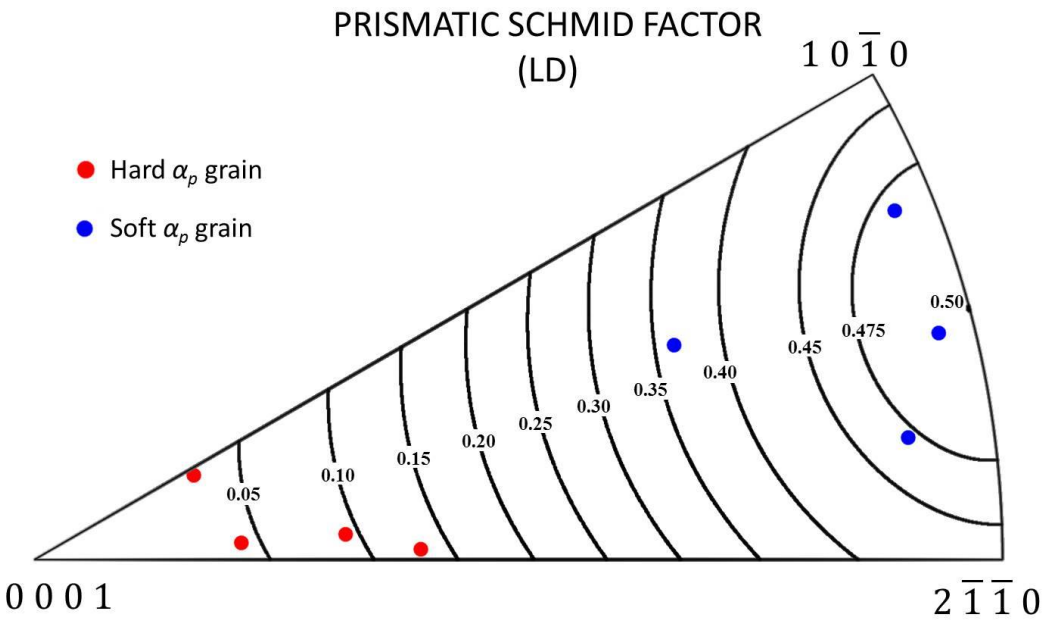

Figure 5.14: IPF maps showing the orientations of the hard and soft α_p grains that led to Type #2 cracks being initiated in vacuum tests. The hard grain had a low prismatic Schmid factor and moderate to high basal Schmid factor simultaneously. The soft grain had a high prismatic Schmid factor and a low to moderate basal Schmid factor. A prismatic slip band, consistent with the modified Stroh mechanism, was also produced within the soft grain, as shown.

The mechanism for Type #2 fatigue crack initiation is likely due to strain incompatibility at the high misorientation grain boundary between the hard and soft grains. This can be explained using the modified Stroh model first proposed by Neal and Blenkinsop [54] to explain fatigue cracks that initiated from α grains and colonies in which the basal plane was oriented normal to the loading axis. Evans and Bache [51] also proposed a modified Stroh model to explain fatigue crack initiation in $\alpha + \beta$ titanium alloys as a function of stress redistribution in the material due to grain orientations with respect to the loading direction. They proposed that at low stresses soft grains having slip planes that are favorably oriented for dislocation slip would accumulate strain more rapidly than their hard grain counterparts. This strain localizes in the form of a slip band in the soft grain that is blocked by the grain boundary causing a dislocation pileup to form at the grain boundary. The dislocation pileup induces a normal and shear stress on the basal plane of the adjacent hard grain. The local shear stress causes slip on the basal plane of the hard grain and the local normal stress combines with the nominal applied stress to cause a crack to initiate on or near the basal plane. This mechanism for crack initiation is useful in explaining the experimental observations of the present study. Indeed, a prismatic slip band in Grain A (soft grain) that has impinged on the high misorientation grain boundary that separates Grain B (hard grain) can be seen in Figure 5.13. It is likely that this slip band preceded crack formation in Grain B, and it was this deformation combined with the strain incompatibility between the two grains that led to the subsequent crack initiation along the basal plane of Grain B.

A combination of scanning electron microscopy and digital image correlation techniques (SEM-DIC) were employed to develop a better understanding of fatigue crack initiation mechanisms in VHCF. SEM- DIC is a non-contact, deformation tracking technique that enables full-field mapping of surface displacements, and thereby strains, at the micro-scale. More

information regarding the technique can be found in [153]. Fatigue specimens were patterned using the procedure described in [154] and ultrasonic fatigue tests were performed in vacuum using the UF-SEM system. Figure 5.15 shows an example of a full-field strain map around a nascent crack initiated in vacuum that was captured at $N = 2 \times 10^6$ cycles. The strain map was captured when the specimen was unloaded. Thus, only the accumulated plastic deformation is depicted. The grain boundaries are shown in black. The nascent crack that was initiated was categorized as a Type #2 crack. As seen in Figure 5.15, the hard grain, Grain B, had a much lower degree of deformation in the axial, or ε_{yy} , direction than the surrounding microstructure. However, Grain B developed a much higher shear strain, ε_{xy} , than the soft grain, Grain A, and the surrounding microstructure. This result is in agreement with the proposed Stroh mechanism explanation for Type #2 fatigue crack initiation between a hard and soft grain.

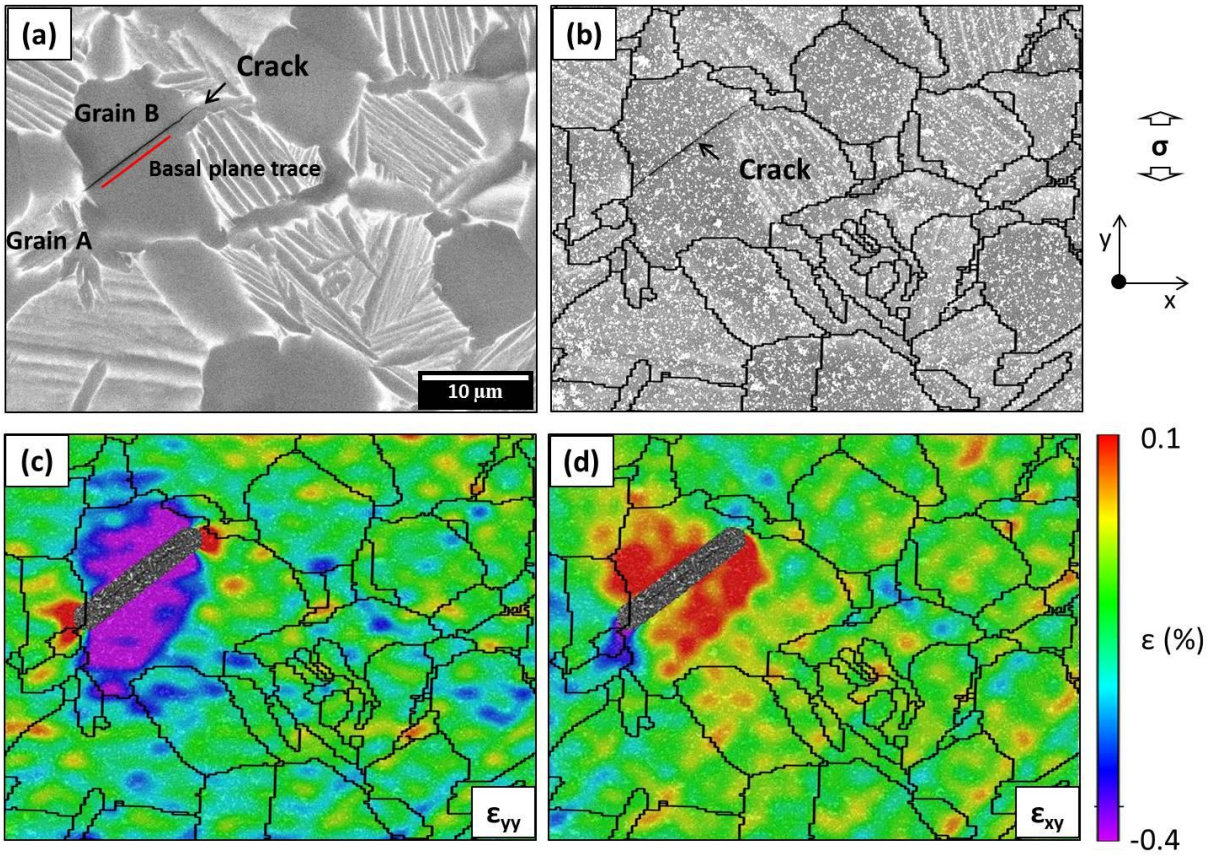

Figure 5.15: SEM-DIC strain maps at N = 2 x 10^6 cycles are shown for a Type #2 nascent fatigue crack that was initiated in vacuum at σ_a = 450 MPa. (a) A micrograph showing the specimen surface and crack after the speckle pattern was removed is shown. The crack initiated along a basal plane trace. (b) A BSE image of the patterned surface with the grain boundary locations overlaid in black and the crack highlighted within the speckle pattern is shown. The ε_{yy} strain map in (c) shows that Grain B, the hard grain, had less accumulated axial strain than its neighborhood. The shear strain map in (d) indicates that Grain B also had a higher degree of shear strain accumulated than Grain A, the soft grain, and the surrounding microstructure. This is in agreement with the hard – soft grain crack initiation mechanism proposed for Type #2 fatigue cracks.

5.4.3 Frequency of Occurrence of Type #1 Fatigue Crack Initiation Neighborhoods

The occurrence of Type #1 fatigue crack initiation neighborhoods within the material where investigated using a custom Matlab code. A large 500 x 500 μm^2 EBSD map was captured over a region with a pre-existing Type #1 fatigue crack located at the center of the map. Using the criteria discussed for Type #1 fatigue crack initiation neighborhoods, the code determined the number of neighborhoods that met these criteria within the EBSD map. Table 5.3 lists the criteria used in treatment of the EBSD data in the order of application. Figure 5.16 shows the resulting maps after treatment of the EBSD data for the indicated criteria. There were over 5600 grains in scanned area, including the two α_p grains where a fatigue crack initiated. Using the ranges determined from the experimental observations, grains were removed from the EBSD map if they did not meet the specified criterion, for example a basal Schmid factor between 0.25 and 0.50. After application of all of the specified criteria for Type #1 fatigue cracks, less than 1% of the initial grains remained, including the circled region where a Type #1 crack was known to have initiated. This indicates that neighborhoods suitable for fatigue crack initiation are rare.

Table 5.3: Criteria used in treatment of EBSD map to identify grains that may form Type #1 fatigue cracks

Step	Criterion
1	All grains: *0.25 < basal Schmid factor < 0.50*
2	All grains: *0.00 < prism Schmid factor < 0.10*
3	All nearest neighbor grains: *0.30 < basal Schmid factor < 0.50*
4	All nearest neighbor grains: *0.35 < prism Schmid factor < 0.50*
5	Misorientation angle between grains: $0° < \theta < 20°$

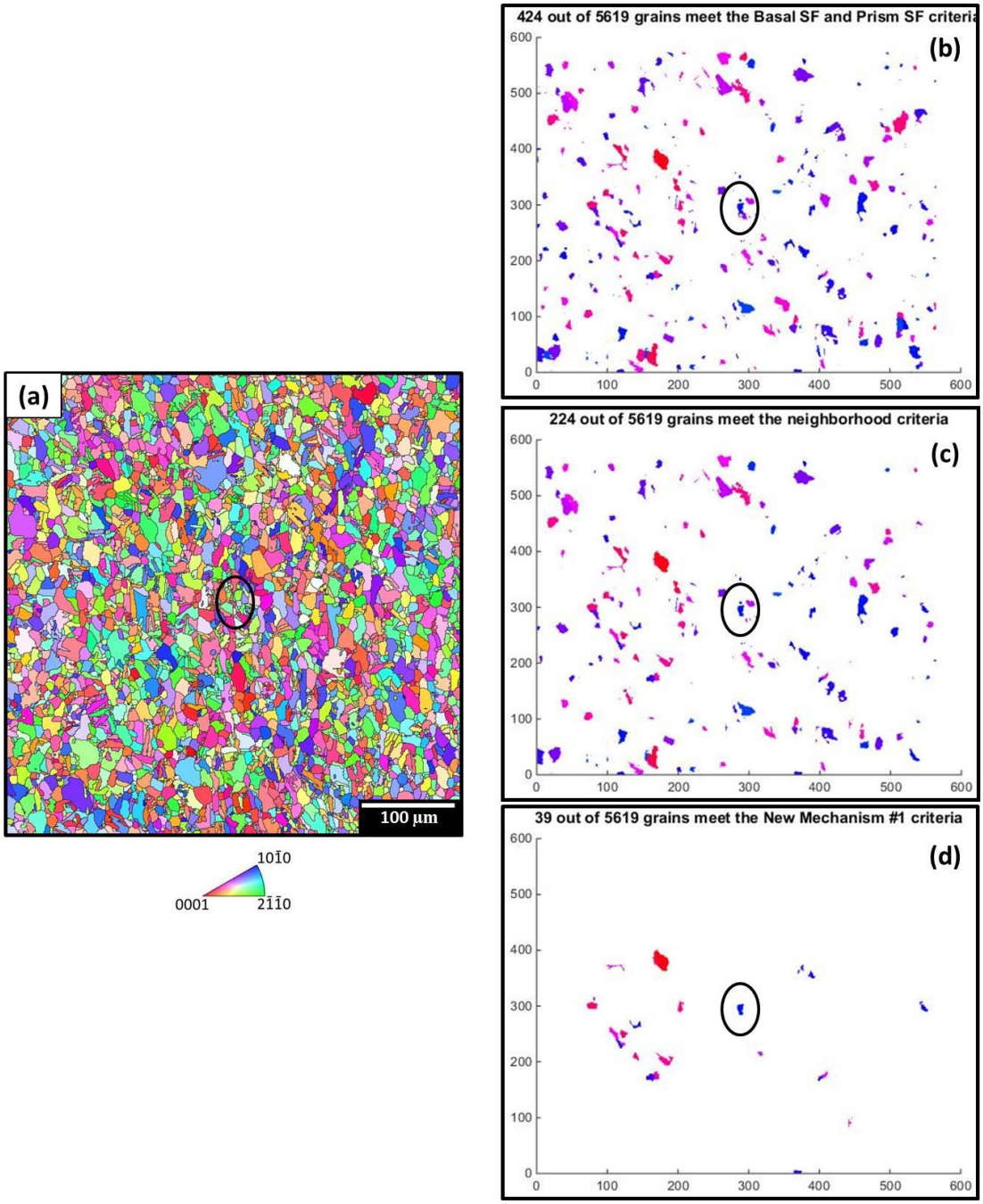

Figure 5.16: An example of some criteria for Type #1 fatigue crack initiation neighborhoods being applied to the (a) large EBSD map is shown. The circled grains produced a Type #1 fatigue crack during cycling in vacuum and should remain after treatment of the data. Plot (b) shows the grains that meet the basal and prismatic Schmid factor requirements. Plot (c) shows the grains that meet the Schmid factor requirement for the hard α_p grains and the soft neighborhood criterion. Plot (d) reduces these grains to only pairings that have a low misorientation grain boundary, in this case < 20°.

5.5 Summary and Conclusions

Results indicated that fatigue damage accumulation mechanisms and subsequent crack initiation are not significantly affected by environment. Ultrasonic fatigue in laboratory air and vacuum (1.7×10^{-4} Pa) at a stress ratio of R = -1 in the range of 400 – 550 MPa resulted in a shorter fatigue life in laboratory air compared to vacuum. Nascent, or non-fatal, cracks initiated as early as 10^6 cycles at σ_a = 450 MPa in vacuum, which was not significantly longer than the fatigue life of 8.8×10^5 cycles that was recorded for a specimen tested in laboratory air (step-tested). Additionally, fatigue specimens cycled in vacuum for 10^8 cycles and then cycled in laboratory air until failure produced similar fatigue lifetimes as samples cycled in air only. The majority of these samples failed at newly initiated cracks, despite the presence of numerous (at least 11 in one case) nascent cracks initiated in vacuum. None of the vacuum-initiated nascent cracks propagated during cycling in laboratory air, and no difference in the microstructural neighborhoods of the fatal cracks was observed. Also, nascent cracks in laboratory air were often longer than nascent cracks initiated in vacuum, despite the shorter lifetimes of laboratory air specimens. Yet, there was no microstructural difference in the types of fatigue cracks initiated in laboratory air and vacuum. Finally, fractography showed a similar appearance of crack nucleation facets, but differing features in the early crack growth regions of laboratory air and vacuum fracture surfaces. Smoother, more faceted regions were seen in air tests, while finer, ductile fracture regions were observed in vacuum.

Although fatigue damage accumulation mechanisms and subsequent crack initiation are not significantly affected by environment, early crack growth is strongly influenced by environmental effects. Specifically, damage accumulation and crack initiation mechanisms are mainly controlled by the microstructure. Given adequate time, i.e. an increased number of cycles,

more cracks will initiate based on the local microstructure, supported by the observation that more nascent cracks were formed in vacuum compared to air. There is likely a microstructural hierarchy that determines when a crack will initiate, but this may involve subsurface characteristics and no hierarchy was detected in this work, which relied only on surface characterization of microstructure neighborhoods. Once crack initiation occurs, environment plays a critical role in determining whether the crack will propagate. This finding is in agreement with the findings of the previous chapter, namely that small crack growth rates from FIB mico-notches were 2-3 orders of magnitude lower in vacuum than in laboratory air. The fact that cracks that initiated in vacuum did not propagate in subsequent cycling in air also suggests that crack-tip blunting may be an important mechanism in vacuum, which may also explain lower small fatigue crack growth rates in vacuum.

Two types of fatigues cracks were initiated in laboratory air and vacuum, with Type #1 being the most prevalent. The two types are defined as followed:

1. Type #1: Cracks initiated along (at/near) a low misorientation grain boundary between two similarly oriented α_p grains. The two α_p grains can be classified as hard compared to neighboring region, which can be described as soft. The grain boundary between these grains typically has a low misorientation (< 30°).
2. Type #2: Cracks initiated from high misorientation grain boundary between two grains. One grain can be classified as hard and the other grain as soft. The hard grain where the crack is initiated is a primary alpha grain and the soft grain can be either an α or $\alpha + \beta$ grain. OIM analysis shows that Type #2 cracks initiated on or near the basal plane of the α_p grain.

The mechanism responsible for the initiation of Type #1 fatigue cracks is proposed to be an increase of stress in the two similarly oriented hard α_p grains by load shedding of the soft surrounding microstructure. This additional stress combined with the nominal applied stress caused a crack to open up at the low misorientation angle grain boundary. The mechanism for Type #2 fatigue crack initiation is likely the result of strain incompatibility at the high misorientation grain boundary between the hard and soft grains. In agreement with the Stroh model, the strain localizes in the form of a slip band in the soft grain that is blocked by the grain boundary causing a dislocation pileup to form at the grain boundary. The dislocation pileup induces a normal and shear stress on the basal plane of the adjacent hard grain. The local shear stress causes slip on the basal plane of the hard grain and the local normal stress combines with the nominal applied stress to cause a crack to initiate on or near the basal plane.

CHAPTER 6

CONCLUSIONS AND FUTURE WORK

6.1 Conclusions

The conclusions from the investigation of microstructure and environmental effects on fatigue crack initiation and early crack growth in Ti-6242S during ultrasonic fatigue are the following:

1. Small fatigue crack growth rates determined by in-SEM testing using the UF-SEM system showed a significant increase in small fatigue crack growth rates in laboratory air versus vacuum (2 – 3 orders of magnitude) at an ultrasonic frequency of 20 kHz.
2. Small fatigue crack growth rates increased with increasing partial pressures of water vapor, oxygen, and hydrogen. Water vapor is more detrimental to small fatigue crack growth rates than oxygen and hydrogen. Fatigue crack growth rates in all gaseous environments were higher than those obtained in vacuum.
3. Based on surface observations, fatigue damage accumulation mechanisms and subsequent crack initiation lifetimes do not depend on whether initiation occurred in vacuum or laboratory air. This suggests that environment-specific differences in fatigue lifetime result from differences in short crack growth rates and not from differences in initiation lifetimes. Damage accumulation mechanisms leading to surface crack initiation are determined mainly by the microstructure, and not by the environment.

4. Two main types of microstructure neighborhood dependent fatigue crack initiation processes were observed. The most prevalent type was an initiated crack that nucleated near a low misorientation grain boundary between two similarly oriented hard α_p grains that were surrounded by a neighborhood of soft grains. The second type involved intragranular crack initiation within a hard α_p grain that was unfavorably oriented for prismatic slip and located adjacent to a soft grain. These cracks nucleated from the high misorientation grain boundary between the hard and soft grain and proceeded to propagate across the grain.

6.2 Recommendations for Future Work

Based on the findings discussed in this dissertation, the following recommendations are made for future work in this area.

1. Small fatigue crack growth studies in nitrogen, dry air, and at differing vacuum levels would help determine if there is a significant effect of nitrogen on FCGR in ultrasonic fatigue. Combined with AES and XPS measurements, this investigation may allow for quantification of the method and of the kinetics of the nitrogen interaction with the crack-tip plastic zone. This experimental methodology could also be modified to include varied isotopes of oxygen in order to detect the level of oxygen transported into the material, in an effort to further understand its effect on increasing the FCGR.
2. TEM dislocation analysis should be conducted on foils extracted from near the crack-tips of cracks of varying length that were grown in different environments. This analysis would provide more information regarding crack-tip plasticity and elemental composition at the crack-tip as a function of environment. Additionally, TEM studies on the dislocation structures developed in the neighborhoods of naturally initiated cracks in

laboratory air and vacuum would provide further insight on strain accumulation and dislocation pile-up processes.

3. Experimental evidence of slip processes leading to fatigue crack initiation and slip-preceding facet formation is lacking, yet the Stroh model is used extensively by the CPFE community and others as the predominant means of modeling both cyclic and dwell fatigue behavior. The main support for concepts explaining damage accumulation mechanisms remains post-mortem observations by SEM and TEM. While such observations are vital, direct experimental observations of damage accumulation processes would help to inform and validate these models. In this thesis, scanning electron microscopy (SEM-DIC) strain mapping techniques provided valuable insight regarding fatigue crack initiation mechanisms in the VHCF regime. The results presented in this work were obtained in an interrupted manner, but with automation and improved vibration damping of the UF-SEM system, *in situ* studies are possible. Based on the SEM-DIC studies discussed in this dissertation, the following improvements to the testing procedure are suggested:
    a. Increased inspection frequency will provide direct evidence of damage accumulation processes that lead to crack initiation and facet formation.
    b. Using reduced gage length specimens will enable easier monitoring of fatigue crack initiation sites due to the reduced surface area of interest. This would result in a significant time-savings per experiment.
    c. OIM analysis could be used in conjunction with custom Matlab scripts to identify fatigue critical microstructures before the start of testing. This would enable increased inspection frequency and higher magnification fields of view at key

areas of interest, thereby maximizing the effectiveness of the SEM-DIC technique at probing strain accumulation processes in VHCF.

4. The UF-SEM system is an effective and highly adaptable experimental tool for developing a better understanding of fatigue behavior in the VHCF regime. This is evident in its capabilities to perform both fatigue crack initiation and growth experiments in various environments with the possibility to incorporate *in situ* EBSD and SEM-DIC techniques. The following modifications/upgrades to the system are recommended going forward:
    a. Mean-stress capabilities to interrogate the effect of different load ratios on fatigue behavior, including environmental effects. This would permit *in situ* measurements of crack opening displacements at different loads in relation to proximity to different microstructural features. Also, information regarding the crack-tip plastic zone could be obtained with the use of SEM-DIC strain mapping techniques.
    b. Various automation improvements could be made to the system that would result in significant user time savings and increased knowledge gained for each experiment.
    c. Elevated temperature capabilities would enable investigation of fatigue behavior as a function of temperature. It is important to study structural engineering materials at the temperatures to which they would be subjected to in normal operation. Additionally, a permanent means of monitoring the temperature of the fatigue specimen, *in situ*, would also be useful

APPENDICES

Appendix A
Ultrasonic Fatigue Specimen Drawing

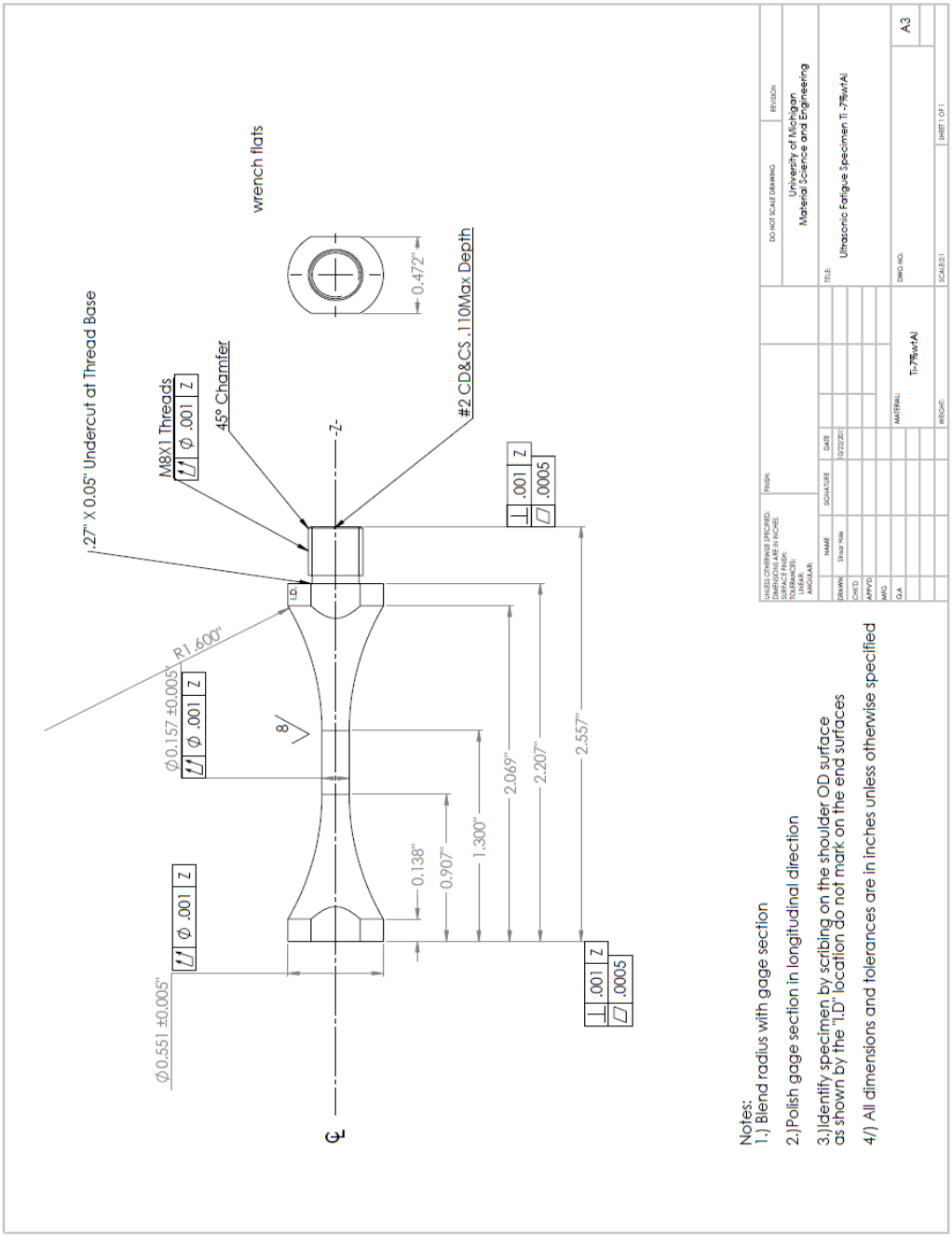

Appendix B
Ultrasonic Fatigue Testing Principle

Ultrasonic fatigue testing has been used since the early 1950s [13, 14] to provide a powerful and time-effective means for interrogating the very high cycle fatigue regime. Higher testing frequencies are possible, but most investigations of structural materials utilize a nominal operating frequency of 20 kHz because the resonance frequency is inversely proportional to the specimen length. The principles of the ultrasonic fatigue testing technique are summarized as follows.

The velocity of a wave propagating in a smooth cylindrical bar of constant diameter is given by Equation A.1, E is the Young's modulus, and ρ is the density.

$$k = \sqrt{\frac{E}{\rho}} \tag{A.1}$$

The equation for the first mode of vibration is given by Equation A.2. The displacement, u, is a function of position, x, and time, t.

$$u(x,t) = A_o \cos(kx) \sin(\omega t) \tag{A.2}$$

The amplitude at any point x along the bar is given by Equation A.3,

$$A(x) = A_o \cos(kx) \tag{A.3}$$

where A_o is the amplitude at the end of the bar and,

$$k = \sqrt{\frac{\pi}{l}}, \omega = \frac{\pi c}{l} \tag{A.4}$$

The strain, ε, at each point along the bar is given by Equation A.5.

$$\varepsilon(x,t) = -kA_o \sin(kx) \sin(\omega t) \tag{A.5}$$

Combining Equations A.1 and A.4,

$$l = \frac{1}{2f}\sqrt{\frac{E_d}{\rho}} \tag{A.6}$$

where $f = \omega/2\pi$, l is the wavelength of the acoustic pulse, and E_d is the dynamic elastic modulus. Equation A.6 establishes the resonance length to ensure that the amplitude of the acoustic wave is not attenuated. The load train components and the fatigue specimen used in the ultrasonic fatigue system are designed with this principle in mind.

REFERENCES

1. HCF, H.C.F., *AFRL-PR-WP-TR-2002-2060.* 2002.
2. Suresh, S., *Fatigue of materials. 2nd ed.* 1998: Cambridge University Pres.
3. Sakai, T., *Review and prospects for current studies on very high cycle fatigue of metallic materials for machine structural use.* Journal of Solid Mechanics and Materials Engineering, 2009. **3**(3): p. 425-439.
4. Miller, K.J. and W.J. O'Donnel, *The fatigue limit and its elimination.* Fatige Fract. Engng Mater. Struct., 1999. **22**: p. 545-557.
5. Sakai, T., Y. Sato, and N. Oguma, *Characteristic S–N properties of high-carbon–chromium-bearing steel under axial loading in long-life fatigue.* Fatigue & Fracture of Engineering Materials & Structures, 2002. **25**: p. 765-773.
6. Bathias, C., *There is no infinite fatigue life in metallic materials.* Fatigue & Fracture of Engineering Materials & Structures, 1999. **22**: p. 559–565.
7. Wang, Q.Y., et al., *Gigacycle fatigue of ferrous alloys.* Fatigue & Fracture of Engineering Materials & Structures, 1999. **22**: p. 667-672.
8. Miao, J., T.M. Pollock, and J.W. Jones, *Very High Cycle Fatigue Crack Initiation in Nickel-based Superalloy René 88 DT at 593 ° C*, 2010, Materials Science.
9. Mughrabi, H., *On the life-controlling microstructural fatigue mechanisms in ductile metals and alloys in the gigacycle regime*, in *Materials and Structures*. 1999. p. 633-641.
10. Stanzl-Tschegg, S.E. and B. Schönbauer, *Mechanisms of strain localization, crack initiation and fracture of polycrystalline copper in the VHCF regime.* International Journal of Fatigue, 2010. **32**(6): p. 886-893.
11. Szczepanski, C.J., et al., *Microstructural Influences on Very-High-Cycle Fatigue-Crack Initiation in Ti-6246.* Metallurgical and Materials Transactions A, 2008. **39**(12): p. 2841-2851.
12. Mughrabi, H., *On the life-controlling microstructural fatigue mechanisms in ductile metals and alloys in the gigacycle regime.* Fatigue and fracture of engineering materials and structures, 1999. **22**(7): p. 633.
13. Willertz, L.E., *Ultrasonic Fatigue.* International Materials Reviews, 1980. **25**(1): p. 65-78.
14. Mason, W.P., *Piezoelectric crystals and their application to ultrasonics*. 1950: van Nostrand.
15. Caton, M.J., et al., *Demonstration of an endurance limit in cast 319 aluminum.* Metallurgical and Materials Transactions A, 2003. **34**(1): p. 33-41.
16. Zhu, X., J.W. Jones, and J.E. Allison, *Effect of Frequency, Environment, and Temperature on Fatigue Behavior of E319 Cast Aluminum Alloy: Stress-Controlled Fatigue Life Response.* Metallurgical and Materials Transactions A, 2008. **39**(11): p. 2681-2688.

17. Liu, L., et al., *In Situ Imaging of High Cycle Fatigue Crack Growth in Single Crystal Nickel-Base Superalloys by Synchrotron X-Radiation.* Journal of Engineering materials and Technology, 2008. **130**(2).
18. Furuya, Y., *Specimen size effects on gigacycle fatigue properties of high-strength steel under ultrasonic fatigue testing.* Scripta Materialia, 2008. **58**(11): p. 1014-1017.
19. Stanzl-Tschegg, S. and B. Schönbauer, *Near-threshold fatigue crack propagation and internal cracks in steel.* Procedia Engineering, 2010. **2**(1): p. 1547-1555.
20. Stanzl, S. and E. Tschegg, *Influence of environment on fatigue crack growth in the threshold region.* Acta Metallurgica, 1981. **29**(1): p. 21-32.
21. Mayer, H., *Fatigue crack growth and threshold measurements at very high frequencies.* International Materials Reviews, 1999. **44**(1): p. 1-34.
22. Caton, M.J., J.W. Jones, and J.E. Allison, *The influence of heat treatment and solidification time on the behavior of small-fatigue-cracks in a cast aluminum alloy.* Materials Science and Engineering: A, 2001. **314**(1-2): p. 81-85.
23. Mitsche, R., S. Stanzl, and D. Burkert, *Hochfrequenzkinematographie in der Metallforschung.* Wissenschaftlicher Film, 1973. **14**(3): p. 10.
24. Stanzl-Tschegg, S., H. Mughrabi, and B. Schoenbauer, *Life time and cyclic slip of copper in the VHCF regime.* International Journal of Fatigue, 2007. **29**(9–11): p. 2050-2059.
25. Lütjering, G. and J.C. Williams, *Titanium*. Vol. 2. 2003: Springer.
26. Leyens, C. and M. Peters, *Titanium and titanium alloys*. 2003: Wiley Online Library.
27. Banerjee, D. and J. Williams, *Perspectives on titanium science and technology.* Acta materialia, 2013. **61**(3): p. 844-879.
28. Schuster, J.C. and M. Palm, *Reassessment of the binary aluminum-titanium phase diagram.* Journal of phase equilibria and diffusion, 2006. **27**(3): p. 255-277.
29. Collings, E., *The physical metallurgy of titanium alloys.* American Society for Metals, 1984, 1984: p. 261.
30. Banerjee, D., A.L. Pilchak, and J.C. Williams. *Processing, Structure, Texture and Microtexture in Titanium Alloys*. in *Materials Science Forum*. 2012. Trans Tech Publ.
31. Ogi, H., et al., *Titanium's high-temperature elastic constants through the hcp–bcc phase transformation.* Acta materialia, 2004. **52**(7): p. 2075-2080.
32. Larson, F. and A. Zarkades, *Properties of textured titanium alloys*, 1974, DTIC Document.
33. Savage, M., J. Tatalovich, and M. Mills, *Anisotropy in the room-temperature deformation of α–β colonies in titanium alloys: role of the α–β interface.* Philosophical Magazine, 2004. **84**(11): p. 1127-1154.
34. Bache, M., et al., *Characterization of mechanical anisotropy in titanium alloys.* Materials Science and Engineering: A, 1998. **257**(1): p. 139-144.
35. Donachie, M.J., *Titanium and Titanium alloys: source book: a collection of outstanding articles from the technical literature*. 1982: ASM international.
36. Paton, N., R. Baggerly, and J. Williams, *Deformation and Solid Solution Strengthening of Titanium-Aluminum Single Crystals*, 1976, DTIC Document.
37. Paton, N., J. Williams, and G. Rauscher, *The deformation of alpha-phase titanium.* Titanium science and technology, 1973: p. 1049-1069.
38. Tanaka, T. and H. Conrad, *Deformation kinetics for {10$\bar{1}$0}< 11$\bar{2}$0> slip in titanium single crystals below 0.4T m.* Acta Metallurgica, 1972. **20**(8): p. 1019-1029.

39. Williams, J., R. Baggerly, and N. Paton, *Deformation behavior of HCP Ti-Al alloy single crystals.* Metallurgical and Materials Transactions A, 2002. **33**(13): p. 837-850.
40. Williams, J., A. Sommer, and P. Tung, *The influence of oxygen concentration on the internal stress and dislocation arrangements in α titanium.* Metallurgical Transactions, 1972. **3**(11): p. 2979-2984.
41. Churchman, A. *The slip modes of titanium and the effect of purity on their occurrence during tensile deformation of single crystals*. in *Proceedings of the Royal Society of London A: Mathematical, Physical and Engineering Sciences*. 1954. The Royal Society.
42. Hall, J., *Fatigue crack initiation in alpha-beta titanium alloys.* International Journal of Fatigue, 1997. **19**(93): p. 23-37.
43. Bridier, F., P. Villechaise, and J. Mendez, *Slip and fatigue crack formation processes in an α/β titanium alloy in relation to crystallographic texture on different scales.* Acta materialia, 2008. **56**(15): p. 3951-3962.
44. Bantounas, I., D. Dye, and T.C. Lindley, *The effect of grain orientation on fracture morphology during high-cycle fatigue of Ti–6Al–4V.* Acta materialia, 2009. **57**(12): p. 3584-3595.
45. Wells, C. and C. Sullivan, *LOW-CYCLE FATIGUE CRACK INITIATION IN Ti--6Al--4V*, 1969, Pratt and Whitney Aircraft, Middletown, Conn.
46. Bache, M., et al., *The effects of texture in titanium alloys for engineering components under fatigue.* International Journal of Fatigue, 2001. **23**: p. 153-159.
47. Baxter, G., W. Rainforth, and L. Grabowski, *TEM observations of fatigue damage accumulation at the surface of the near-α titanium alloy IMI 834.* Acta materialia, 1996. **44**(9): p. 3453-3463.
48. Le Biavant, K., S. Pommier, and C. Prioul, *Local texture and fatigue crack initiation in a Ti-6Al-4V titanium alloy.* Fatigue & Fracture of Engineering Materials & Structures, 2002. **25**(6): p. 527-545.
49. Neeraj, T., et al., *Phenomenological and microstructural analysis of room temperature creep in titanium alloys.* Acta materialia, 2000. **48**(6): p. 1225-1238.
50. Sinha, V., M. Mills, and J. Williams, *Crystallography of fracture facets in a near-alpha titanium alloy.* Metallurgical and Materials Transactions A, 2006. **37**(6): p. 2015-2026.
51. Evans, W. and M. Bache, *Dwell-sensitive fatigue under biaxial loads in the near-alpha titanium alloy IMI685.* International Journal of Fatigue, 1994. **16**(7): p. 443-452.
52. Bantounas, I., D. Dye, and T.C. Lindley, *The role of microtexture on the faceted fracture morphology in Ti–6Al–4V subjected to high-cycle fatigue.* Acta materialia, 2010. **58**(11): p. 3908-3918.
53. Slavik, D., J. Wert, and R. Gangloff, *Determining fracture facet crystallography using electron backscatter patterns and quantitative tilt fractography.* Journal of materials research, 1993. **8**(10): p. 2482-2491.
54. Neal, D. and P. Blenkinsop, *Internal fatigue origins in α-β titanium allols.* Acta Metallurgica, 1976. **24**(1): p. 59-63.
55. Stroh, A.N., *A theory of the fracture of metals.* Advances in Physics, 1957. **6**(24): p. 418-465.
56. Brandes, M., M. Mills, and J. Williams, *The Influence of Slip Character on the Creep and Fatigue Fracture of an α Ti-Al Alloy.* Metallurgical and Materials Transactions A, 2010. **41**(13): p. 3463-3472.

57. Stroh, A. *The formation of cracks as a result of plastic flow*. in *Proceedings of the Royal Society of London A: Mathematical, Physical and Engineering Sciences*. 1954. The Royal Society.
58. Pearson, S., *Initiation of fatigue cracks in commercial aluminium alloys and the subsequent propagation of very short cracks.* Engineering Fracture Mechanics, 1975. **7**(2): p. 235-247.
59. Caton, M., et al., *The effect of solidification rate on the growth of small fatigue cracks in a cast 319-type aluminum alloy.* Metallurgical and Materials Transactions A, 1999. **30**(12): p. 3055-3068.
60. Lankford, J., *The growth of small fatigue cracks in 7075–T6 aluminum.* Fatigue & Fracture of Engineering Materials & Structures, 1982. **5**(3): p. 233-248.
61. Tanaka, K., Y. Nakai, and M. Yamashita, *Fatigue growth threshold of small cracks.* International Journal of fracture, 1981. **17**(5): p. 519-533.
62. Ritchie, R. and J. Lankford, *Small fatigue cracks: a statement of the problem and potential solutions.* Materials Science and Engineering, 1986. **84**: p. 11-16.
63. Davidson, D. and J. Lankford, *Fatigue crack growth in metals and alloys: mechanisms and micromechanics.* International Materials Reviews, 2013.
64. Suresh, S. and R. Ritchie, *Propagation of short fatigue cracks.* International Metals Reviews, 2013.
65. Schroeder, G., J. Albrecht, and G. Luetjering, *Fatigue crack propagation in titanium alloys with lamellar and bi-lamellar microstructures.* Materials Science and Engineering: A, 2001. **319**: p. 602-606.
66. Sinha, V. and W. Soboyejo, *An investigation of the effects of colony microstructure on fatigue crack growth in Ti–6Al–4V.* Materials Science and Engineering: A, 2001. **319**: p. 607-612.
67. Dubey, S., A. Soboyejo, and W. Soboyejo, *An investigation of the effects of stress ratio and crack closure on the micromechanisms of fatigue crack growth in Ti-6Al-4V.* Acta materialia, 1997. **45**(7): p. 2777-2787.
68. Benedetti, M., et al., *Influence of sharp microstructural gradients on the fatigue crack growth resistance of α+ β and near-α titanium alloys.* Fatigue & Fracture of Engineering Materials & Structures, 2005. **28**(10): p. 909-922.
69. Ravichandran, K., *Near threshold fatigue crack growth behavior of a titanium alloy: Ti-6A1-4V.* Acta metallurgica et materialia, 1991. **39**(3): p. 401-410.
70. Ritchie, R., et al., *Thresholds for high-cycle fatigue in a turbine engine Ti–6Al–4V alloy.* International Journal of Fatigue, 1999. **21**(7): p. 653-662.
71. Zhai, T., A. Wilkinson, and J. Martin, *A crystallographic mechanism for fatigue crack propagation through grain boundaries.* Acta materialia, 2000. **48**(20): p. 4917-4927.
72. Marx, M., W. Schaef, and H. Vehoff, *Interaction of short cracks with the local microstructure.* Procedia Engineering, 2010. **2**(1): p. 163-171.
73. Saleh, Y. and H. Margolin, *Low cycle fatigue of Ti-Mn alloys: Microstructural aspects of fatigue crack growth.* Metallurgical Transactions A, 1983. **14**(7): p. 1481-1486.
74. Szczepanski, C., et al., *The Role of Local Microstructure on Small Fatigue Crack Propagation in an α+ β Titanium Alloy, Ti-6Al-2Sn-4Zr-6Mo.* Metallurgical and Materials Transactions A, 2012. **43**(11): p. 4097-4112.

75. Jin, O. and S. Mall, *Effects of microstructure on short crack growth behavior of Ti–6Al–2Sn–4Zr–2Mo–0.1 Si alloy.* Materials Science and Engineering: A, 2003. **359**(1): p. 356-367.
76. Sinha, V., C. Mercer, and W. Soboyejo, *An investigation of short and long fatigue crack growth behavior of Ti–6Al–4V.* Materials Science and Engineering: A, 2000. **287**(1): p. 30-42.
77. Bowen, A.W., *The influence of crystallographic orientation on fatigue crack growth in strongly textured Ti ‐ 6A1 ‐ 4V.* Acta Metallurgica, 1975. **23**(11): p. 1401-1409.
78. Krupp, U., et al., *Mechanisms of short-fatigue-crack initiation and propagation in a β-Ti alloy.* Philosophical Magazine A, 2002. **82**(17-18): p. 3321-3332.
79. Sakai, T., Y. Sato, and N. Oguma, *Characteristic S–N properties of high‐carbon–chromium‐bearing steel under axial loading in long‐life fatigue.* Fatigue & Fracture of Engineering Materials & Structures, 2002. **25**(8-9): p. 765-773.
80. Mughrabi, H., *Specific features and mechanisms of fatigue in the ultrahigh-cycle regime.* International Journal of Fatigue, 2006. **28**(11): p. 1501-1508.
81. Lukáš, P. and L. Kunz, *Specific features of high‐cycle and ultra‐high‐cycle fatigue.* Fatigue & Fracture of Engineering Materials & Structures, 2002. **25**(8-9): p. 747-753.
82. Li, W., et al., *Subsurface inclusion-induced crack nucleation and growth behaviors of high strength steels under very High cycle fatigue: Characterization and microstructure-based modeling.* Materials Science and Engineering: A, 2015. **641**: p. 10-20.
83. Szczepanski, C.J., *The Role of Microstructural Variability on the Very High Cycle Fatigue Lifetime Variability of the Alpha+ Beta Titanium Alloy, Ti-6246*. 2008: ProQuest.
84. Liu, X., C. Sun, and Y. Hong, *Faceted crack initiation characteristics for high-cycle and very-high-cycle fatigue of a titanium alloy under different stress ratios.* International Journal of Fatigue, 2016.
85. Gilbert, J.L. and H.R. Piehler, *On the nature and crystallographic orientation of subsurface cracks in high cycle fatigue of Ti-6Al-4V.* Metallurgical Transactions A, 1993. **24**(3): p. 669-680.
86. Sinha, V. and J. Larsen, *Vacuum Levels Needed to Simulate Internal Fatigue Crack Growth in Titanium Alloys and Nickel-Base Superalloys: Thermodynamic Considerations.* Metallurgical and Materials Transactions A, 2012. **43**(10): p. 3433-3441.
87. Davidson, D.L., *Damage mechanisms in high cycle fatigue*, 1999, DTIC Document.
88. Stanzl-Tschegg, S., *Fatigue crack growth and thresholds at ultrasonic frequencies.* International Journal of Fatigue, 2006. **28**(11): p. 1456-1464.
89. Roth, L., L. Willertz, and T. Leax, *On the fatigue of copper up to ultrasonic frequencies.* Ultrasonic Fatigue, 1981: p. 265-282.
90. Morrissey, R., D. McDowell, and T. Nicholas, *Frequency and stress ratio effects in high cycle fatigue of Ti-6Al-4V.* International Journal of Fatigue, 1999. **21**(7): p. 679-685.
91. Smith, S.W. and R.S. Piascik, *The Effect of O2, H2O, and N2 on the Fatigue Crack Growth Behavior of an A+ B Titanium Alloy at 24°C and 177°C*. 2001: Citeseer.
92. Sarrazin-Baudoux, C., S. Lesterlin, and J. Petit, *Atmospheric influence on fatigue crack propagation in titanium alloys at elevated temperature.* ASTM special technical publication, 1997. **1297**: p. 117-139.

93. Demulsant, X. and J. Mendez, *Influence of environment on low cycle fatigue damage in Ti 6Al 4V and Ti 6246 titanium alloys.* Materials Science and Engineering: A, 1996. **219**(1): p. 202-211.
94. Shimojo, M., et al., *The entering behavior of environmental gases into the plastic zone around fatigue crack tips in titanium.* Metallurgical and Materials Transactions A, 1997. **28**(6): p. 1341-1346.
95. Sarrazin-Baudoux, C., F. Loubat, and S. Potiron, *On the role of water vapor and oxygen on the fatigue crack propagation behavior at 550° C of a Ti6242 alloy.* Metallurgical and Materials Transactions A, 2006. **37**(4): p. 1201-1209.
96. Ding, Y., L. Tsay, and C. Chen, *The effects of hydrogen on fatigue crack growth behaviour of Ti–6Al–4V and Ti–4.5 Al–3V–2Mo–2Fe alloys.* Corrosion Science, 2009. **51**(6): p. 1413-1419.
97. Bache, M., W. Evans, and M. McElhone, *The effects of environment and internal oxygen on fatigue crack propagation in Ti-6Al-4V.* Materials Science and Engineering: A, 1997. **234**: p. 918-922.
98. Gao, S., G. Simmons, and R. Wei, *Fatigue crack growth surface reactions for titanium alloys exposed to water vapor.* Materials Science and Engineering, 1984. **62**(1): p. 65-78.
99. Gaddam, R., et al., *Fatigue crack growth behaviour of forged Ti–6Al–4V in gaseous hydrogen.* Corrosion Science, 2014. **78**: p. 378-383.
100. Pittinato, G., *REACTIVITY OF HYDROGEN WITH Ti--6Al--4V UNDER FATIGUE CYCLING AT AMBIENT AND CRYOGENIC TEMPERATURES*, 1969, McDonnell Douglas Corp., Santa Monica, Calif.
101. Pittinato, G., *Hydrogen-enhanced fatigue crack growth in Ti-6Al-4V ELI weldments.* Metallurgical Transactions, 1972. **3**(1): p. 235-243.
102. Williams, D.P. and H.G. Nelson, *Gaseous hydrogen-induced cracking of Ti-5Al-2.5 Sn.* Metallurgical Transactions, 1972. **3**(8): p. 2107-2113.
103. Nelson, H.G., D.P. Williams, and J.E. Stein, *Environmental hydrogen embrittlement of an α-β titanium alloy: effect of microstructure.* Metallurgical Transactions, 1972. **3**(2): p. 473-479.
104. Christ, H.-J., M. Decker, and S. Zeitler, *Hydrogen diffusion coefficients in the titanium alloys IMI 834, Ti 10-2-3, Ti 21 S, and alloy C.* Metallurgical and Materials Transactions A, 2000. **31**(6): p. 1507-1517.
105. Moody, N. and W. Gerberich, *Hydrogen-induced slow crack growth in Ti-6Al-6V-2Sn.* Metallurgical Transactions A, 1980. **11**(6): p. 973-981.
106. Shih, D., I. Robertson, and H. Birnbaum, *Hydrogen embrittlement of α titanium: in situ TEM studies.* Acta Metallurgica, 1988. **36**(1): p. 111-124.
107. Evans, W. and M. Bache, *Hydrogen and fatigue behaviour in a near alpha titanium alloy.* Scripta metallurgica et materialia, 1995. **32**(7): p. 1019-1024.
108. Shimojo, M., Y. Higo, and Y. Oya-Seimiya, *Effects of inert gases on fatigue crack growth and their transportation into subsurface regions in titanium.* Metallurgical and Materials Transactions A, 2000. **31**(5): p. 1435-1441.
109. Maier, H., R. Teteruk, and H.-J. Christ, *Modeling thermomechanical fatigue life of high-temperature titanium alloy IMI 834.* Metallurgical and Materials Transactions A, 2000. **31**(2): p. 431-444.

110. Pilchak, A. and J. Williams, *Observations of facet formation in near-α titanium and comments on the role of hydrogen.* Metallurgical and Materials Transactions A, 2011. **42**(4): p. 1000-1027.
111. Sarrazin-Baudoux, C., S. Lesterlin, and J. Petit, *Atmospheric influence on fatigue crack propagation in titanium alloys at elevated temperature*, in *Elevated temperature effects on fatigue and fracture*. 1997, ASTM International.
112. Stanzl, S.E., H.R. Mayer, and E.K. Tschegg, *The influence of air humidity on near-threshold fatigue crack growth of 2024-T3 aluminum alloy.* Materials Science and Engineering: A, 1991. **147**(1): p. 45-54.
113. Zhu, X., J. Jones, and J. Allison, *Effect of frequency, environment, and temperature on fatigue behavior of E319 cast-aluminum alloy: small-crack propagation.* Metallurgical and Materials Transactions A, 2008. **39**(11): p. 2666-2680.
114. Zhu, X., J. Jones, and J. Allison, *Effect of frequency, environment, and temperature on fatigue behavior of E319 cast aluminum alloy: stress-controlled fatigue life response.* Metallurgical and Materials Transactions A, 2008. **39**(11): p. 2681-2688.
115. Lu, G., S.L. Bernasek, and J. Schwartz, *Oxidation of a polycrystalline titanium surface by oxygen and water.* Surface Science, 2000. **458**(1): p. 80-90.
116. Vaquila, I., M. Passeggi, and J. Ferrón, *Oxide stoichiometry in the early stages of titanium oxidation.* Surface Science, 1993. **292**(1): p. L795-L800.
117. Vaquila, I., et al., *Chemical reactions at surfaces: titanium oxidation.* Surface and Coatings Technology, 1999. **122**(1): p. 67-71.
118. Kasemo, B., *Biocompatibility of titanium implants: surface science aspects.* The Journal of prosthetic dentistry, 1983. **49**(6): p. 832-837.
119. Coddet, C., A. Craze, and G. Beranger, *Measurements of the adhesion of thermal oxide films: application to the oxidation of titanium.* Journal of materials science, 1987. **22**(8): p. 2969-2974.
120. Hierro-Oliva, M., A. Gallardo-Moreno, and M. González-Martín, *XPS Analysis of Ti6Al4V Oxidation Under UHV Conditions.* Metallurgical and Materials Transactions A, 2014. **45**(13): p. 6285-6290.
121. Sittig, C., et al., *Surface characterization.* Journal of Materials Science: Materials in Medicine, 1999. **10**(1): p. 35-46.
122. Azoulay, A., et al., *Hydrogen interactions with polycrystalline and with deposited titanium surfaces.* Journal of alloys and compounds, 1997. **248**(1): p. 209-214.
123. Oshida, Y., *Bioscience and bioengineering of titanium materials*. 2010: Elsevier.
124. Azoulay, A., et al., *The initial interactions of oxygen with polycrystalline titanium surfaces.* Surface Science, 1997. **370**(1): p. 1-16.
125. Lee, P.A., et al., *Oxide formation on Fe and Ti thin films and on Fe thin films modified with ultrathin layers of Ti.* Surface and Interface Analysis, 1991. **17**(1): p. 48-56.
126. Galerie, A., Y. Wouters, and J.P. Petit. *Interfacial reactions and diffusion during the thermal oxidation of titanium in water vapour*. in *Materials science forum*. 1997. Trans Tech Publ.
127. Azoulay, A., et al., *Water vapor interactions with polycrystalline titanium surfaces.* Surface Science, 1999. **422**(1): p. 141-153.
128. Orloff, J., L.W. Swanson, and M.W. Utlaut, *High resolution focused ion beams: FIB and its applications: The physics of liquid metal ion sources and ion optics and their application to focused ion beam technology*. 2003: Springer.

129. Newman, J. and I. Raju, *An empirical stress-intensity factor equation for the surface crack.* Engineering Fracture Mechanics, 1981. **15**(1-2): p. 185-192.
130. Mølhave, K. and P. Bøggild, *Tools for in-situ manipulation and characterization of nanostructures.* Lyngby: Technical University of Denmark, 2004: p. 209.
131. Paris, P. and F. Erdogan, *A critical analysis of crack propagation laws.* Journal of basic engineering, 1963. **85**(4): p. 528-533.
132. Yu, Q., et al., *Origin of dramatic oxygen solute strengthening effect in titanium.* Science, 2015. **347**(6222): p. 635-639.
133. Oguma, H. and T. Nakamura, *Fatigue crack propagation properties of Ti–6Al–4V in vacuum environments.* International Journal of Fatigue, 2013. **50**: p. 89-93.
134. Sugano, M., S. Kanno, and T. Satake, *Fatigue behavior of titanium in vacuum.* Acta Metallurgica, 1989. **37**(7): p. 1811-1820.
135. Bache, M.R., W.J. Evans, and M. McElhone, *The effects of environment and internal oxygen on fatigue crack propagation in ti-6al-4v.* Materials Science and Engineering: A, 1997. **234–236**(0): p. 918-922.
136. Irving, P.E. and C.J. Beevers, *The effect of air and vacuum environments on fatigue crack growth rates in Ti-6Al-4V.* Metallurgical Transactions, 1974. **5**(2): p. 391-398.
137. McClung, R., et al., *Fatigue crack growth of titanium rotor alloys in vacuum and air.* Fatigue Behavior of Titanium Alloys, 1999: p. 211-218.
138. Guo, B., K. Kerns, and A. Castleman, *Chemistry and kinetics of primary reactions of TI+ with H2O, NH3, CH3, CH3OH, C2H4, and C3H6 at thermal energies.* Journal of physical chemistry, 1992. **96**(12): p. 4879-4883.
139. Swanson, J. and H. Marcus, *Oxygen transport during fatigue crack growth.* Metallurgical and Materials Transactions A, 1978. **9**(2): p. 291-293.
140. Stout, V.L. and M.D. Gibbons, *Gettering of gas by titanium.* Journal of applied physics, 1955. **26**(12): p. 1488-1492.
141. Uchida, H. and E. Fromm, *Kinetics of hydrogen absorption by titanium, tantalum, tungsten, iron and palladium films with and without oxygen preabsorption at 300 K.* Journal of the Less Common Metals, 1983. **95**(1): p. 139-146.
142. Wulv, H. and E. Fromm, *Hydrogen absorption rate of titanium, lanthanum, iron, nickel, manganese and palladium films with and without ovygen precoverage at 300 K.* Journal of the Less Common Metals, 1986. **118**(2): p. 293-301.
143. Ritchie, R. and S. Suresh, *Some considerations on fatigue crack closure at near-threshold stress intensities due to fracture surface morphology.* Metallurgical Transactions A, 1982. **13**(5): p. 937-940.
144. Elsworth, L., L. Holland, and L. Laurenson, *The sorption of N 2, H 2 and D 2 on titanium films at 20° C and− 190° C.* Vacuum, 1965. **15**(7): p. 337-345.
145. Gulbransen, E.A. and K.F. Andrew, *Kinetics of the Reactions of Zirconium with O2, N2 and H2.* Transactions of the American Institute of Mining, Metallurgical and Petroleum Engineers, 1949. **185**: p. 8.
146. Robertson, I. and H. Birnbaum. *Dislocation mobility and hydrogen–a brief review*. in *Proc. 11th International Conference on Fracture, http://www.icf11. com/proceeding/EXTENDED/5759. pdf, accessed*. 2009.
147. Tal-Gutelmacher, E., D. Eliezer, and D. Eylon, *The effects of low fugacity hydrogen in duplex-and beta-annealed Ti–6Al–4V alloy.* Materials Science and Engineering: A, 2004. **381**(1): p. 230-236.

148. Gao, M., R. Wei, and P. Pao, *Chemical and metallurgical aspects of environmentally assisted fatigue crack growth in 7075-T651 aluminum alloy.* Metallurgical Transactions A, 1988. **19**(7): p. 1739-1750.
149. Wei, R., *Environmental considerations for fatigue cracking.* Fatigue & Fracture of Engineering Materials & Structures, 2002. **25**(8-9): p. 845-854.
150. Mason, E.A. and A. Malinauskas, *Gas transport in porous media: the dusty-gas model*. Vol. 17. 1983: Elsevier Science Ltd.
151. Covington, L., *The influence of surface condition and environment on the hydriding of titanium.* Corrosion, 1979. **35**(8): p. 378-382.
152. Geathers, J., et al., *Investigating environmental effects on small fatigue crack growth in Ti–6242S using combined ultrasonic fatigue and scanning electron microscopy.* International Journal of Fatigue, 2015. **70**: p. 154-162.
153. Kammers, A.D. and S. Daly, *Digital image correlation under scanning electron microscopy: methodology and validation.* Experimental Mechanics, 2013. **53**(9): p. 1743-1761.
154. Kammers, A.D. and S. Daly, *Self-assembled nanoparticle surface patterning for improved digital image correlation in a scanning electron microscope.* Experimental Mechanics, 2013. **53**(8): p. 1333-1341.